The Hydrocracking of Long Chain n-Paraffins under Fischer-Tropsch Conditions

Jacqueline Binneman

Submitted in partial fulfillment of the requirements
of the degree of Master of Science in Chemical Engineering

June 2012

Centre for Catalysis Research
Department of Chemical Engineering
University of Cape Town
Cape Town
South Africa

Synopsis

Interest in the area of hydrocracking has grown rapidly over the years. In the early 1960's companies such as Chevron and Universal Oil Products (UOP) introduced new hydrocracking processes to manufacture high octane gasoline. The demand for transportation fuels such as diesel and jet fuel has increased significantly which results in the continuous development of hydrocracking techniques and catalysts. The conversion of normal long chain paraffins from the Fischer-Tropsch synthesis to clean distillate fuels is a particular area of interest. The objective of this project is to investigate the hydrocracking of long chain paraffins under F-T conditions.

The aim is to achieve in situ, the hydrocracking of low temperature Cobalt-based F-T wax by combining F-T synthesis and hydrocracking in a single reactor. For the purpose of this thesis, it involves subjecting the hydrocracking catalyst to F-T conditions. Synthesis gas (carbon monoxide and hydrogen), the paraffin n-C_{16} and water were co-currently fed to a fixed-bed reactor containing only the hydrocracking catalyst. Therefore care was taken to match the experimental conditions of the hydrocracking experiments to those that prevail in the Fischer-Tropsch synthesis. Practically this means the hydrocracking of n-hexadecane was studied at the space velocity, the reaction temperature and pressure and under partial pressure of H_2, CO and water, at which n-hexadecane is produced in F-T process assuming that n-hexadecane is the only hydrocarbon product and that n-hexadecane is a model compound for the low temperature F-T process.

The results of this investigation show that the hydrocracking reaction over a Pd catalyst supported on H-MFI Zeolite under F-T conditions is non-ideal. At low feed (n-C_{16}) conversions, product distributions are strongly dominated by secondary reactions. The ability of the metal site is significantly inhibited by the presence of CO and water. The product distributions show exactly this due to the increase in unsaturated and more branched species. Feed conversion in the presence of water and CO increase with increasing reaction temperature. The absence of methane in the product spectrum is an indication that the hydrogenolysis reaction is an unfavorable pathway for the catalyst used. The data obtained from this investigation suggests that the combination of low temperature Fischer-Tropsch and hydrocracking into a single reaction step is feasible.

Acknowledgements

I would like to acknowledge the help and support of a few people without whom this dissertation would not have been successful.

I would like to thank my supervisors, Professor Jack Fletcher and Dr Roald Brosius. Professor Jack Fletcher has supported my studies since the first day and has guided and motivated me all the way. Jack always ensured that the research was on track and within the scope on this thesis. I will always be extremely grateful for the opportunity given to me. This thesis would not have been possible without the commitment from Roald. I want to thank him for all his hard work that he put into the construction of the apparatus and making the experiments run as efficiently and safely as possible. I would also like to thank him for all his support and guidance with the laboratory matters as well as his advice and insight with the write up of this thesis.

The help and support from the laboratory staff is exceedingly valued. I would also like to thank Mr Stehpen Roberts, Marc Wust, Jacobus and Waldo Koorts for all their assistance and guidance. It is much appreciated.

I would like to thank Chevron and c*change for providing financial support throughout this study. Many thanks to the University of Cape Town and the Department of Chemical Engineering for the use of their facilities and resources.

Declaration

I, the undersigned, hereby certify that this dissertation contains work that is my own research and interpretation completed with the assistance of my supervisors (indicated in the Acknowledgements). Any information which is not my own has been indicated as such and referenced in accordance with the Harvard referencing system.

Signed: _____

Name: _____

Date: _____

Table of Contents

Page

Synopsis ..... **i**

Table of Contents ..... **iv**

List of Figures ..... **vii**

List of Tables ..... **x**

Nomenclature ..... **xi**

Chapter 1: Introduction **1**

Chapter 2: Background **2**

2.1 Coal- or Gas-to-Liquids Production 2

2.2 Hydrocracking 5

2.2.1 Hydrocracking Catalysts 6

2.2.2 Zeolites 7

2.2.3 Metal-Acid Balance 8

2.2.4 Hydrocracking Mechanism 9

2.3 Catalyst Incorporation 12

2.4 Operating Variables 12

2.4.1 Temperature 13

2.4.2 Hydrogen : Hydrocarbon ratio 13

2.4.3 High CO Partial Pressure 14

2.4.4 High Water Partial Pressure 15

Chapter 3: Objective **16**

Chapter 4: Experimental 17

4.1 Experimental Apparatus and Design 17

4.2 Experimental Reaction Conditions 20

4.3 Catalyst Classification and Loading Procedure 22

4.4 Operating Procedure 24

4.5 Data Analysis using GC-FID and GC-MS 24

4.6 Calculation of Conversion and Selectivity 25

4.7 Experiments Conducted 28

4.8 Test Unit Commissioning 30

Chapter 5: Results 32

5.1 Effect of Temperature on n-C_{16} Hydrocracking 32

5.2 Effects of Co-Feeding Water and CO on n-C_{16} Hydrocracking 37

5.2.1 Pd01BHMFI 37

5.2.2 Pd10CHMFI 41

5.2.3 Influence of Temperature 45

5.2.4 Effects of CO and H2O on Product Selectivities at Equal Conversions 46

Chapter6: Discussion 47

6.1 n-C_{16} Hydrocracking - Correlation with Temperature 47

6.2 n-C_{16} Hydrocracking - Effect of CO Co-Feeding 50

6.3 n-C_{16} Hydrocracking - Effect of H_2O Co-Feeding 51

6.4 Compatibility of F-T Conditions and n-C_{16} Hydrocracking 52

Chapter 7: Conclusion 54

References 55

Appendix A – Post Reactor Effluent Vaporization 61

A.1 Introduction 61

A.2 Comparison of Improved System Designs 62

A.3 Obtaining a Steady State Flow of $C_{16}H_{34}$ to the FID; the Blank Run 63

A.4 Recommendations for Further Reducing Temperature Gradients 72

A.5 Application of the Improved Design to Two More Test Units 73

A.6 Co-feeding water and hexadecane 80

A.7 Conclusion 83

List of Figures

Page

Figure 2.1: The Process of Converting Natural Gas to Liquid Hydrocarbons via the Fischer-Tropsch Synthesis 3

Figure 2.2: Fischer-Tropsch Synthesis Product Selectivity as Predicted by the Anderson-Schulz-Flory Distribution 3

Figure 2.3: The Surface of the Zeolite Crystal showing Brönsted Acid and Lewis Base Sites..... 8

Figure 2.4: Representation of the Classical Bi-functional Hydrocracking Mechanism over Pt/Acid Catalyst 10

Figure 2.5: β-Scission Reactions Involving Secondary and Tertiary Carbenium Ions 10

Figure 2.6: Theoretical Carbon Number Distribution of Products from the Bi-functional (Metal/Acid) Hydrocracking of n-C_{14} 11

Figure 2.7: Conversions of CO as function of Reaction Temperature obtained over Rh, Ru, Pt and Pd catalysts (0.5 wt.%) supported on Al_2O_3 14

Figure 4.1: Process Flow Diagram of the Dual Tube Test Unit 18

Figure 4.2: Diagram of Reactor Housing Illustrating Heating Element Layout 19

Figure 4.3: Example of a Chromatogram obtained from GC-FID 25

Figure 4.4: C_{16} Peak Height for Blank Run with Water Inlet Modification 31

Figure 4.5: Temperature Profile of the Vaporizer Section 31

Figure 5.1: TOS Data for n-C_{16} Conversion over Pd/SiO_2 + HMFI-90 (Experiment A: $Pd10_AHMFI$) 32

Figure 5.2: Conversion versus Temperature of n-C_{16} Hydrocracking (Experiment A: $Pd10_AHMFI$) 33

Figure 5.3 (a), (b) and (c): Selectivity versus Carbon Number at 225°C, 215°C and 205°C (Experiment A: $Pd10_AHMFI$) 34

Figure 5.4: Total Product Distribution versus Carbon Number (Experiment A: $Pd10_AHMFI$) 35

Figure 5.5 (a) and (b): Selectivity versus Carbon Number in the Absence and Presence of CO at 225°C (Experiment A: $Pd10_AHMFI$) 36

Figure 5.6: Effect of co-feeding CO to the hydrocracking reaction (Experiment A: $Pd10_AHMFI$) 37

Figure 5.7: Conversion versus TOS of n-C_{16} Hydrocracking (Experiment B: $Pd01_BHMFI$) 38

Figure 5.8: Effects of Co-Feeding H_2O, CO on Hydrocracking Reaction (Experiment B: $Pd01_BHMFI$) 39

Figures 5.9 (a), (b) and (c): Effects of co-feeding H_2O, CO on hydrocracking (Experiment B: $Pd01_BHMFI$) 40

Figure 5.10: Conversion of n-C_{16} versus Time-On-Stream (Experiment C: $Pd10_CHMFI$) 41

Figure 5.11: Effects of co-feeding H_2O, CO on Hydrocracking (Experiment C: $Pd10_CHMFI$) 43

Figures 5.12 (a), (b) and (c): Effects of co-feeding H_2O, CO on n-C_{16} hydrocracking (Experiment C: $Pd10_CHMFI$) 44

Figure 5.13: Effects of co-feeding CO and H_2O on (a) $Pd01_BHMFI$ (open symbols) and (b) $Pd10_CHMFI$ (closed symbols) in normal hydrocracking (triangles), with CO co-feeding (diamonds) and with CO together with H_2O co-feeding (squares). 45

Figure 5.14: Selectivity per Carbon Number Fraction versus Carbon Number for Experiments B.2 (46.0% Conversion), C.6 (45.9% Conversion) and C.4 (42.6% Conversion) 46

Figure 6.1: Yield of Isomerisation and Cracking Products for the Bi-functional (Metal/Acid) Hydrocracking of a Long n-Alkane (Taken from Kukard, 2008) 48

Figure 6.2: Observed Isomerisation and Cracking Yield over Hydrocracking catalyst under Low Temperature Conditions (Experiment A: Pd10AHMFI) 49

Figure A.1: Initial Design 61

Figure A.2: Improved System Design A 62

Figure A.3: Alternative Improved System Design B 63

Figure A.4: Representation of Observed Chromatographic Scatter when Filter is Heated 65

Figure A.5: $C_{16}H_{34}$ Chromatographic Reproducibility in the Absence of the Filter 65

Figure A.6: Chromatographic Representation of Condensation in the Sample Loop 66

Figure A.7: Chromatographic Reproducibility at a Sample Loop Temperature of 250°C 66

Figure A.8: Chromatographic Reproducibility with Reduced Dilution Flow of 250 sccm 67

Figure A.9: Chromatographic Reproducibility with Dilution Gas Flow Rate and Feed Gas Flow Rate Exchanged 68

Figure A.10: Chromatographic Reproducibility with the T-Piece of the Dilution Entry Point at an Angled Position, Scatter Observed 69

Figure A.11: Chromatographic Reproducibility with the Vaporizer Temperature Lowered to 250°C 69

Figure A.12: Chromatographic Reproducibility showing No Significant Improvement with the Redesigned Heating Arrangement 70

Figure A.13: Chromatographic Representation at 'High' n-C_{16} Feed Flow Rate 71

Figure A.14: Chromatographic Reproducibility with Increased Split Flow in the GC Injector 71

Figure A.15: Vaporizer Temperature Profile 72

Figure A.16 (a), (b), (c) and (d): Chromatographic Comparison of the Output from Identical Test Units and their Vaporizer Temperature Profiles. 74

Figure A.17: Illustration of How Dilution at Too High Temperature Leads to Complete Vaporization 76

Figure A.18 (a), (b), (c) and (d): Final Results from All Reactor Tubes 79

Figure A.19: Chromatographic Reproducibility with High Flow Rate of Gas at the Reactor Entry and a Steep Temperature Gradient: Scatter Observed 80

Figure A.20: Chromatographic Representation of Observed Scatter due to co-feeding of H_2O and n-C_{16} 81

Figure A.21: Chromatographic Reproducibility with Introducing Water through a Dip-Tube 82

Figure A.22: Total Peak Height and n-C_{16} Peak Height versus Time-On-Stream show the Quality of the Data (Experiment B: $Pd01_BHMFI$) 83

List of Tables

Page

Table 2. 1: Comparison of the Various Hydrocracking Technologies used in Industry 6

Table 4. 1: Suppliers of Equipment and Instrumentation used for this research..... 20

Table 4.2: Calculation of a Hypothetical n-C_{16} Formation Rate from F-T and the Corresponding H_2O Formation Rate and their Volumetric Flow Rate Equivalents ... 21

Table 4.3: Catalyst and Reagent Suppliers..... 22

Table 4.4: Catalyst Loading Masses 23

Table 4.5: Experiment A ($Pd10_AHMFI$)..... 28

Table 4.6: Experiment B ($Pd01_BHMFI$) 28

Table 4.7: Experiment C ($Pd10_CHMFI$) 29

Table 5.1: Conversion at Different Experimental Settings..... 38

Table 5.2: Conversion at Different Experimental Conditions ($Pd10_CHMFI$) 42

Table 6.1: Partial Pressures during the n-C_{16} Hydrocracking Experiments: 1) Normal Hydrocracking Conditions, 2) Co-Feeding of CO, 3) Co-Feeding of CO and H_2O 51

Table 6.2: Comparison of Hydrocracking Reaction Rates on $Pd10_CHMFI$ Catalyst with the Rate of Formation of Hydrocarbons in F-T synthesis over Cobalt Catalysts. 53

Table A.1: Partial and Vapor Pressure of C_{16} 74

Table A.2: An overview of the C_{16} partition over the different phases 77

Nomenclature

A_i	GC peak Areas Corresponding to Individual Hydrocarbon Species i
CH_4 or C_1	Methane
C_i	Concentration of Iso- and Normal Paraffins of Species i
FID	Flame Ionization Detector
F-T	Fischer-Tropsch
GC	Gas Chromatograph / Gas Chromatography
GTL	Gas-to-Liquids Process
H_2:n-C_{16}	Hydrogen to n-Hexadecane Molar Ratio
LHSV	Liquid Hourly Space Velocity
WHSV	Weight Hourly Space Velocity
LPG	Liquid Petroleum Gas
min	Minute
M_w	Molecular Weight
n-C_{16}	n-Hexadecane
n-C_i	Normal Paraffins of Species i
NC_i	Number of Carbon Atoms in the Respective Compound i
n_i	Number of Moles of Species i
P	Pressure
sccm	Standard cubic centimeters per minute
SC_i	Molar Selectivity of the Respective Compound i
SMDS	Shell Middle Distillate Synthesis
SO_x	Sulphur Oxides
T	Temperature
TOS	Time-On-Stream
hr	Hour
wt	Weight
X	Conversion

Introduction 1

Due to increasing environmental concern and legislation, the demand for low sulphur diesel has increased dramatically. The transportation fuel system has been placed under severe pressure due to environmental problems, high oil prices as well as insecurities in the stability of the crude oil supply. Therefore, the search for alternative clean fuels is ongoing. These alternatives include biodiesel, ethanol, hydrogen, LPG and di-methyl-ether. Although these alternatives allow for the lowest emissions of greenhouse gases, the changes required in the vehicles' engines may be substantial.

Diesel fuel (C_{10} – C_{20}) can be produced by refining crude oil or from the Fischer-Tropsch (F-T) based Gas-to-Liquids (GTL) processing. The concept of sulphur free synthetic diesel is part of the next step towards cleaner transportation fuels and improved air quality. Synthetic diesel, produced from natural gas, has many advantages including high cetane number, low particulate formation and low NO_x and CO emission. This idea is very appealing in countries having large natural gas reserves and countries having no major pipelines to other countries.

The ability to combine the F-T synthesis process with the selective F-T wax hydrocracking step creates an opportunity for improvement of overall Gas-to-Liquids processing. The objective of this project is an initial investigation into the potential for single-stage combined low temperature F-T synthesis / hydrocracking. As such the project will focus on evaluating hydrocracking performance at conditions typical of cobalt catalyzed F-T synthesis, inter alia the temperature (230 – 240˚C), pressure (20 – 30 bar) and H_2/oil molar ratio (0.5 – 5) typical of low-temperature F-T processing.

Background 2

2.1 Coal- or Gas-to-Liquids Production

It is expected that due to limited reserves of crude oil and stringent environmental constraints, the feedstock for the chemical industry will shift from crude oil to natural gas. The diesel produced via the F-T synthesis is well suited to the current market, is fully compatible with existing vehicles, has a high cetane number and is free of sulphur and nitrogen.

The Fischer-Tropsch process is a crucial step in converting natural gas (methane) or coal into "petroleum products". The Fischer-Tropsch process was developed in Germany in the 1920's where coal was especially abundant. Since then, interest in and development of the process has fluctuated but in the last 30 years it has experienced renewed interest and more research and development. The Fischer-Tropsch synthesis constitutes a practical way for the chemical liquefaction of solid (coal) or gaseous (natural gas) carbon resources. In relation to traditional crude oil refining, the liquefaction of these carbon sources via the Fischer-Tropsch synthesis provides alternative routes for the production of transportation fuels and petrochemical feedstocks.

While the commercial operation of Fischer-Tropsch plants is currently limited to three companies, i.e. Sasol (South Africa and Qatar), Shell (Malaysia) and PetroSA (South Africa), the interest in the Fischer-Tropsch technology is increasing. Exxon now also offer a process for hydrocracking F-T wax into liquid oils and the Sasol/Chevron plant in Nigeria is aimed at producing maximum diesel fuel with a cetane number greater than 70.

The main steps of the gas based F-T process are illustrated in Figure 2.1. The feed, natural gas, is converted via the process of steam reforming to produce syngas, H_2 and CO via the following reaction:

$$CH_4 + H_2O \rightarrow CO + 3H_2$$

The syngas is then converted to long chain hydrocarbons via the F-T synthesis, using an F-T catalyst. Operating conditions include reaction temperatures ranging from 200 to 350°C and reaction pressures between 20 – 40 bar (Möller et al., 2009).

Figure 2.1: The Process of Converting Natural Gas to Liquid Hydrocarbons via the Fischer-Tropsch Synthesis

The two main types of the F-T process include the low-temperature (LTFT) and the high-temperature (HTFT) processes. The products from the high temperature iron based F-T synthesis are light hydrocarbons and of olefinic nature. Products from the low-temperature cobalt-based Fischer-Tropsch synthesis are essentially long-chain paraffins (waxes).

The maximum yield of the straight run middle distillate fuels (jet fuel and diesel) reaches only approximately 35 wt.%. This is seen in Figure 2.2.

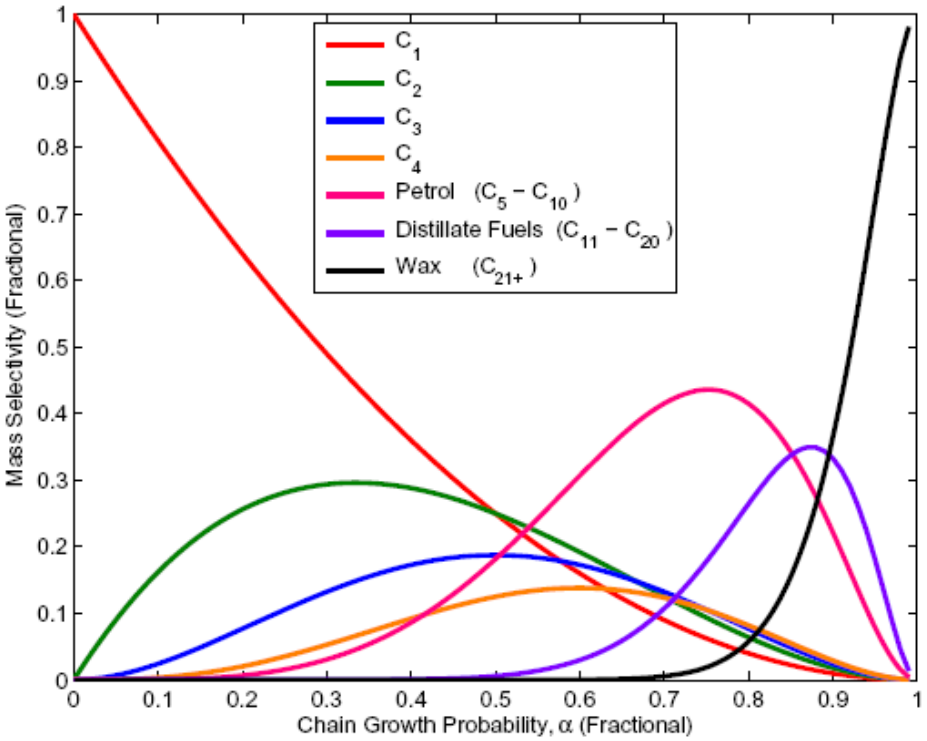

Figure 2.2: Fischer-Tropsch Synthesis Product Selectivity as Predicted by the Anderson-Schulz-Flory Distribution (Taken from Fletcher et al., 2004)

An intrinsic feature of the F-T synthesis is the low selectivity towards the middle distillate fraction whose production is always associated with the generation of less desirable products that are gasoline and wax. One consequence of the chemical nature of the F-T products is that their cold flow properties will be very poor. A suitable way to improve both the yields and quality of middle distillate is to subject the F-T products to a hydrocracking process.

The Fischer-Tropsch waxes are hydrocracked to produce preferably diesel and kerosene fractions. The diesel produced by this process of hydrocracking has a cetane number of more than 74 with zero sulphur content (Kumar and Froment, 2007).

Due to the dramatic increase in crude oil price and the concern for crude oil reserves, interest in alternative energy resources have grown rapidly over the past few years. There has been substantial growth in proven natural gas reserves around the world. Gas is a clean source of fuel and thus desirable due to the environmental concern and stringent legislation. Since the late 1940's, the Royal Dutch/Shell company has conducted research into the conversion of natural gas to liquid transportation fuels. In August 1989, it was announced that the world's first commercial SMDS plant would be built in Malaysia and it came on stream in 1992 (Sie et al., 1991). The SMDS technology produces fuel with virtually no sulphur and aromatic compounds.

The SMDS process consists of three steps:

- Conversion of natural gas to synthesis gas

Syngas is produced by the partial oxidation of natural gas with oxygen.

- Conversion of syngas to normal paraffins (Heavy Paraffin Synthesis HPS)

The syngas components H_2 and CO are consumed in the ratio 2:1 to produce hydrocarbons using a highly modified version of the classical Fischer-Tropsch synthesis. The product slate ranges from very light paraffins to heavy paraffinic waxes. The catalyst used by Shell is very robust and has a high selectivity towards the heavy paraffinic waxes (Sie et al., 1991).

- Conversion of normal paraffins to middle distillates (Heavy Paraffin Conversion HPC)

During HPC the heavy paraffinic wax is selectively hydrocracked to produce a maximum yield of middle distillates of high quality. The hydrocracking process is a mild trickle-flow process operating typically at 30 – 50 bar total pressure and between temperatures of 300 – 350°C (Eilers et al., 1990).

2.2 Hydrocracking

Classic hydrocracking as practiced in oil refining is a bi-functional process that requires metal as well as acid sites. Saturated hydrocarbons are dehydrogenated on the metal sites; subsequently, the unsaturated species migrate to the acid sites where they are protonated, yielding carbenium ions. Such carbenium ions undergo further isomerization and cracking reactions. The product carbenium ions desorb as alkenes that are hydrogenated into the observed saturated species. Prior to these chemical steps, physisorption occurs in the micropores of the catalyst.

Hydrocracking is achieved at high hydrogen partial pressure and high temperature. The hydrocracking process is carried out in two stages, the first to reduce the amount of nitrogen, sulphur and oxygen impurities that may reach the second stage catalyst, and the second to continue the process of cracking, hydrogenating and isomerising the compounds in the oil. The bi-functional mechanism of hydrocracking and hydroisomerisation of long chain paraffins has been reviewed in detail elsewhere (Kumar and Froment, 2007).

The metal site catalyzes the hydrogenation/dehydrogenation activity and the acid site catalyzes the hydroisomerisation and hydrocracking. The metal function is generally provided by platinum or palladium, whereas the acid function is provided by zeolites. The current suggestion is to achieve in situ, hydrocracking of wax from the low-temperature Fischer-Tropsch synthesis by combining the Fischer-Tropsch synthesis and the hydrocracking process into a single reactor. This involves subjecting the hydrocracking process to Fischer-Tropsch conditions including:

- Low temperature (200 - 240°C)
- Presence of CO
- High H_2 to oil ratio
- Presence of water

A few studies have been conducted to investigate the hydrocracking of paraffins over a bi-functional catalyst. Fernandes and Teles (2007) presented a model for the hydrocracking of low-temperature Cobalt-based Fischer-Tropsch product consisting of a C_4 – C_{30} mixture of paraffins where the main product fractions are gasoline, diesel and kerosene. Diesel-selective hydrocracking of iron-based Fischer-Tropsch wax using a noble metal modified catalyst has contributed to literature together with other studies on the influence of chain length, temperature and feed ratios on the hydrocracking of long-chain paraffins (Leckel, 2005; Fernandes et al., 2007; Weitkamp et al., 1983). Table 2.1 below summarizes the various hydrocracking technologies used in industry together with the current study.

Table 2. 1: Comparison of the Various Hydrocracking Technologies used in Industry

	Operating Conditions	Catalyst used	Feed	Effect of Operating Conditions
"Classic" Hydrocracking	350 – 450°C, 100 – 140 bar	Bifunctional, e.g. Pt/H-Y	Heavy Gas Oils	Maximum Middle Distillate Yield
Shell Middle Distillate Synthesis	300 – 350°C, 30 – 50 bar	Non-disclosed	FT product ranging from light paraffins to heavy waxes	Maximum Middle Distillate Yield
FT wax Hydrocracking	320 – 380°C, 35 – 60 bar	Pt supported on SiO_2/Al_2O_3 (MSA) Or NiMo on SiO_2/Al_2O_3	FT wax (long chain hydrocarbons)	High temperatures and pressures produce light gas and gasoline cuts, lower temperatures and pressures favors mild hydrocracking , yielding a product with higher percentage of diesel
Hydrocracking under FT conditions	225°C, 20 bar	Pd/SiO2 in combination with H-MFI zeolite	FT wax model compound n-C_{16}, Water and CO	Non-ideal behavior with high yield in the lower carbon number range

2.2.1 Hydrocracking Catalysts

Hydrocracking catalysts are dual function catalysts. They consist of two main constituents, the acid site and the metal site. The acidic site provides the isomerization and cracking, whereas the metal site accommodates the hydrogenation/dehydrogenation function (Fernandes and Teles, 2007).

The acidic site can either be an amorphous mixed oxide such as silica-alumina, a zeolite or a combination of the amorphous oxide and zeolite. Various metals have been employed for the hydrocracking of long chain paraffins:

- Noble metals including platinum and palladium
- Non-noble transition metals from group VIA and group VIIIA, notably nickel, cobalt and molybdenum.

2.2.2 Zeolites

The chemical industries are continuously confronted with more severe product specifications, the need for more environmentally friendly processes and the development of new fuels and chemicals. The answer to these requirements is the use of hyper-selective catalysts. Zeolites, having their pores of molecular size, are well known for their high catalytic activity and high specificity (Denayer et al., 2003).

Zeolites are used in many industries including catalysis, ion exchange and gas separation. The most important use for zeolites in catalysis is that of hydroisomerisation and hydrocracking of hydrocarbons. It is due to their shape selectivity and remarkable properties of their active sites that these catalysts are preferred. Zeolites are 3-dimensional, microporous, crystalline structures (similar to a honeycomb) consisting of interconnected channels and cages. Zeolites have a molecular sieving property whereby they can separate smaller molecules from larger molecules. Due to the wide pore structure of the preferred Zeolite-Y, these catalysts are suitable for the hydroconversion of heavy feedstocks. There are nearly 50 different types of zeolites with different physical and chemical properties including crystal structure and chemical composition. Other properties that can differ include particle density, pore size and acid strength. Zeolites are preferred over their amorphous catalyst counterparts due to their more severe cracking function. Other advantages of the acid zeolites include better thermal stability, better resistance to sulphur and nitrogen compounds and a low tendency to coke. Zeolite Y, ZSM-5, mordenite and beta are a few of the zeolites most commonly used in the hydroconversion processes.

2.2.3 Metal-Acid Balance

The number of acid sites as well as the strength of the acid sites contributes to the overall activity of H-Zeolite catalyst. This is also related to the SiO_2/Al_2O_3 ratio of the framework (Figure 2.3). A low SiO_2/Al_2O_3 ratio results in a high number of acid sites but with each of low individual acid strength. This causes the overall acidity to be low and thus low activity of the catalyst. On the other hand, a high SiO_2/Al_2O_3 ratio leads to less acid sites but of increased acid strength, increasing the overall catalyst acidity and thus activity. When the ratio becomes too high, the low number of acid sites, although having high individual acidity, will result in low overall acidity and thus activity (Kukard, 2008). The strength of the Brønsted acid site is determined by the strength of the O-H bond. A weak O-H bond relates to a strong acid site.

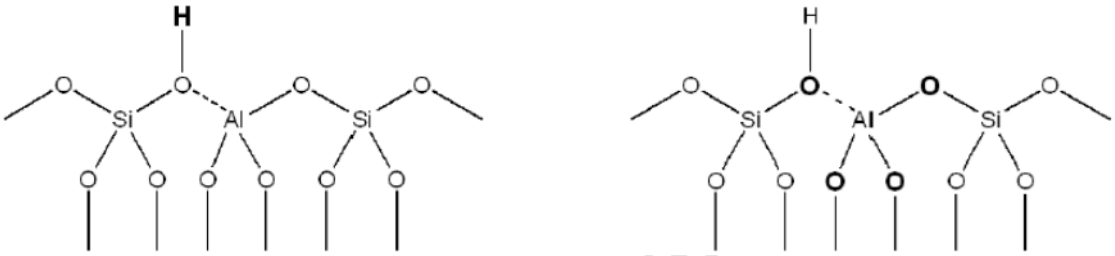

(a) Brønsted acidity due to weakening of the O-H bond

(b) Lewis basicity of the Al oxo-ligands due to weakening of the Al-O bonds

Figure 2.3: The Surface of the Zeolite Crystal showing Brönsted Acid and Lewis Base Sites (Taken from Kukard, 2008)

Secondary cracking of primary cracked products occurs with increased overall strength of the acid function of the catalyst. Secondary cracking results in the increased formation of products in the lighter carbon number range. According to the bi-functional mechanism, the cracked product would be hydrogenated on the metal function. Depending on the number of acid sites and mass transfer effects, the cracked product could go to another acid site before going to the metal site, thereby undergoing further cracking. This is also observed on stronger acid sites. The cracking products could undergo a number of cracking reactions before being rehydrogenated on the metal site. "True" hydrocracking is observed where there are sufficient metal sites to rapidly rehydrogenate the cracking products and thus quench the cracking reactions (Kukard, 2008). In the study conducted by Thybaut et al. (2005) on the acid – metal balance of a hydrocracking catalyst, it is stated that the balance between the number and the strength of the metal and acid sites plays a key role in the product selectivities observed. The term 'ideal hydrocracking' is used for situations where the primary cracked products are rapidly hydrogenated to avoid further (secondary and tertiary) cracking products.

2.2.4 Hydrocracking Mechanism

Liquid fuel production from coal dates back to 1915, when the development of the hydrocracking process started in Germany. Today hydrocrackers are directed towards the production of exceptionally low sulphur diesel. Synthesis gas from the Sasol Lurgi gasifiers undergoes several steps to remove impurities such as sulphur and nitrogen which are common poisons to catalysts. Hence, the products from the Fischer-Tropsch synthesis are an environmentally clean source for distillate fuels. Low-temperature Fischer-Tropsch waxes contain essentially linear paraffins (95%), smaller amounts of olefins and oxygenates, and no sulphur or aromatics making these waxes suitable for high quality transportation fuels (Leckel, 2007).

The hydrocracking of Fischer-Tropsch wax using bi-functional catalysts has been studied extensively at Sasol in the 1970's (Leckel, 2007). A high-quality Fischer-Tropsch diesel can be produced by applying low pressure hydrocracking with a well-balanced bi-functional catalyst (i.e. a catalyst having sufficient metal activity).

The mechanism of hydrocracking over bi-functional catalysts is essentially the breaking of the C-C bond in a carbon chain followed by the saturation of the resulting fragments through the addition of hydrogen. This mechanism relies on the carbenium ion mechanism whereby the n-paraffin undergoes a series of steps including hydrogenation/dehydrogenation and skeletal isomerisation. The paraffins are absorbed into the pores of the zeolites from the surrounding phase (gas or liquid) where it is chemisorbed onto the metal site.

The paraffin is then dehydrogenated to form the corresponding olefinic intermediate. The olefin migrates from the metal site to the acidic site of the catalyst where it is protonated into a carbenium ion. The carbenium ion is isomerised and cracked at the carbon–carbon bond in the β position with respect to the carbon atom carrying the positive charge, yielding a smaller carbenium ion and an olefin (Kumar and Froment, 2007). See Figure 2.4 for schematic illustration of the mechanism.

The resulting carbenium ion can crack further or deprotonate on the acid site to form an olefin. The resulting olefin can be protonated to yield another carbenium ion or be hydrogenated on the metal site to form a paraffin. The relative strength of the acid/metal functions of the catalyst determines which route the intermediates will follow (Kumar and Froment, 2006). The β-Scission mechanism suggests that the n-paraffins submitted to hydrocracking undergo several isomerisations until a favorable configuration is attained. The cracking of the isomers occurs near the center of the hydrocarbon chain. Smaller carbenium ions and olefins are formed via the β-Scission mechanism. For large carbenium ions, the cracking with β-scission occurs with di- and tri-branched isomers. This mechanism is also known to be the rate limiting step.

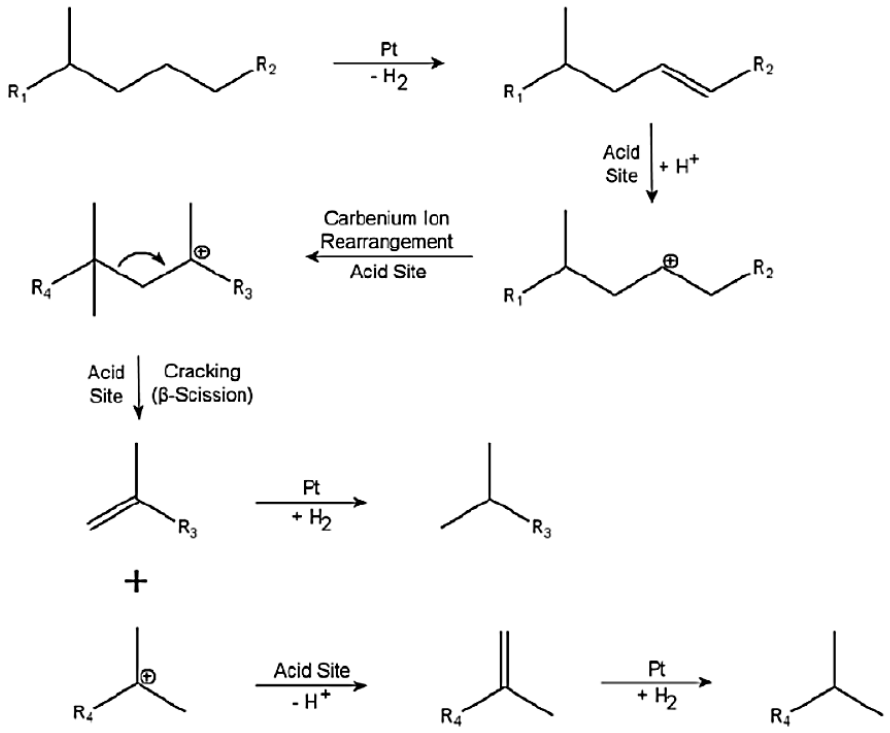

Figure 2.4: Representation of the Classical Bi-functional Hydrocracking Mechanism over Pt/Acid Catalyst (Taken from Weitkamp et al., 1983)

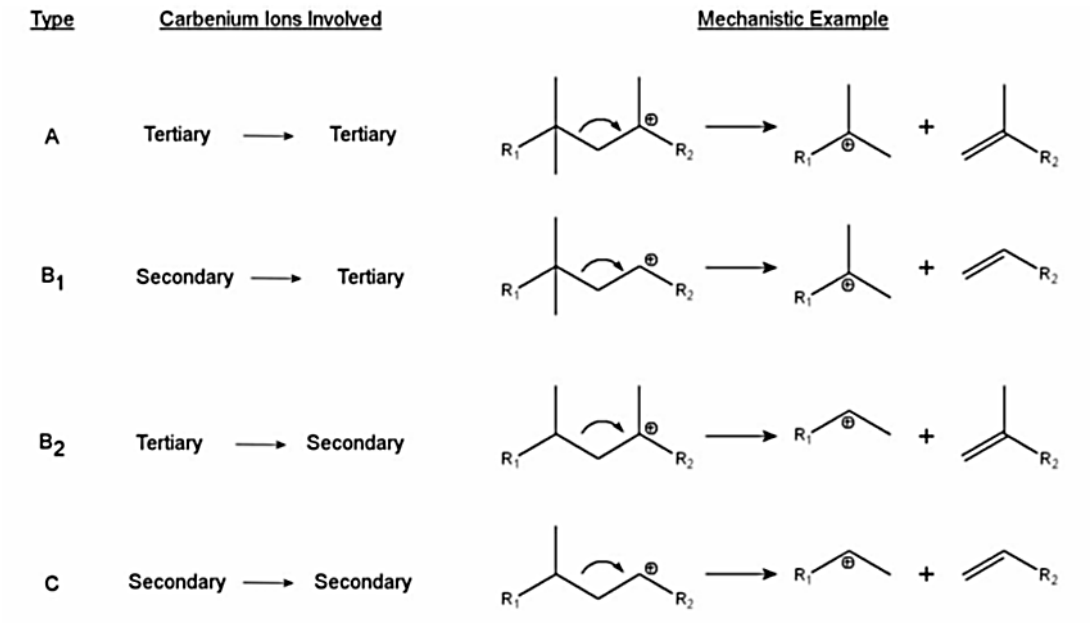

Figure 2.5: β-Scission Reactions Involving Secondary and Tertiary Carbenium Ions (Taken from Weitkamp et al., 1983)

Figure 2.5 illustrates examples of β-scission reactions that involve tertiary and secondary carbenium ions. The tertiary–tertiary mechanism is said to occur more rapidly than the other mechanisms illustrated in the figure, with the ranking of the order A » B1, B2 > C.

The type A cracking mechanism will only occur on internal C-C bonds and thus with equal reactivity. This will result in an even product distribution with fragments smaller than C_4 not favored. Type A cracking illustrates the ideal primary cracking reaction, i.e. no re-absorption or secondary cracking will occur. The formation of C_2 and C_3 occur to a much smaller extent and the formation of C_1 does not occur. These trends are illustrated in Figure 2.6 (solid line) for an n-tetradecane (n-C_{14}) feedstock.

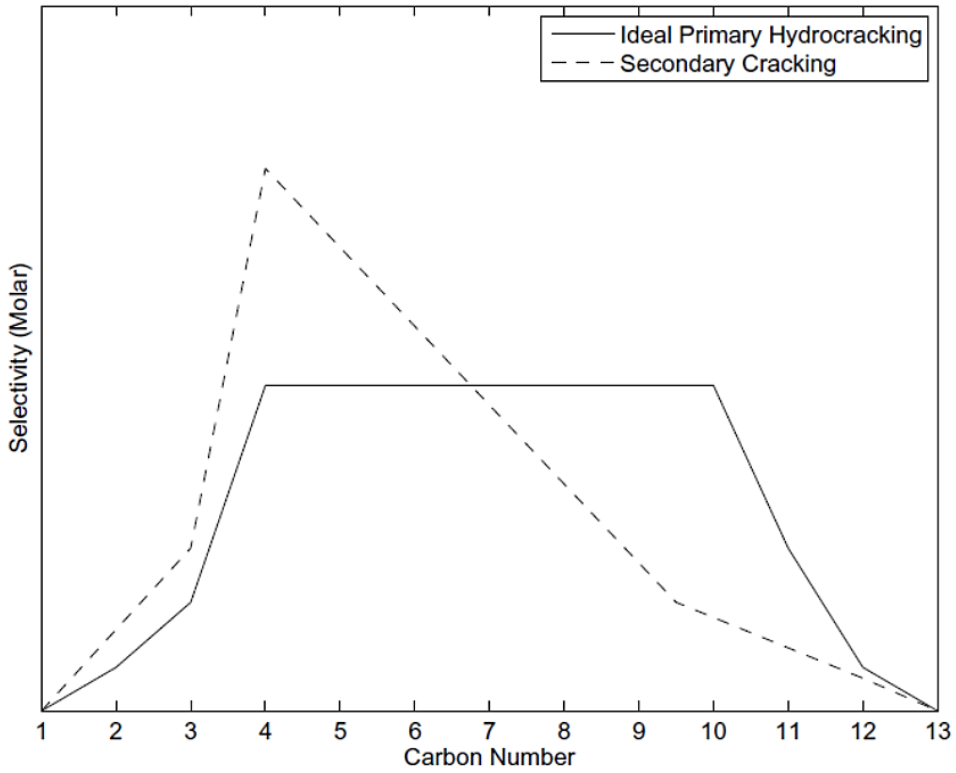

Figure 2.6: Theoretical Carbon Number Distribution of Products from the Bi-functional (Metal/Acid) Hydrocracking of n-C_{14} (Taken from Kotsiopoulos, 2005)

Secondary cracking occurs at higher conversions where primary products are cracked further. This is illustrated in Figure 2.6 by the dotted line. The carbon number distribution is seen to drift away from that of ideal cracking and shifted towards a maximum in the lower carbon number range. This increase in the selectivity of shorter chains is due to the high cracking selectivity of the highly branched isomerisation products. Higher conversion, i.e. secondary cracking, is favored at higher reaction temperatures and lower pressures.

2.3 Catalyst Incorporation

Research into the improvement of hydrocracking catalysts and reactor design is an ongoing process. Acid catalysts loaded with a noble metal show high selectivity for the conversion of the heavy fractions from the F-T synthesis to middle distillates. Noble metal loaded zeolite catalysts are used as dual function hydrocracking catalysts to convert the heavy fractions to lighter more valuable fractions. According to Weitkamp and Ernst (1998), a catalyst loaded with noble metal shows high selectivity for hydroisomerisation giving a good product distribution, better than that of a transition metal (Ni, Co, Mo or W).

Industrially zeolites (almost exclusively Zeolite Y) are used to achieve 'severe' hydrocracking as is the case when high gasoline selectivity is desired and / or the feedstock is highly refractive. Medium-pore zeolites, e.g. MFI-types, have limited application in refinery hydrocracking due to their inability to process large, 'bulky' molecules. These zeolites are applicable to the linear paraffinic nature of F-T wax and may be of advantage in limiting the extent of branching and so serve to maintain molecular linearity and its associated high cetane properties (Fletcher et al., 2004). Therefore, for this research, H-MFI loaded with palladium is considered the most suitable hydrocracking catalyst to achieve mild hydrocracking of the paraffinic feedstock n-hexadecane with high middle distillate selectivity. The catalyst is in the form of 1/16" extrudates with length of 0.5 – 0.85 mm.

Due to the potential for the combination of the F-T synthesis and the subsequent hydrocracking step, it is of importance to determine the effect of the F-T conditions on the hydrocracking catalyst used. Conditions such as low temperature and the presence of CO and water were applied to test the activity of the catalyst used and thus the deactivation thereof if any.

2.4 Operating Variables

Operating conditions including temperature, hydrogen partial pressure, space velocity, hydrocarbon chain length, feed/recycle ratio and others have a significant impact on the yield and quality of the resulting products. Thybaut et al. (2005) states that operating conditions and the acid-metal ratio strongly affect the ideality of the hydrocracking reaction. Non-ideal hydrocracking is favored under conditions including decreased total pressure, increased reaction temperature, increased hydrogen – hydrocarbon ratio and longer hydrocarbon chains.

2.4.1 Temperature

In crude oil refinery hydrocracking, a change in reaction temperature can shift the maximum yield from naphtha to jet fuel or diesel. The typical hydrocracking temperature is approximately 400°C. According to Chavarria et al. (2004), temperature has the biggest effect on wax hydrocracking conversion, when compared to pressure and hydrogen-hydrocarbon ratio. When the objective is to produce a product in the higher boiling range, the operation severity is decreased. Thus by decreasing reactor temperature, the maximum yield is shifted from naphtha to jet or diesel fuel (Scherzer and Gruia, 1996). The study of Fernandes and Teles (2007) indicates that during hydrocracking of long-chain paraffins, an increase in temperature results in increased formation of lighter products but with a narrow hydrocarbon product distribution. High temperatures produce a great amount of light gas and gasoline, leaving very little in the way of heavier paraffins. Low temperatures in the range of 200 – 250°C favor mild hydrocracking, yielding a product with a high percentage diesel as only the long chain hydrocarbons undergo cracking.

Temperature effects on the hydrocracking of long chain paraffins are also influenced by the choice of catalyst. Leckel (2005) investigated the hydrocracking of n-hexadecane with a Siral-based catalyst, i.e. an amorphous silica-alumina catalyst. He states that the Brönsted acid sites influence the final hydrocracking activity of the catalyst. The catalyst with the larger number of acid sites will require a lower temperature to attain the same conversion as a catalyst with less acid sites (Leckel, 2005). Zeolite catalysts show a greater acidity and reactivity than their amorphous counterpart and therefore can achieve the same conversion at lower temperatures (Scherzer and Gruia, 1996).

2.4.2 Hydrogen : Hydrocarbon ratio

The typical hydrogen-hydrocarbon ratio during crude oil refinery hydrocracking is 10:1 on a molar basis; in the Fischer-Tropsch reactor it is much higher. Hydrogen-hydrocarbon ratio is analogous to the hydrogen partial pressure. It is stated by Leckel (2007) that isomerisation of long chain alkanes and thus the hydrocracking rate with a commercial hydrocracking catalyst NiMo on silica-alumina, increases at operating pressures between 20 – 40 bar. For the purpose of this study, the operating pressure is fixed at 20 bar as typical of industrial F-T synthesis. According to the hydrocracking mechanism on a bi-functional catalyst, the limiting step is the skeletal rearrangement of the secondary carbenium ion. An increase in hydrogen partial pressure, necessary for hydrogenation, will result in a decrease in the isomerisation (Leckel, 2007).

2.4.3 High CO Partial Pressure

Noble metals such as palladium, iridium and platinum are active CO hydrogenation catalysts producing mainly methane (van Gruijthuijsen et al., 1997).

$$CO + 3H_2 \rightarrow CH_4 + H_2O$$

The methanation of CO has been investigated by Panagiotopoulou et al. (2008). A variety of supported metal catalysts have been used, including noble metals such as platinum and palladium. The results from their study show that the hydrogenation of CO increases with increasing temperature for palladium catalysts (see Figure 2.7). For temperatures as low as 200 to 300°C the hydrogenation of CO is negligible. For the purpose of this study we selected to use Pd as the metal function as to minimize methane formation.

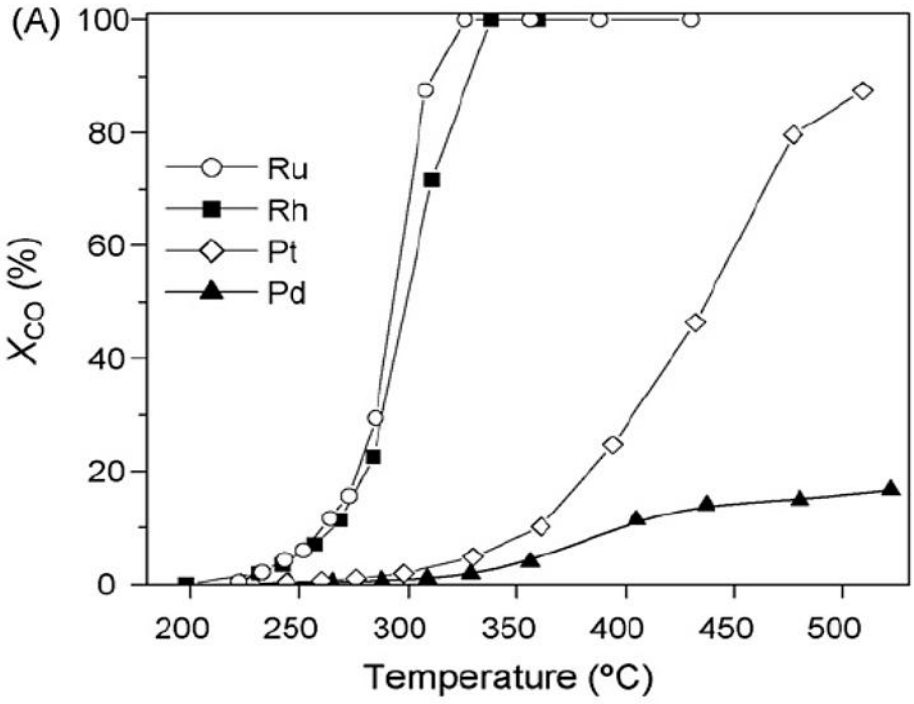

Figure 2.7: Conversions of CO as function of Reaction Temperature obtained over Rh, Ru, Pt and Pd catalysts (0.5 wt.%) supported on Al_2O_3 (Taken from Panagiotopoulou et al., 2008)

2.4.4 High Water Partial Pressure

Zeolites with high silica content are said to be hydrophobic in nature. Hydrophobicity is recognized as the tendency to repel and not to absorb water. At low pressures, hardly any water molecules exist in the pores (Ramachandran et al., 2006). The interaction of water with HZSM-5 has been studied by Olsen et al. (2000). They report that at low pressure the amount of water adsorbed decreases as the SiO_2/Al_2O_3 ratio increases. This indicates that there is a direct proportional relationship between the aluminum content and the amount of water adsorbed. They also report that the amount adsorbed is less affected by the SiO_2/Al_2O_3 ratio at high pressure conditions. Thus from literature it is seen that highly siliceous zeolites are known to be truly hydrophobic.

Objective 3

GTL processing is becoming a popular way for the production of cleaner transportation fuels. Currently, commercial interest lies in the production of sulphur free diesel fuels from the GTL process via Fischer-Tropsch synthesis. The wax produced from the F-T synthesis is cracked further to produce a high cetane diesel fuel. Therefore, it is of interest to look at the potential of combining the F-T synthesis and the hydrocracking steps into a single reaction stage.

The objective of this study is to investigate the potential for including a hydrocracking function into such a combined F-T/hydrocracking stage and, hence, seeks specifically to determine the impact of LTFT conditions (which are largely fixed) on wax hydrocracking. These conditions include low reaction temperature, the presence of CO and the presence of water. A single fixed bed test unit, suitable not only for hydrocracking or F-T synthesis but also for combined F-T synthesis/hydrocracking, was constructed for this purpose and n-hexadecane was applied as a model wax compound.

Underlying this study is the hypothesis that the relatively high hydrocracking reaction rate compared to the relatively low F-T reaction rate is such that, despite depression of hydrocracking activity by partial CO (and possibly H_2O) poisoning, sufficient hydrocracking activity remains under LTFT conditions, thereby making possible a rational combination of both reactions in a single reaction stage.

Consequently, the following key questions may be posed to determine the validity of the above hypothesis and the practicability of the proposed F-T/hydrocracking process embodiment:

- Does CO depress hydrocracking activity and, if so, to what extent at typical LTFT conditions?
- Does F-T product water depress hydrocracking activity and, if so, to what extent at typical LTFT conditions?
- Does the Pd metal component of the hydrocracking catalyst affect a significant (deleterious) methanation of CO under typical LTFT conditions?
- Does the application of LTFT conditions significantly alter the nature of the products of hydrocracking, e.g. olefinicity, degree of branching and carbon-number distribution?

Experimental 4

4.1 Experimental Apparatus and Design

A process flow diagram of the experimental rig is shown in Figure 4.1. Although the construction of this test unit is not part of this work, the commissioning of it is an integral part of this dissertation. Considerable difficulties were experienced during the commissioning phase, primarily related to the vaporization of n-hexadecane with a view to obtaining a steady state output – low scatter in the sampling of the n-C_{16} – and reliable, reproducible data. A detailed description of the relevant components is given here, followed by a brief overview of the operating procedure. The chronology of how the rig became operational is laid out in the Appendix.

The wax model compound n-C_{16} (liquid phase) is fed from a feed pot to the reactor by means of a piston type (HPLC) pump. During the investigation of the effect of water on the activity of the hydrocracking catalyst, water is being fed also by means of piston type (HPLC) pump. Both the n-C_{16} and water feed pots are placed on separate balances.

The fixed bed trickle reactor used in this experimental research consists of a stainless steel cylindrical tube with an internal diameter of approximately 16.8 mm and having a length of 360 mm. A thermowell of approximately 3 mm outer diameter runs through the length of the reactor. Four rectangular heating bands surround the brass reactor block as shown in Figure 4.2. By sliding a thermocouple up the thermowell a temperature profile of the reactor was established which shows that the temperature does not vary along the length of the reactor tube except for the bottom 4 cm and the top 10 cm. The catalyst is positioned in this isothermal section by means of SiC filler granulates. The space above the catalyst is also filled with SiC to ensure that the liquid distributes evenly in the radial direction and no channeling occurs.

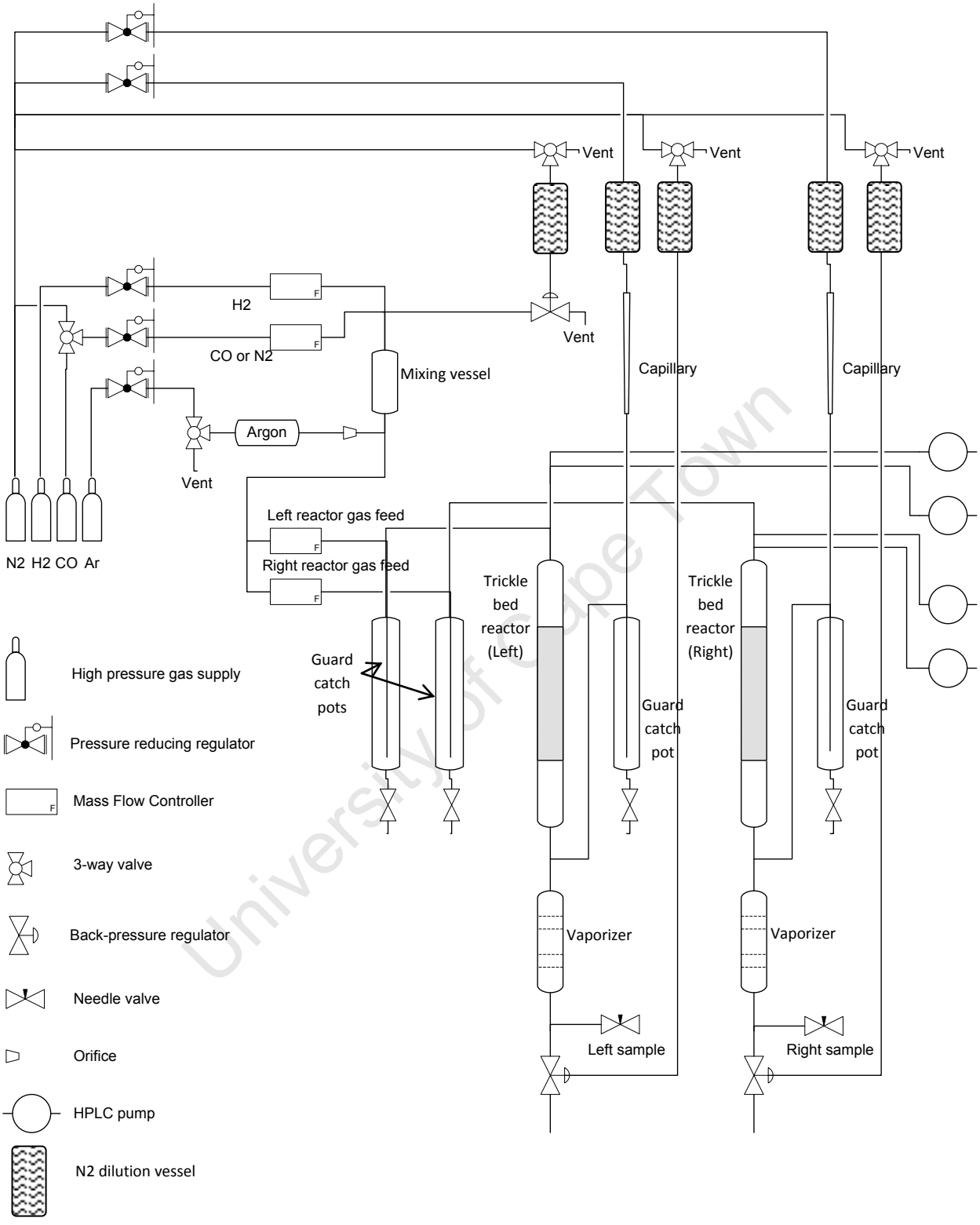

Figure 4.1: Process Flow Diagram of the Dual Tube Test Unit

The gas feed consisting of a mixture of H_2 and N_2 or H_2 and CO, and the dilution flow are administered to the reactor by means of thermal mass flow controllers (Brooks Instruments) with flow ranges of 0 to 500 ml/min. In the direction of the flow path the following instruments are encountered:

- Pressure reducing regulators placed upstream of the mass flow controllers are used to maintain the correct inlet pressure to the mass flow controllers.
- In-line filters are placed upstream of the mass flow controllers to prevent any particulates from entering the controllers.
- Beyond the mass flow controllers, the gaseous streams are passed through guard catch pots to prevent contamination of the controllers with liquid feed in the not so unlikely event that liquid would flow upstream due to a blockage.

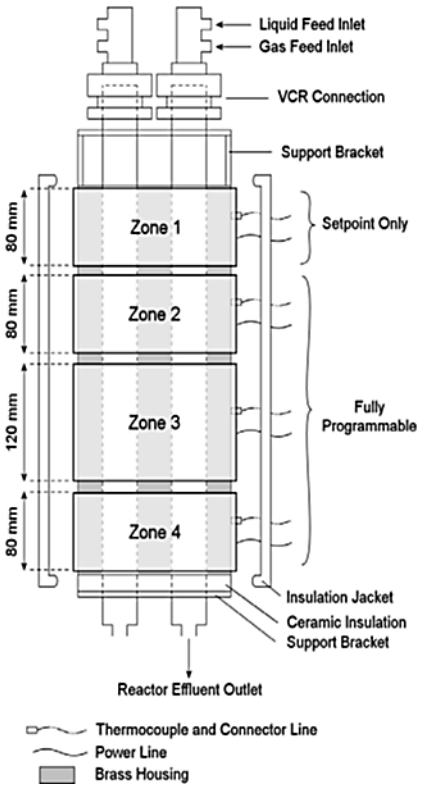

Figure 4.2: Diagram of Reactor Housing Illustrating Heating Element Layout (Taken from Kukard, 2008)

Along the path of flow, at the bottom of the reactor a T-junction is encountered where the nitrogen dilution gas is added to the reactor effluent. Further down, the role of the vaporizer is to ensure that the products from the reactor are all in the vapor phase when a sample is taken to the gas chromatograph for analysis. The vaporizer is packed with inert silicon carbide. Downstream of the vaporizer a back pressure regulator maintains the pressure upstream.

The table below summarizes the suppliers used to obtain the equipment and instrumentation used for this study.

Table 4.1: Suppliers of Equipment and Instrumentation used for this Study

Equipment	Supplier
Valves and Fittings	Swagelok South Africa
Electronic Components and Temperature Control Devices	UNITEMP
Piston Type HPLC pumps	ANATECH
Thermal Mass Flow Controllers	Brooks Instruments Supplied by Control Valve Technology (CVT)

4.2 Experimental Reaction Conditions

The cobalt low temperature Fischer-Tropsch synthesis is typically operated at 200 - 230°C and 10 - 20 bar. In this work, a pressure of 20 bar and temperature of 225°C were used throughout. The weight hourly space velocity (WHSV) of the liquid n-hexadecane feed is based on the hypothetical molar rate of formation of n-hexadecane in the LTFT synthesis. To determine the latter the following assumptions are made; the entire product spectrum of the Fischer-Tropsch synthesis consists of n-hexadecane, and a syngas conversion of 85% is reached. The calculation is presented below in Table 4.2.

Starting from a GHSV of 90 ml (STP)/min.g_{cat} and a H_2/CO ratio of 2 – typical feed gas flow rate and composition found in literature (Visconti et al., 2007) – and given 85% conversion, the molar composition of the effluent is calculated with the following reaction equation:

$$2\ H_2 + CO \rightarrow -CH_2- + H_2O$$

From Table 4.2, three important parameters can be deduced for this experimental programme. The first is the weight hourly space velocity (WHSV) for feeding n-C_{16} to the hydrocracking catalyst on the assumption that F-T produces only n-C_{16}. The WHSV in this work is set at 1 h^{-1},

close to the nominal value of 0.97 hr^{-1} determined in Table 4.2. The second parameter, the water flow rate, or the water WHSV is almost the same as the n-C_{16} WHSV at 0.95 hr^{-1}. The third and final observation is that the H_2/n-C_{16} ratio varies depending on the syngas conversion. At 75% conversion of H_2 and CO the remaining molar flow rate of H_2 is approximately 10 times that of the hypothetical n-C_{16} molar formation rate; at 80% it is down to 8 and at 85% the H_2/n-C_{16} ratio reduces to 5.7. For reason of the aforementioned and other comparative n-C_{16} hydrocracking studies within the Centre of Catalysis research, the H_2/n-C_{16} molar ratio was fixed at 10:1 for this study.

Table 4.2: Calculation of a Hypothetical n-C_{16} Formation Rate from F-T and the Corresponding H_2O Formation Rate and their Volumetric Flow Rate Equivalents

For 85% CO conversion

	Inlet		Outlet	
Component	No of moles	Molar fraction	No of moles	Molar fraction
CO	1	0.333	0.150	0.070
H2	2	0.667	0.300	0.140
H2O	0	0	0.850	0.395
-CH2-	0	0	0.850	0.395
Total	3	1	2.150	1

GHSV	90	$ml/min.g_{cat}$
Molar gas feed rate	0.004	mol/min
-CH_2- molar formation rate	0.0011	$mol(CH_2)/min.g_{cat}$
n-C_{16} molar formation rate	0.0001	$mol(C_{16})/min.g_{cat}$
n-C_{16} mass flow rate	0.0161	$g(C_{16})/min.g_{cat}$
n-C_{16} volumetric flow rate	0.0208	$ml(C_{16})/min.g_{cat}$
n-C_{16} WHSV	0.97	hr^{-1}
Water molar formation rate	0.0011	$mol(H_2O)/min.g_{cat}$
Water mass flow rate	0.0205	$g(H_2O)/min.g_{cat}$
Water volumetric flow rate	0.0205	$ml(H_2O)/min.g_{cat}$
Water WHSV	0.95	hr^{-1}

The table below summarizes the suppliers used to obtain the catalyst and reagents used for this study.

Table 4.3: Catalyst and Reagent Suppliers

Equipment	Supplier
HMFI-90	Süd-Chemie
Pd/SiO_2	Johnson Matthey
Hydrogen (5.0)	Air Liquide
Carbon Monoxide (4.5)	Air Liquide
n-Hexadecane (Reagent Plus 99%)	Sigma Aldrich Chemie (SAFC)

4.3 Catalyst Classification and Loading Procedure

For the first experiment, Experiment A, a 1 wt.% Pd containing catalyst consisting of 5 wt.% Pd/SiO_2 pellets and H-MFI-90 powder (80% zeolite, 20% binder) was used. For the purpose of this thesis the abbreviation $Pd10_AHMFI$ will be used throughout when referring to the catalyst used in Experiment A. Refer to Table 4.4 for catalyst loading masses.

Zeolite powder was pelletized and granulated to obtain a size range 500 – 800 µm and mixed with granulates of the same size of a 5wt.% Pd/SiO2 catalyst which was provided by Johnson Matthey.

For the second experiment, Experiment B, 0.1 wt.% Pd containing catalyst consisting of 5 wt.% Pd/SiO_2 pellets and H-MFI-90 granulates was used. For the purpose of this thesis the abbreviation $Pd01_BHMFI$ will be used throughout when referring to the catalyst used in Experiment B.

For the last experiment, Experiment C, 1 wt.% Pd containing catalyst consisting of 5 wt.% Pd/SiO_2 pellets and H-MFI-90 granulates was used. For the purpose of this thesis the abbreviation $Pd10_CHMFI$ will be used throughout when referring to the catalyst used in Experiment C.

Table 4.4: Catalyst Loading Masses

Experiment	Pd Content (g)	H-MFI-90 (g)	Pellet Size	5 wt.% Pd on Silica (g)
A $Pd10_AHMFI$	(1 wt%) 0.01286	1.2860	powdered HMFI-90	0.2572
B $Pd01_BHMFI$	(0.1 wt.%) 0.001286	1.2860	0,5-0,8 mm granulates	0.02572
C $Pd10_CHMFI$	(1 wt%) 0.01286	1.2860	0,5-0,8 mm granulates	0.2572

The loading of the catalyst occurs from the bottom to the top. The reactor is secured in an upright position in a bench vise. Silane treated glass wool is placed at the bottom of the reactor to provide support. The bottom section of silicon carbide having volume of 30 cm^3 is poured into the reactor using a funnel. The reactor wall is the gently tapped to compact the layer thoroughly. The weight of the catalyst is carefully measured off and poured into reactor again using a funnel. A scale with four decimal places is needed to measure the exact mass of catalyst.

The remaining section of the reactor is then filled with silicon carbide. The reactor wall is then again tapped to compact the final layer of silica carbide. The reactor body is mated to its feed distribution head and secured into the bronze furnace block with the feed lines and outlet connected. Once the unit has been secured a leak test is done by means of pressurizing to 25 bar using nitrogen gas. All fittings are checked using soapy water. Where bubbling is observed, the fitting was further tightened. Upon completion of the leak test, the catalyst pretreatment could commence.

Pretreatment for the purpose of reduction of supported metal catalyst was carried out using a temperature program together with 200 sccm N_2 gas and 50 sccm H_2 gas. The reactor temperature in all four isothermal zones is ramped up from room temperature to 350°C over a ramp period of 4 hours and held at this temperature for 16 hours after which the reactor pressure is set at 20 bar and the temperature is lowered to the reaction temperature, 225°C.

4.4 Operating Procedure

Gaseous feed is mixed and supplied as required via the mass flow controllers (refer to section 4.2). The feed pumps of n-C_{16} and H_2O are primed to release any gas bubbles from the intake line and set to the specified flow rates (refer to section 4.2). The gas flow rate through the needle valve in the sample line leading the GC is verified manually using a bubble flow meter.

At the end of an experiment, care is taken to flush the system of CO by slowly releasing the pressure on the dome-loading side of the back pressure regulator, such that the gas upstream of the mass flow controllers (up to the closed pressure regulators) can be vented through the reactor system, following which the entire system is flushed with N_2 at 250 sccm for several hours.

4.5 Data Analysis using GC-FID and GC-MS

The analysis of products is carried out using an on-line Varian 3800 gas chromatograph with a non-polar Varian capillary column (25 m, 0,15 mm ID, 2 µm film thickness), argon carrier gas and a flame ionization detector. An example chromatogram is shown in Figure 4.3. Good separation is obtained with a temperature program as follows; 5 min at 0°C, ramp to 150°C at 10°C/min, ramp to at 300°C at 5°C/min.

The relatively thick bonded phase (2 µm) allows for the separation of methane, ethane, propylene and propane at 0°C, thereby drastically reducing the consumption of liquid CO_2 for cooling. The trade-off – a slightly higher peak width resulting in sub-optimal, but manageable, peak separation of the mono-methyl isomer of the higher carbon number products – is considered acceptable.

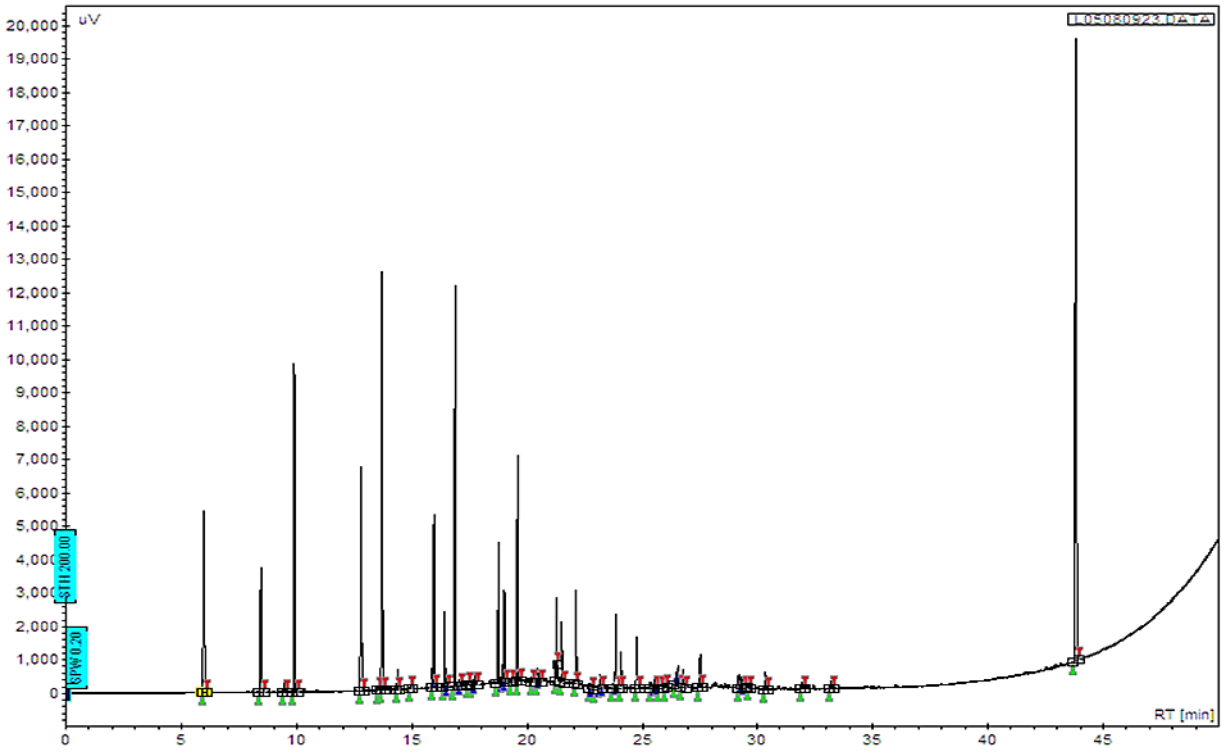

Figure 4.3: Example of a Chromatogram obtained from GC-FID

Gas chromatography equipped with a mass specific detector (GC-MS) was used to identify each of the species in the product with the same column being used in both the GC-FID in the GC-MS instruments such that each peak appears at the same retention time in both instruments. All linear and the branched paraffins in the product stream as well as olefins were identified.

4.6 Calculation of Conversion and Selectivity

The flame ionization detector (FID) is a mass-sensitive detector. Consequently, the peak area in the chromatogram is proportional to the number of reduced carbon atoms in the product sample via a corresponding response factor. The response factor for olefins is only marginally lower than that for paraffins so that no significant error is introduced by setting them equal to 1.

$$A_i \approx N_{Ci}$$

$$N = n \cdot N_A \qquad m = n \cdot M_w$$

The cracking conversion of n-C_{16} is defined as the conversion of n-C_{16} feed into fragments with carbon numbers less than 16.

The total conversion of n-C_{16} is defined as the conversion of n-C_{16} feed into both isomerised C_{16} and fragments with carbon numbers less than 16.

---

where

Integrated area of linear products species with carbon number n

Integrated area of all isomerised products species with carbon number n

After correction, the peak area of a product corresponds to the number of carbon atoms in the product peak. Dividing by the total peak area and assuming that all products were detected yields the number of carbon atoms in product peak *i* as a percentage of the total number of carbon atoms in the entire product spectrum. Selectivities on a carbon basis are obtained, abbreviated S(C_i).

$$S(C_i) = \frac{A_i}{\sum_i A_i}$$

The number of carbon atoms in a chromatographic peak relates to the number of moles of carbon of that product in a sample via Avogadro's number. Therefore, carbon percent and mole percent on C_1 basis are the same.

$$S(n_{c,i}) = \frac{A_i}{\sum_i A_i}$$

To obtain the molar fraction of a particular product in the product spectrum, the following manipulation is required.

$$x_n = \frac{\frac{S(n_{c,i})}{n}}{\sum_i \frac{S(n_{c,i})}{n}} = \frac{\frac{A_i}{n}}{\sum_i \frac{A_i}{n}}$$

with *n* the number of carbon atoms in product *i* as represented in the chemical formula C_nH_m

The calculation of the weight of a product compound as a percentage of the total weight of the product spectrum proceeds similarly.

$$wt.\% = \frac{x_{n,i} \cdot M_{w,i}}{\sum_i x_{n,i} \cdot M_{w,i}}$$

4.7 Experiments Conducted

The three different experiments conducted are represented Tables 4.2, 4.3 and 4.4.

Table 4.5: Experiment A ($Pd10_AHMFI$)

Step No.	Loading of Pd in Mixed Catalyst	Feed C_{16}	Feed H_2	Feed N_2	Feed CO	WHSV	H_2:N_2	H_2:CO	H_2:C_{16}	Temperature	Pressure
	wt%	ml/min	ml/min	ml/min	ml/min	hr^{-1}				°C	bar_g
A.1	1.0	0.03	24.3	12.2	-	1.05	2	-	10	225	20
A.2	1.0	0.03	24.3	12.2	-	1.05	2	-	10	215	20
A.3	1.0	0.03	24.3	12.2	-	1.05	2	-	10	205	20
A.4	1.0	0.03	24.3	12.2	-	1.05	2	-	10	225	20
A.5	1.0	0.03	24.3	-	12.2	1.05	-	2	10	225	20

Table 4.6: Experiment B ($Pd01_BHMFI$)

Step No.	Loading of Pd in Mixed Catalyst	Feed C_{16}	Feed H_2	Feed N_2	Feed CO	Feed H_2O	WHSV	H_2:N_2	H_2:CO	H_2:C_{16}	Temperature	Pressure
	wt%	ml/min	ml/min	ml/min	ml/min	ml/min	hr^{-1}				°C	bar_g
B.1	0.1	0.03	24.3	12.2	-	-	1.05	2	-	10	225	20
B.2	0.1	0.03	24.3	12.2	-	-	1.05	2	-	10	225	20
B.3	0.1	0.03	24.3	-	12.2	-	1.05	-	2	10	225	20
B.4	0.1	0.03	24.3	-	12.2	-	1.05	-	2	10	225	20
B.5	0.1	0.03	24.3	-	12.2	-	1.05	-	2	10	225	20
B.6	0.1	0.03	24.3	-	12.2	0.02	1.05	-	2	10	225	20

Table 4.7: Experiment C ($Pd10_CHMFI$)

Step No.	Loading of Pd in Mixed Catalyst	Feed C_{16}	Feed H_2	Feed N_2	Feed CO	Feed H_2O	WHSV	H_2:N_2	H_2:CO	H_2:C_{16}	Temperature	Pressure
	wt%	ml/min	ml/min	ml/min	ml/min	ml/min	hr^{-1}				°C	bar_g
C.1	1.0	0.03	24.3	12.2	-	-	1.05	2	-	10	225	20
C.2	1.0	0.03	24.3	-	12.2	-	1.05	-	2	10	225	20
C.3	1.0	0.03	24.3	-	12.2	0.02	1.05	-	2	10	225	20
C.4	1.0	0.03	24.3	-	12.2	0.02	1.05	-	2	10	235	20
C.5	1.0	0.03	24.3	-	12.2	0.02	1.05	-	2	10	230	20
C.6	1.0	0.03	24.3	-	12.2	-	1.05	-	2	10	230	20
C.7	1.0	0.03	24.3	-	12.2	-	1.05	-	2	10	235	20
C.8	1.0	0.03	24.3	12.2	-	-	1.05	2	-	10	235	20
C.9	1.0	0.03	24.3	12.2	-	-	1.05	2	-	10	225	20

4.8 Test Unit Commissioning

Obtaining a stable output from the test unit was met with considerable difficulty, the complete version of which is explained in the Appendix. The following is a brief overview of how vaporization of the reactor effluent and co-feeding of water is achieved.

In order to evaporate n-C_{16} in a controlled manner leading to minimal scatter in the data, the following conditions need to be satisfied. The partial pressure of C_{16} must increase incrementally along the length of the vaporiser. Any step change in the partial pressure may result in scatter. Step changes are either a drastic increase in temperature and C_{16} vapor pressure in conjunction or a drastic lowering of the partial pressure due to dilution of the C_{16} containing effluent. When a step change is introduced, the effect can be moderated by increasing the surface area on which C_{16} is evaporated.

Water and n-C_{16} are immiscible at the conditions prevailing in the reactor. Water has a large effect on the stability of the C_{16} output. When water and C_{16} are both introduced in the liquid state to the reactor, large scatter of the C_{16} output is the result. This problem is resolved only when one of these components is fed to the reactor as a vapor. And since C_{16} needs to be evaporated preferably in a controlled way, water must be pre-heated and introduced as a vapor. Because the top of the reactor must remain cool so as not to aggravate the already steep temperature gradient in the SiC filler on which C_{16} is evaporated, water is introduced through a dip tube that drops down to the point at which all water is in the vapor phase. Water runs through the dip tube and is evaporated on the progressively hot wall of the tube that extends about 15 cm into the reactor but ends well above the catalyst bed (approximately 20 cm).

Figure 4.4 displays the excellent steady state blank run results. The standard deviation of the C_{16} peak height was 1.4% before introduction of water and 1.7% when water was flowing through the reactor (from sample number 930 in Figure 4.4).

A J-type thermocouple with a length of 80 cm was used to determine the temperature profile from the bottom of the reactor down to the bottom of the vaporizer. Figure 4.5 presents the temperature profile of the vaporizer section. The temperature is measured at 1 cm increments. The thermocouple is slid through a 1/8” tube that was installed without any sharp bends. It is seen on the initial temperature profile that there is a hot spot in the exit line from the reactor. This was corrected by evenly spreading the coiled heating wire surrounding that section of the line. The temperature profile after this adjustment shows a very stable temperature profile with no hot spots remaining.

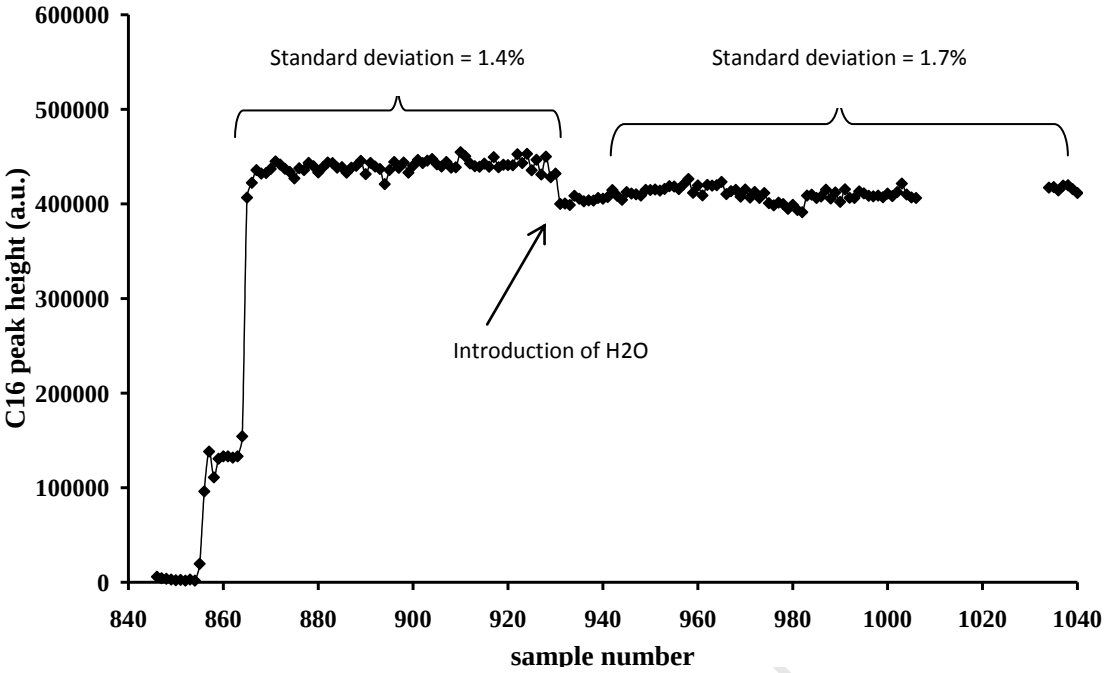

Figure 4.4: C_{16} Peak Height for Blank Run with Water Inlet Modification

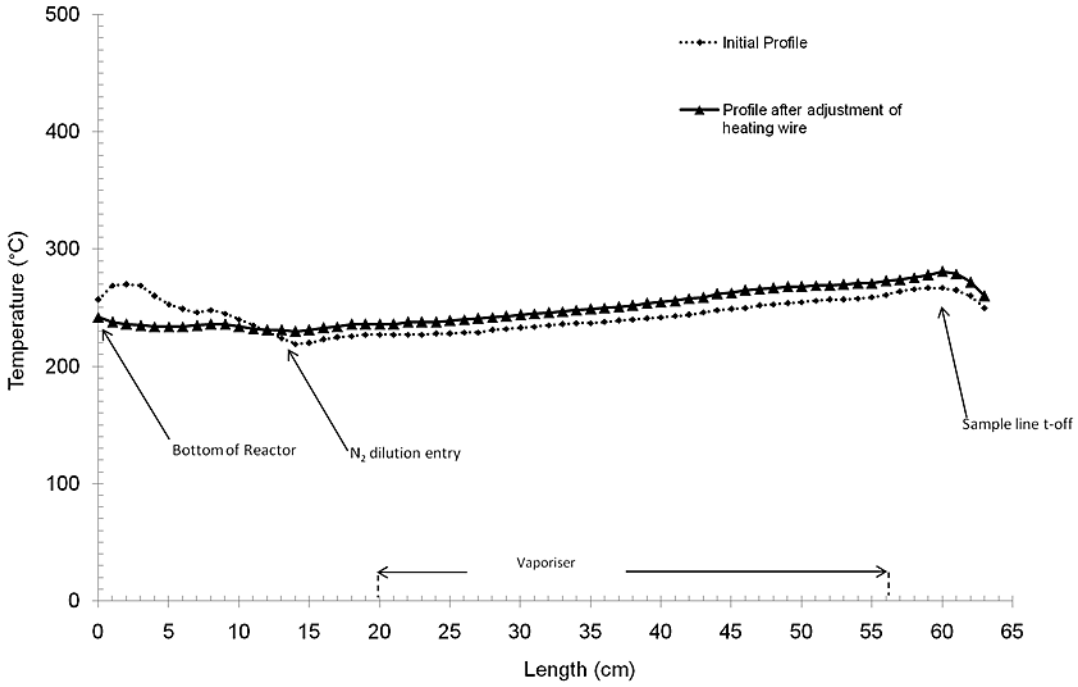

Figure 4.5: Temperature Profile of the Vaporizer Section

Results 5

5.1 Effect of Temperature on n-C_{16} Hydrocracking

The Fischer-Tropsch process involving a low temperature cobalt-based catalyst is usually run between 200°C and 230°C. A hydrocracking catalyst used in combination with an F-T catalyst would have to be active in this temperature window. The first experiment (Experiment A), the results of which are presented here, records the conversion and product selectivities in the hydrocracking of n-hexadecane over a combined (mixed) catalyst bed comprising of $Pd10_AHMFI$ with a metal/acid ratio of 1.02 at WHSV = 1, with a H_2/n-C_{16} ratio of 10 at 20 bar gauge. An overview of the conversion versus time-on-stream (TOS) is presented in Figure 5.1.

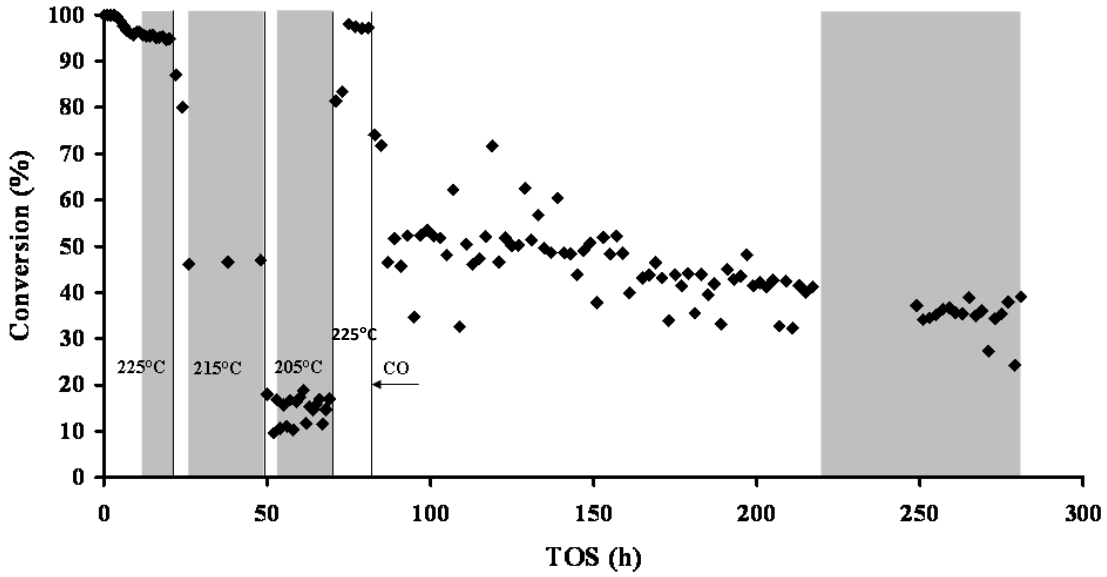

Figure 5.1: TOS Data for n-C_{16} Conversion over Pd/SiO_2 + HMFI-90
(Experiment A: $Pd10_AHMFI$)

A solid vertical line in Figure 5.1 indicates a change of an experimental setting. The grey zones indicate which data points were used to calculate conversions and selectivities considered representative of the conditions prevailing and which are subsequently used for comparison. Steady state is reached after approximately 12 hours. After initial performance evaluation reaction temperature is increased to 225°C where upon CO is introduced into the gas feed stream at a ratio of H_2/CO = 2, similar to F-T reaction conditions. As may be seen in Figure 5.1, the catalyst deactivates rapidly at first in a CO containing gas phase and continues to deactivate

slowly thereafter until it appears to level off at which point the pseudo steady-state conversion can be determined. It should be noted that Experiment A was conducted early in the experimental series, before modifications to the test unit were implemented to improve experimental data scatter (the reader is referred to the Appendix for a detailed account of the improvements undertaken). Subsequent experiments were conducted after the aforementioned improvements and, consequently, show less data scatter.

Conversion versus temperature data, in the absence of CO, is plotted in Figure 5.2. The conversion increases sharply from 14.7% at 205°C, through 46.6% at 215°C to 95.2% at 225°C, evidence of a high reaction activation energy.

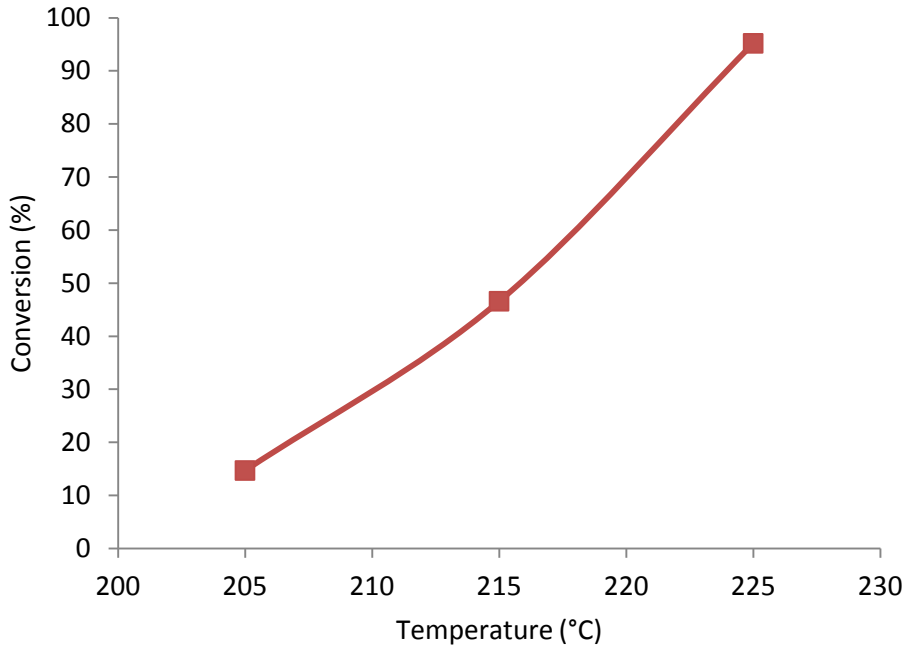

Figure 5.2: Conversion versus Temperature of n-C_{16} Hydrocracking
(Experiment A: $Pd10_AHMFI$)

Figure 5.3 (a), (b), (c) present the product carbon number distributions at the different temperatures evaluated in Experiment A. Differences between the product distributions seem small. At the highest temperature, and conversion, the distribution is slightly more weighted towards the shorter normal and iso-paraffins. This is clear from Figure 5.4 which displays the total of normal and isomerised paraffins per carbon number.

The product distributions of Figure 5.3 are to be interpreted as follows. From Figure 5.3 (a) take the C_7 fraction as an example. Within the C_7 fraction the branched paraffin, iso-C_7, amounts to 8% of the total carbon atoms in the product distribution and the branched olefin, iso-$C^{=}_7$, amount to 1%. Together, all branched products, paraffins and olefins, make up 9% of the C_7 fraction.

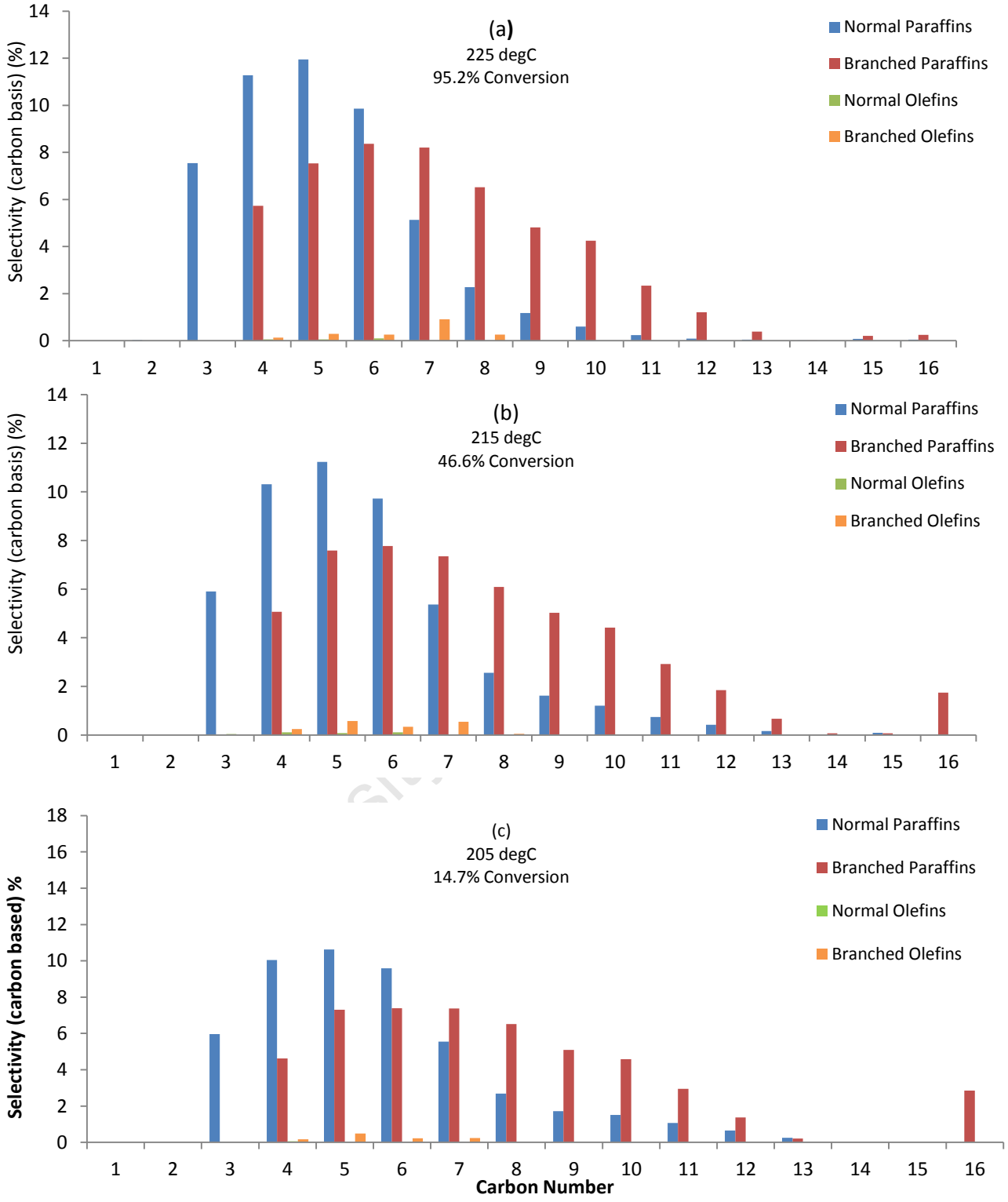

Figure 5.3 (a), (b) and (c): Selectivity versus Carbon Number at 225°C, 215°C and 205°C (Experiment A: $Pd10_AHMFI$)

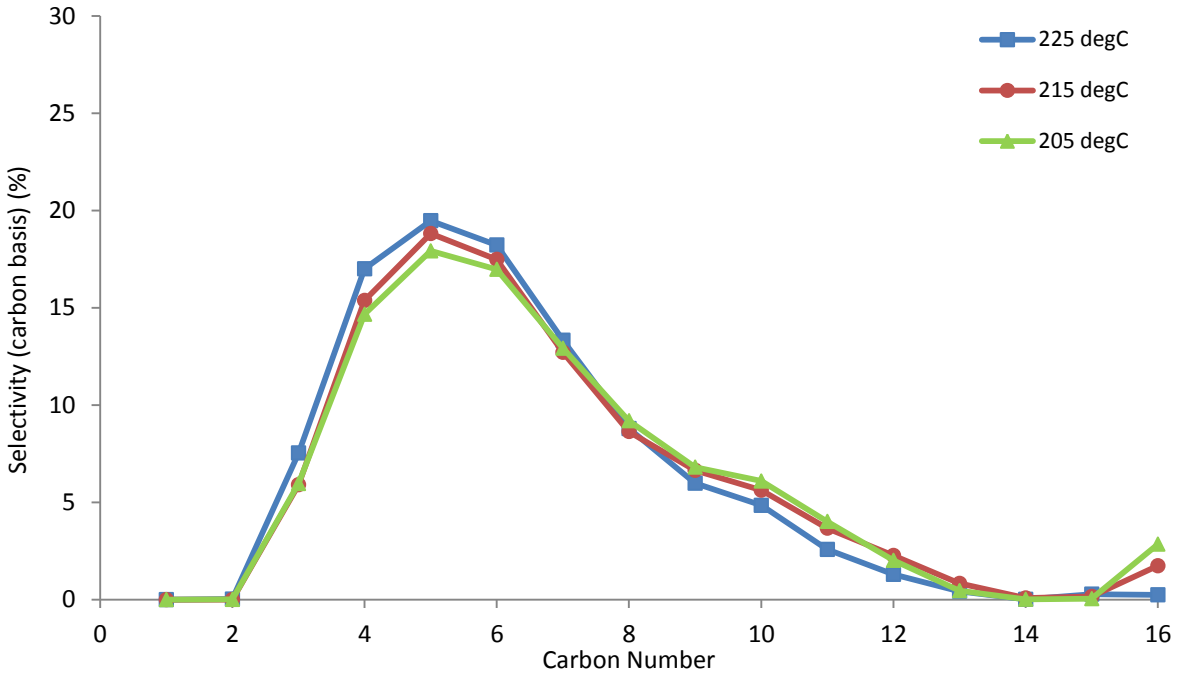

Figure 5.4: Total Product Distribution versus Carbon Number
(Experiment A: $Pd10_AHMFI$)

Figures 5.5 (a) and (b) compare the product distribution of n-C_{16} hydrocracking, at similar temperature, in the absence and presence of CO (Experiments A.1 and A.5, respectively). The total product distribution does not change significantly, however, slightly lighter product is observed in the absence of CO. This is, perhaps, easier seen in Figure 5.6. On the other hand, marked differences in the nature of products in the individual carbon number fractions can be observed. From C_4 to C_7, the ratio of branched to normal products is increased in the presence of CO.

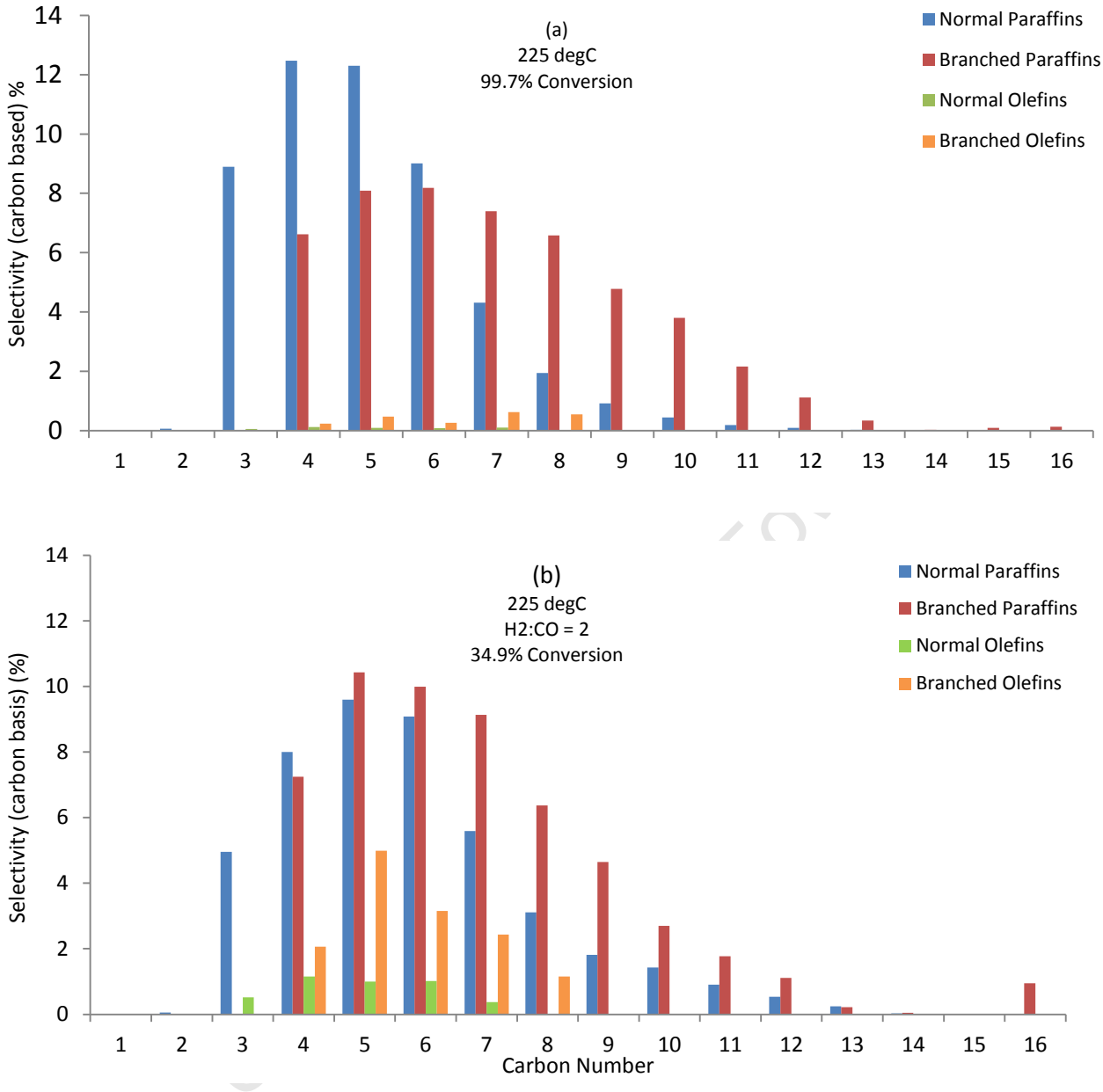

Figure 5.5 (a) and (b): Selectivity versus Carbon Number in the Absence and Presence of CO at 225°C (Experiment A: $Pd10_AHMFI$)

The product spectrum of n-C_{16} hydrocracking in the presence of CO is significantly more unsaturated than in the absence of CO, for example in the C_5 fraction 18% of the branched products are olefins in the presence of CO versus the 3% branched olefinicity in the absence of CO.

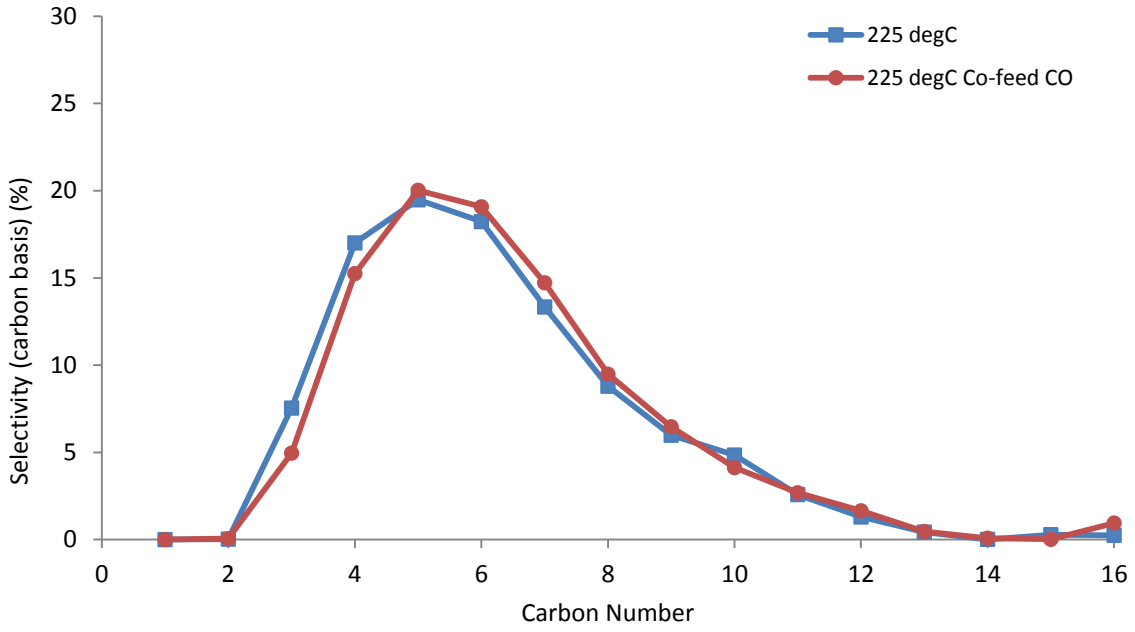

Figure 5.6: Effect of co-feeding CO to the hydrocracking reaction
(Experiment A: $Pd10_AHMFI$)

5.2 Effects of Co-Feeding Water and CO on n-C_{16} Hydrocracking

In order to be able to co-feed water to the hydrocracking experiment the rig design was improved. This is explained in the Appendix. Two experiments (Experiments B and C) were run with different loadings of the noble metal catalyst in combination with an equal amount of acid catalyst. The weight hourly space velocity is regarded as constant with respect to the number of acid sites in the bi-functional catalysts. In the reactor, the partial pressure of C_{16} is much higher than the vapor pressure of C_{16} and thus the reactor operates in a trickle phase regime, and the catalyst is presumed to be well wetted under the conditions of this work.

5.2.1 $Pd01_BHMFI$

Figure 5.7 presents n-C_{16} conversion as a function of time-on-stream for the 0.1 wt.% Pd containing catalyst system ($Pd01_BHMFI$) and shows the influence of CO and water on catalyst performance (Experiment B). Dark grey zones demarcate those samples from which the condition representative average conversion and standard deviation were determined. Three such zones are shown in Figure 5.7; respectively for the standard hydrocracking condition, the catalyst under CO co-feeding and, lastly, for the catalyst under combined CO and H_2O co-feeding. At each condition, catalytic performance stabilizes at a different conversion level reflecting steady state operation.

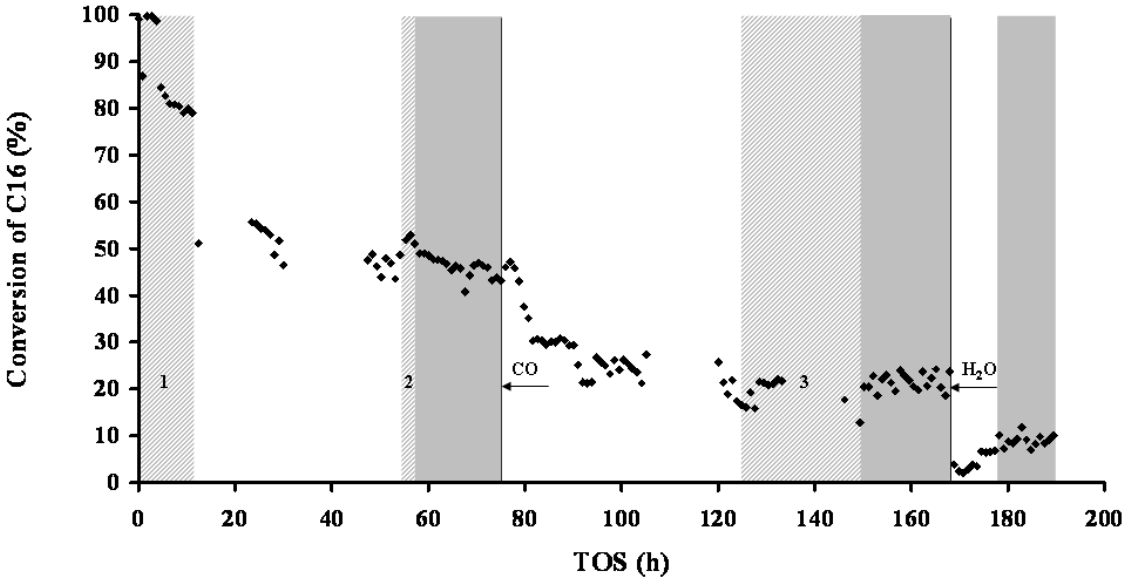

Figure 5.7: Conversion versus TOS of n-C_{16} Hydrocracking
(Experiment B: $Pd01_BHMFI$)

Table 5.1 summarizes the steady state mean conversion and standard deviation at the various experimental conditions.

Table 5.1: Conversion at Different Experimental Settings

Reaction Temperature 225°C	Total Conversion (%)	Standard deviation (σ) (%)
Unsteady State (Experiment B.1)	~100	8.80
Steady State (Experiment B.2)	46.0	2.16
Co-feed CO (Experiment B.3)	21.5	1.77
Co-feed CO and Water (Experiment B.6)	9.1	1.28

The steady state conversion over the $Pd01_BHMFI$ catalyst is 46.0%. Co-feeding of CO at a partial pressure typical of F-T synthesis conditions lowers the activity to 21.5%. H_2O, the main by-product of F-T synthesis, when administered at a partial pressure typical of F-T operations, reduces the activity further to less than 10%. Figure 5.8 presents an overview of the total product distribution under the various conditions of Figure 5.7.

From Figure 5.8 it can be seen that upon introducing CO into the hydrocracking experiment, the C_3-C_7 products are increased whereas the C_9-C_{13} products are reduced. The same trend is observed, and to a still higher degree, when H_2O is introduced into the feed. With H_2O and CO, no iso-C_{16} is observed.

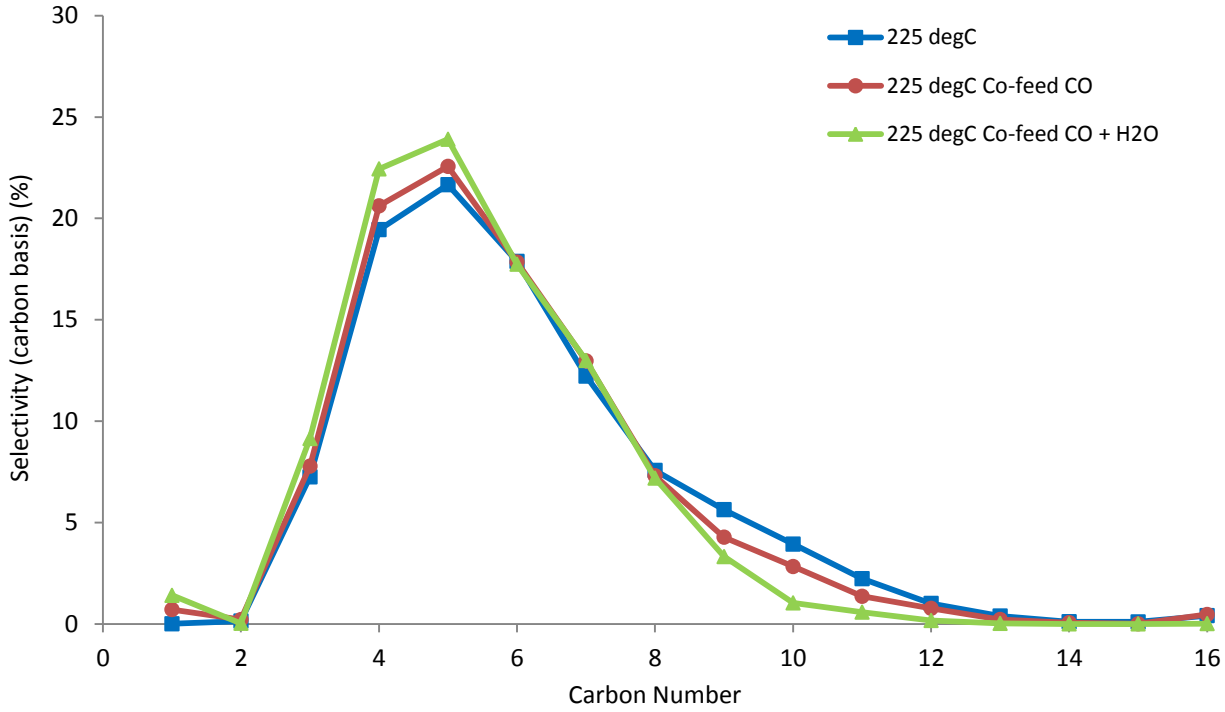

Figure 5.8: Effects of Co-Feeding H_2O, CO on Hydrocracking Reaction
(Experiment B: $Pd01_BHMFI$)

Figures 5.9 (a), (b) and (c) present, respectively, the selectivity, per carbon number, for normal hydrocracking reaction conditions, the co-feeding of CO, and the co-feeding of CO together with H_2O. The following observations can be made. Firstly, in the case of 'standard' hydrocracking conditions, methane is not observed. Ethane is found in the product spectrum but, at 0.1%, it can be neglected. When N_2 is replaced by CO, the conversion decreases from 46.0% to 21.5%. The normal paraffin selectivities are slightly depressed with CO as compared to without CO in the gas feed stream, whereas the iso-C_4, iso-C_5 and iso-C_7 selectivities are higher at the expense of the iso-C_8 to iso-C_{12} selectivities. Interestingly, when CO is co-fed with H_2, a small amount of methane (0.7%) is produced.

Upon introduction of H_2O to the feed, the trends that were seen with CO persist and become even more pronounced. The normal paraffins are further decreased and the methane selectivity is doubled. At only 9.0% conversion, a rather narrow product distribution is obtained.

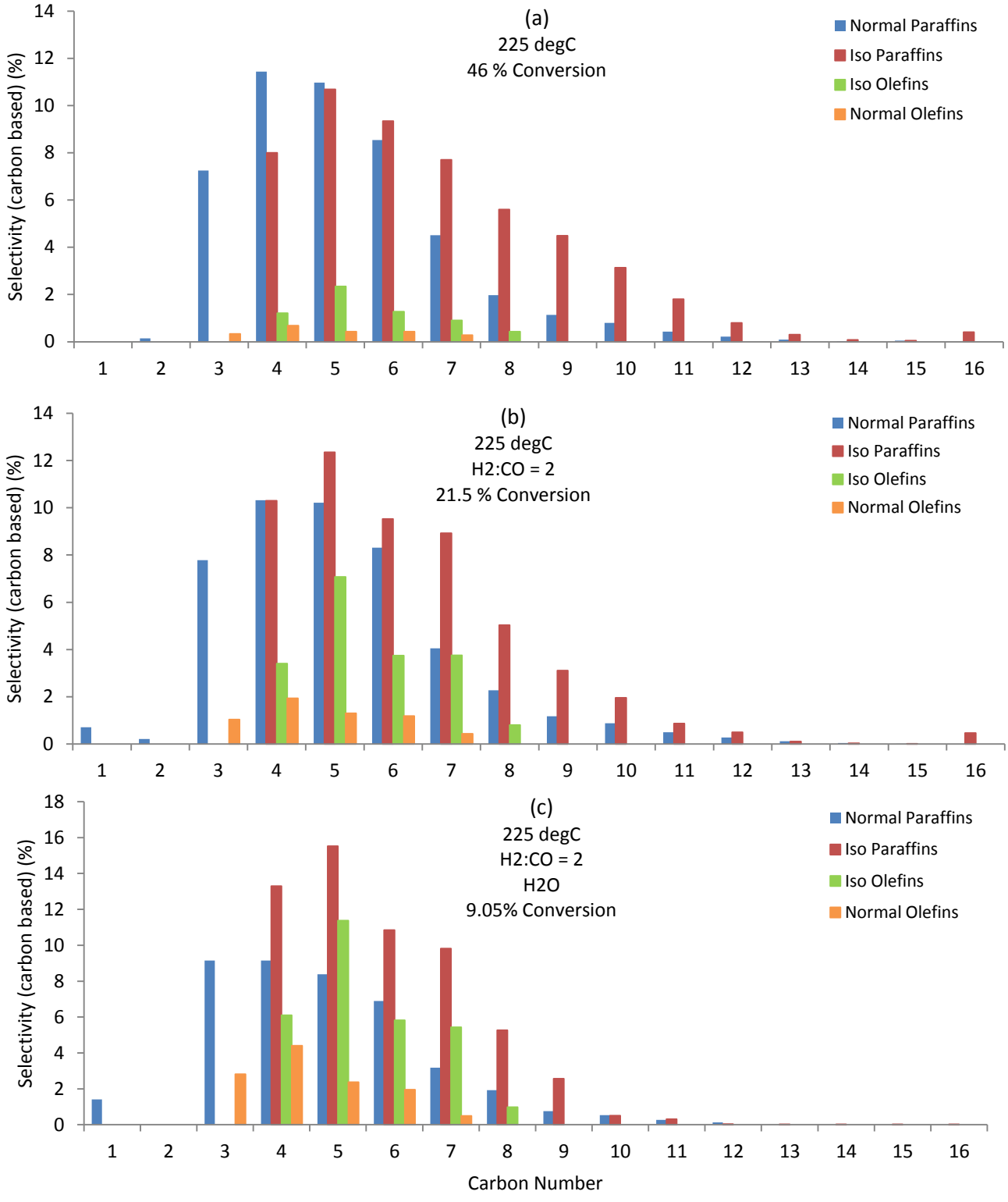

Figures 5.9 (a), (b) and (c): Effects of co-feeding H_2O, CO on hydrocracking (Experiment B: $Pd01_BHMFI$)

5.2.2 Pd10$_C$HMFI

Experiment C was conducted with a 1wt% Pd catalyst (Pd10CHMFI) but, otherwise, represents a similar investigation to Experiment B but for additional temperature conditions. Conversion is plotted as a function of time-on-stream and conditions in Figure 5.10 where dark grey zones demarcate the samples from which the condition specific average conversion and standard deviation were determined. Nine such zones are shown in the Figure 5.10 for various experimental conditions of standard hydrocracking in the presence of CO and hydrocracking in the presence of CO and H_2O, respectively at various temperatures in the range 225°C - 235°C. In all cases stable conversion indicates that steady state performance is reached.

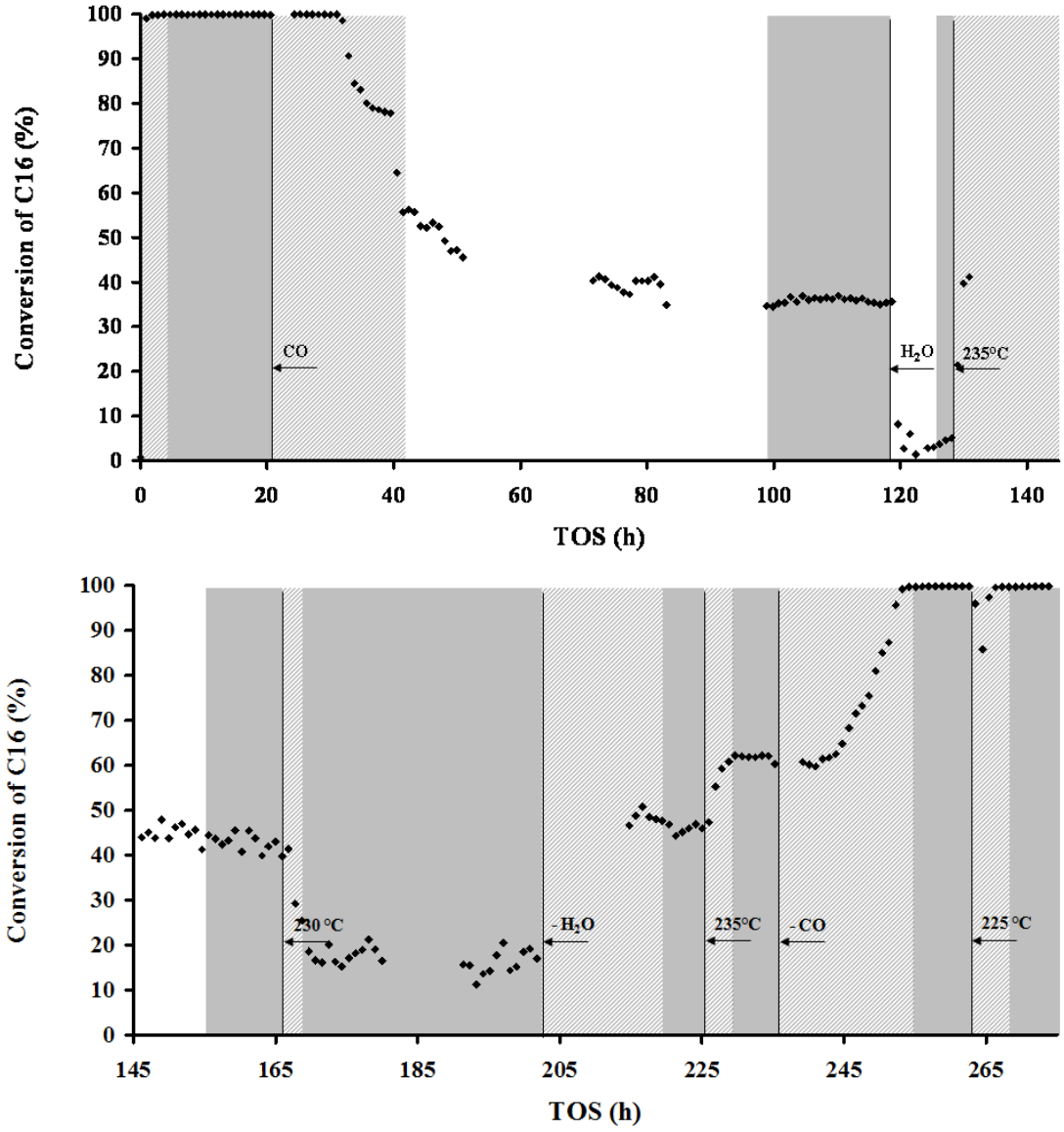

Figure 5.10: Conversion of n-C_{16} versus Time-On-Stream
(Experiment C: Pd10$_C$HMFI)

At 235°C under H_2O and CO poisoning, a conversion of 42.6% is obtained on this $Pd10_CMFI$ catalyst. In comparison, the $Pd01_BHMFI$ catalyst displayed a similar activity before poisoning at 225°C. Table 5.2 summarizes the steady state mean conversion and standard deviation at the various experimental conditions.

Table 5.2: Conversion at Different Experimental Conditions ($Pd10_CHMFI$)

	Experiment No.	Temperature	Total Conversion
		°C	%
Normal hydrocracking reaction	C.1	225	~100
Co-feed CO	C.2	225	36.02
Co-feed CO and H_2O	C.3	225	4.46
Reaction temperature increased	C.4	235	42.64
Reaction temperature decreased	C.5	230	16.95
Remove H_2O	C.6	230	45.9
Reaction temperature increased	C.7	235	61.69
CO removed (replace with N_2)	C.8	235	~100
Reaction temperature decreased	C.9	225	~100

From Figure 5.11, which presents an overview of the total product distribution, it can be seen that upon introducing CO into the hydrocracking experiment, the C_3-C_6 products are decreased whereas the C_7-C_{13} products are up slightly. The opposite trend is observed when H_2O is introduced into the feed.

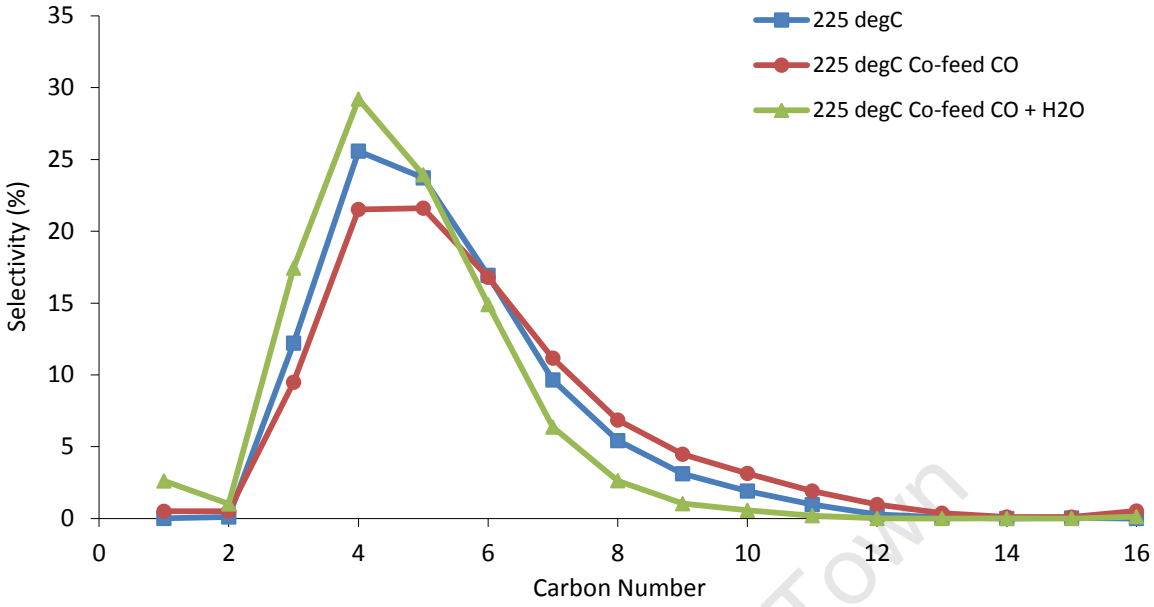

Figure 5.11: Effects of co-feeding H_2O, CO on Hydrocracking
(Experiment C: $Pd10_CHMFI$)

Figures 5.12 (a), (b) and (c) display the selectivity (n-, iso-, olefin, paraffin) per carbon number of products for normal hydrocracking reaction conditions, co-feeding of CO and co-feeding of CO/H_2O, respectively. In general, the product of the 1wt.% Pd catalyst is more saturated than that of the 0.1 wt.% Pd catalyst (Figure 5.12 vs. Figure 5.9) but otherwise the general trends are the same. Methane and Ethane are only formed in the presence of CO and/or H_2O, and olefinicity increases in the presence of CO and more so in the presence of CO/H_2O.

It should also be noted that the impact of CO and CO/H2O addition on catalyst activity (n-C_{16} conversion) appears to be significantly greater in the case of the catalyst with the higher metal loading.

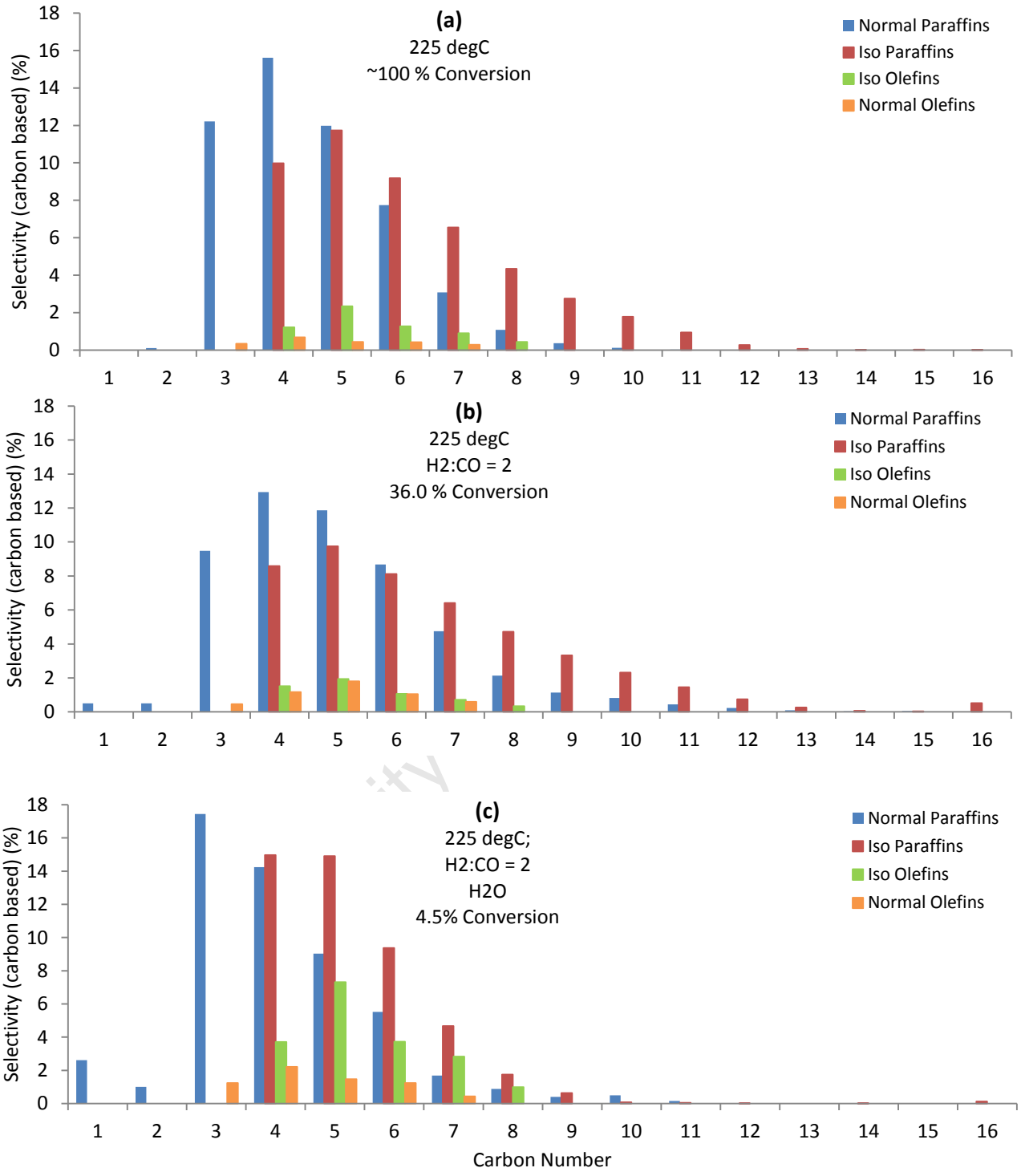

Figures 5.12 (a), (b) and (c): Effects of co-feeding H_2O, CO on n-C_{16} hydrocracking (Experiment C: Pd10$_C$HMFI)

5.2.3 Influence of Temperature

Figure 5.13 presents the n-C16 conversion as a function of temperature for standard hydrocracking as well as hydrocracking in the presence of CO and CO+H_2O for both the $Pd01_BHMFI$ and $Pd10_CHMFI$ catalysts.

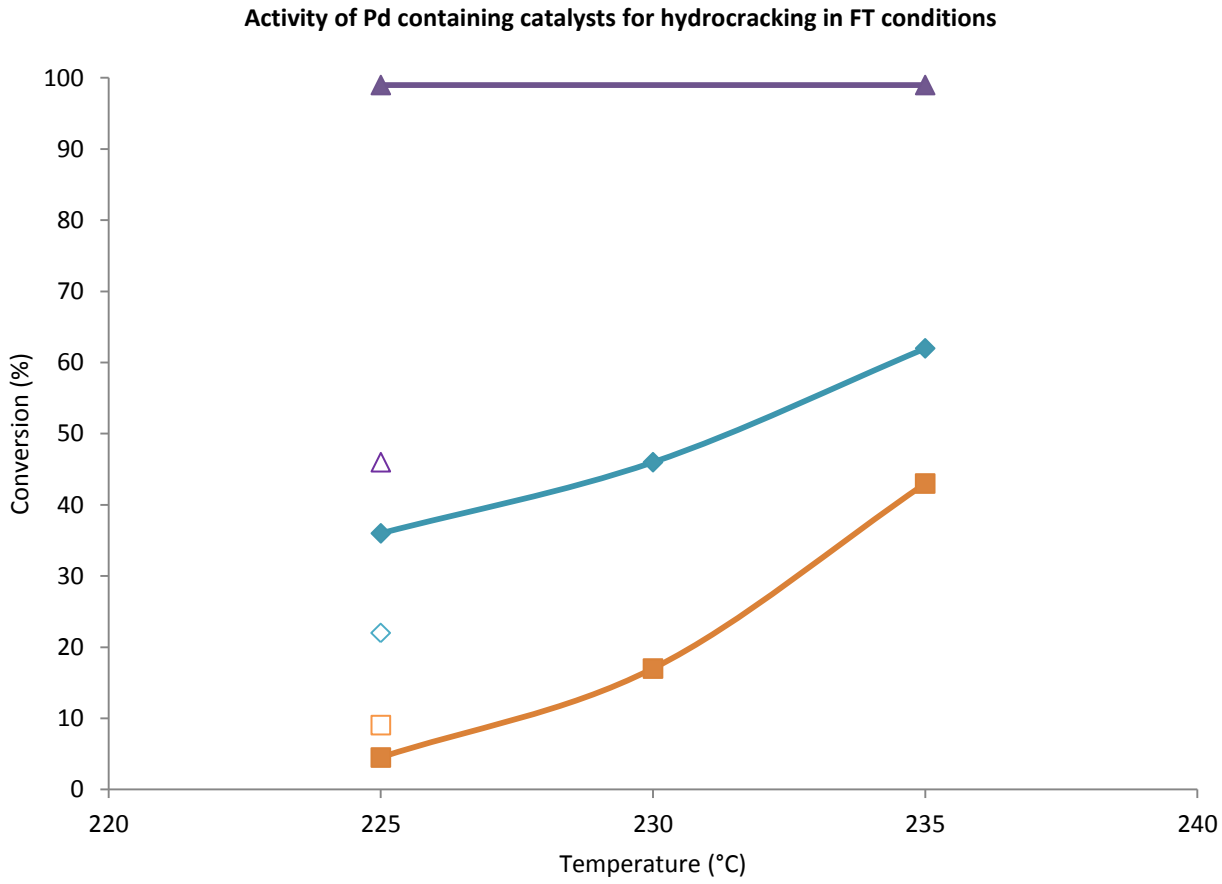

Figure 5.13: Effects of co-feeding CO and H_2O on (a) $Pd01_BHMFI$ (open symbols) and (b) $Pd10_CHMFI$ (closed symbols) in normal hydrocracking (triangles), with CO co-feeding (diamonds) and with CO together with H_2O co-feeding (squares).

Both CO and H_2O deactivate the catalyst, but since the deactivation by CO and H_2O was not measured independently it is not clear which exhibits the greater inhibition. Nonetheless, H_2O introduction to a catalyst that is already suppressed by CO, results in a further loss in catalyst activity. In both cases, CO and CO/H_2O presence, an increase in temperature partially reverses the induced suppression in catalyst activity. Figures 5.7 and 5.10 clearly demonstrates CO and CO/H_2O poisoning to be completely reversible within the temperature range of these experiments, i.e. 225°C – 235°C

5.2.4 Effects of CO and H_2O on Product Selectivities at Equal Conversions

Comparison of the product distributions obtained over Pd catalysts ($Pd01_BHMFI$ and $Pd10_CHMFI$) for normal hydrocracking, CO co-feeding and CO + H_2O co-feeding at almost equal conversions have been investigated. The total product distribution – the sum of branched and linear products and including unsaturated compounds – is very similar for the three cases under consideration as displayed in Figure 5.14.

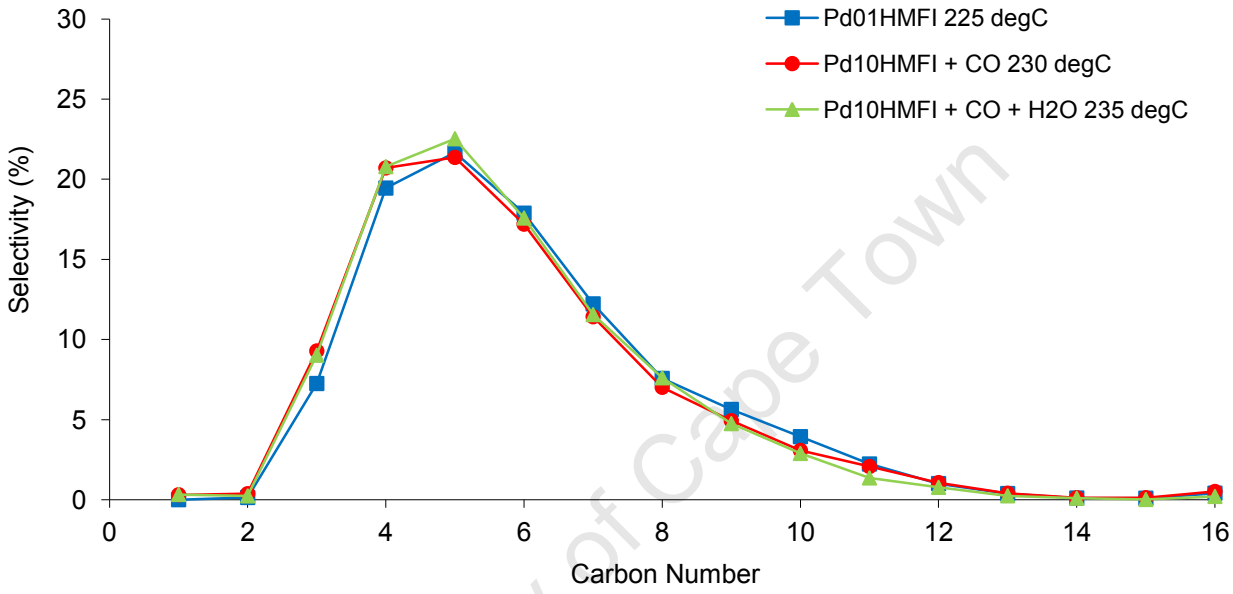

Figure 5.14: Selectivity per Carbon Number Fraction versus Carbon Number for Experiments B.2 (46.0% Conversion), C.6 (45.9% Conversion) and C.4 (42.6% Conversion)

The question of whether or not it is appropriate to compare these results will be dealt with in the next chapter. Apart from small differences in the iso-/n- selectivity ratios and even smaller differences between the total product distributions, one phenomenon needs to be underlined; with co-feeding of CO and H_2O a dramatic increase of the degree of non-saturation is observed. When CO is introduced in the reaction feed, the linear olefin content already increases, but with H_2O the total olefin content increases to 23% of the entire product spectrum.

Discussion 6

6.1 n-C_{16} Hydrocracking - Correlation with Temperature

The acid : metal site ratio plays a key role in the product selectivities observed in hydrocracking. The more rapid formation of unsaturated cracking products over a zeolite presenting a more active acid function would result in an insufficient metal function being present to rehydrogenate (per the classical mechanism) or provide sufficient activated hydrogen to saturate the olefinic cracking fragments. This eventuality would allow these unsaturated species to undergo consecutive cracking reactions, thereby shifting the product carbon number distribution towards lighter species. Should the zeolite acid function be less active, however, the excess metal function would serve to rapidly rehydrogenate or provide activated hydrogen to saturate the olefinic cracking products, effectively quenching the cracking reaction. This would result in a shift towards heavier species in the product carbon number distribution for that catalyst (Kukard, 2008). From a certain level of metal activity and above, the cracking product yield does not increase further. Because of the high feed isomer (iso-C_{16}) yields obtained in the iso-dewaxing process using hydrocracking catalysts with a high metal activity, the term ideal hydrocracking has been introduced. Under ideal hydrocracking conditions, an apparently unique relationship between product yields and total conversion is obtained (Thybaut et al., 2005). This relationship can be observed in Figure 6.1.

Thybaut et al. (2005) conclude that apart from the catalyst's acid-metal balance, the operating conditions also strongly affect the ideality of the hydrocracking behavior. Increasing total pressures, decreasing temperatures, and decreasing molar hydrogen-to-hydrocarbon ratios were found to favor ideal hydrocracking, whereas non-ideal hydrocracking is favored for higher feed carbon numbers under identical hydrocracking conditions.

In this work the total pressure was kept constant at 20 bar, typical of cobalt based F-T processes. From Figure 5.3, two important observations are immediately apparent, namely that 1) the iso-C_{16} selectivity is very low, almost non-existent but varies from 2.9% at 205°C to 0.3% at 225°C and that 2) the product distribution of secondary cracking products varies very little with temperature. Figure 6.2 presents the observed relationship between the cracking and isomerisation yield and the total conversion for the hydrocracking catalyst used in Experiment A. At the lowest temperature slightly less cracking is observed. These small

differences or trends should not distract from the overriding conclusion that hydrocracking of n-C_{16} over this catalyst is far removed from ideal. The low iso-C_{16} yield demonstrates that the balance between the strength of the metal and the acid sites is shifted in favor of the acid sites. It has already been reported in literature that a Pt containing ZSM-5 acid zeolite catalyst displays a low selectivity towards branched C_{16} products in comparison to other zeolite framework types (Park et al., 2000). The question that needs to be answered is why a hydrocracking catalyst with a strong noble metal such as Pd gives rise to non-ideal hydrocracking behavior. Chavarria et al. (2004) demonstrated that a weak metal function such as Mo, dispersed on H-Beta, enhances non-ideal behavior in n-hexadecane hydroisomerisation and hydrocracking reactions. It stands to reason then that the ZSM-5 acid zeolite catalyst is a very strong acid catalyst.

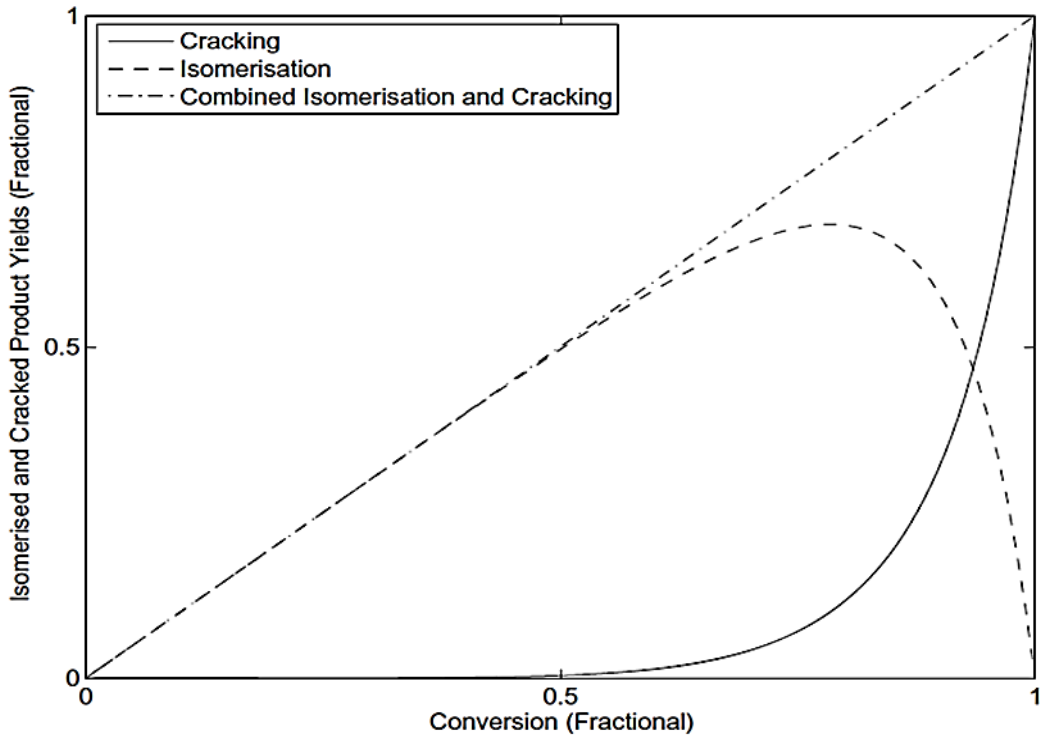

Figure 6.1: Yield of Isomerisation and Cracking Products for the Bi-functional (Metal/Acid) Hydrocracking of a Long n-Alkane (Taken from Kukard, 2008)

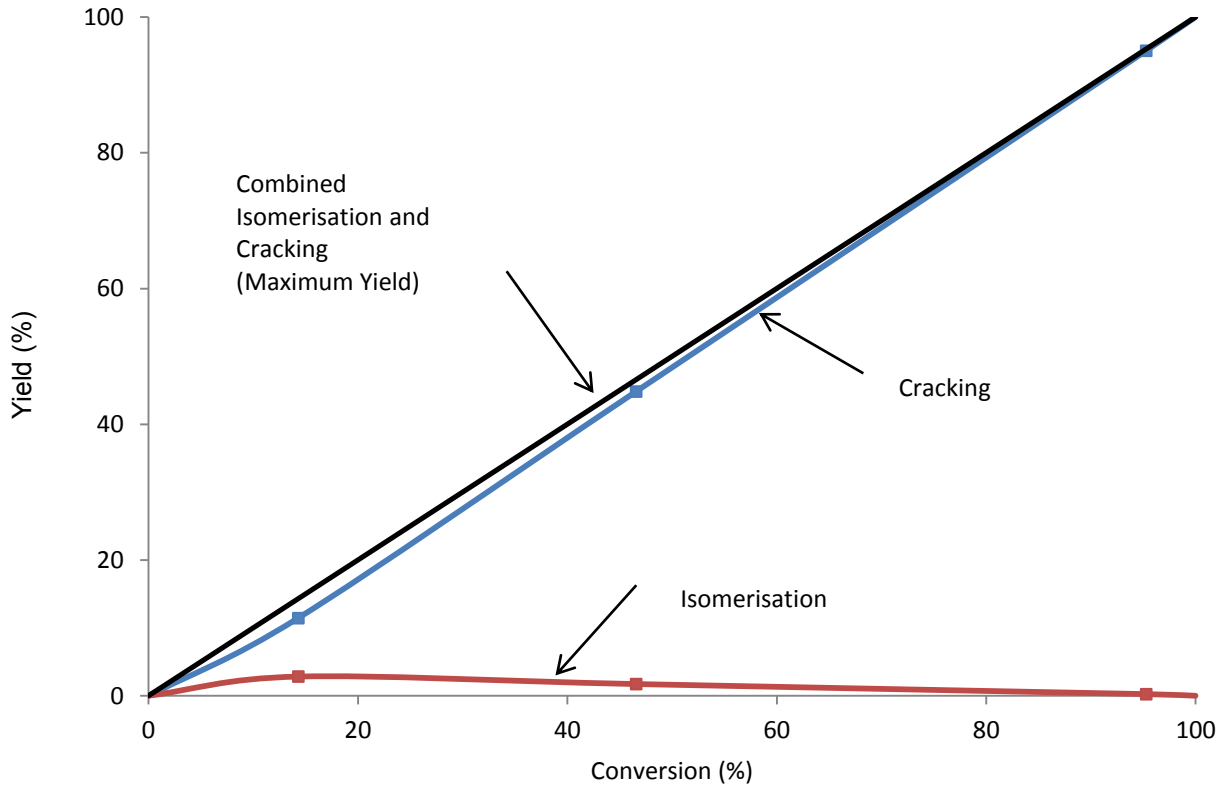

Figure 6.2: Observed Isomerisation and Cracking Yield over Hydrocracking catalyst under Low Temperature Conditions (Experiment A: $Pd10_AHMFI$)

Carbenium ions generated from alkenes on a protonating acid site in the zeolite framework undergo skeletal rearrangement followed by cracking via β-scission to produce one carbenium ion and one alkene. The evidence suggests that the alkene is far more likely to be protonated by the acid site than hydrogenated on the metal site. This is further confirmed by the lack of alkenes in the final product spectrum.

The influence of temperature on the activity is substantial. The conversion rises rapidly between 205 and 225°C, but the product selectivities remain similar. This indicates the effect of temperature on the isomerisation and cracking rates to be similar. From this, one can conclude that the activation energies for the acid-catalyzed steps are similar.

The absence of C_{14} and C_{15} in the product spectrum, which cannot be formed by β-scission of a branched carbenium ion shows that hydrogenolysis is not a favorable reaction pathway on this catalyst. Terminal C–C bonds are not broken by this bi-functional catalyst, since no methane nor C_{15} is formed. Internal C–C bonds are broken at a very low rate by hydrogenolysis; C_2 and C_{14} are found in trace amounts.

6.2 n-C_{16} Hydrocracking - Effect of CO Co-Feeding

Upon introduction of carbon monoxide into the feed stream, the hydrogen-to-hydrocarbon ratio remains unaltered since CO simply replaces the inert N_2 that was already present in the feed.

CO poisons the catalyst such that the activity is reduced. On the $Pd10_AHMFI$ catalyst, the conversion decreases from ~100% to 35% (see Figures 5.5 (a) and (b)), whereas on the $Pd01_BHMFI$ catalyst it is decreased from 46% (steady state) to 22% (Figure 5.9 (a) and (b)).

It is clear that in the absence of CO, the overall reaction rate increases with higher metal loadings. It is therefore fair to say that at least in part, the metal catalyzed reaction step is rate-controlling. Hypothetically, if, with even higher metal loadings, the activity would no longer increase with increasing metal loading, that is, if the activity becomes independent of metal loading, it can be said that the metal catalyzed reaction rate no longer controls the overall reaction rate. Unfortunately, with only two metal loadings, such a 'leveling-off' of the correlation of conversion versus metal loading cannot be observed.

Ideal hydrocracking occurs when the acid catalyzed step is rate controlling, when the metal dehydrogenating function is sufficiently active to quickly hydrogenate intermediates before these can undergo successive reactions. In this work, ample evidence of excessive secondary cracking is presented, underlining that the metal catalyzed reaction step controls the rate.

In the presence of CO poisoning, activity is severely reduced both on the low as on the high metal loaded catalyst. Here too, activity increases with metal loading albeit to a lesser extent. Therefore it can be said that the metal catalyzed step controls the overall reaction rate.

With increasing temperature, the activity in the presence of CO also increases (Experimental step C7, see Figure 5.10). Somewhat surprisingly, the activity is not entirely quenched under the high partial pressure of CO. From Figure 5.10 it is seen that upon the removal of CO the total conversion increases from 62% to complete conversion of 100%.

In order to compare selectivities in the presence and absence of CO, the standard reaction in the absence of CO needs to be performed at a higher space velocity, consequently at lower conversion. With both reactions at lower conversions, the selectivities, in the absence and presence of CO, can then be compared to determine whether the CO poisoning is reversible.

The effect of co-feeding CO on the product selectivities is presented in the product distribution figures of the previous chapter. The first important observation that can be made is that no significant amount of methane is formed from a feed of CO and H_2. Theoretically, two pathways exist for the appearance of methane in the product stream. The first and most

obvious is direct synthesis (CO_x methanation) on a noble metal site. But methane can also be formed by hydrogenolysis of alkanes or alkenes on a noble metal catalyst. Since no evidence of hydrogenolysis was found in the absence of CO it seems unlikely that the presence of CO would promote this reaction pathway. In light of what follows this will appear even more unlikely.

Further to the differences between product selectivities with and without CO, it is clear that in the presence of CO a more unsaturated and more branched product distribution is obtained. This may be seen from Figures 5.3, 5.9 and 5.12 for the $Pd10_AHMFI$, $Pd01_BHMFI$ and $Pd10_CHMFI$ catalysts, respectively. The increase of unsaturated products (normal and branched olefins) can be explained by the poisoning effect of CO on the metal function. A more branched product is also expected with lowered reaction rates on the metal sites as compared to reaction rates on the acid sites. Therefore it seems that the effects on the activity and selectivity observed with co-feeding CO can be explained by an inhibition of the metal function to rehydrogenate the unsaturated product species.

6.3 n-C_{16} Hydrocracking - Effect of H_2O Co-Feeding

The effect of co-feeding H_2O on the activity of both the low ($Pd01_BHMFI$) and the high ($Pd10_CHMFI$) loading bi-functional catalysts is displayed in Figure 5.13. As can be seen from the experimental overview presented in the results chapter, the effect of H_2O was not tested independently of the effect of CO co-feeding. When water is introduced to the reaction mixture the partial pressures of all other constituents are lowered. This is shown in Table 6.1.

Table 6.1: Partial Pressures during the n-C_{16} Hydrocracking Experiments:
1) Normal Hydrocracking Conditions, 2) Co-Feeding of CO, 3) Co-Feeding of CO and H_2O

	Partial pressure (bar)				
	H_2	CO	H_2O	N_2	n-C_{16}
1	13.1			6.6	0.3
2	13.1	6.6			0.3
3	7.5	3.7	8.5		0.3

Although the skeletal rearrangement and hydrocracking of n-paraffins occurs without and with consumption of hydrogen, respectively, it is well known that the rate constant for hydroisomerisation/hydrocracking of n-paraffins is inversely proportional to the hydrogen pressure and the apparent reaction order with respect to hydrogen reported in the literature is generally −1. This hydrogen order can be explained in terms of the bi-functional mechanism

where the first step is the formation of olefins at the metal site with subsequent formation of a carbenium ion at the acidic site followed by either cracking or isomerisation and ultimately hydrogenation at the metal site. The limiting step is the skeletal rearrangement of the secondary carbenium ion; therefore, an increase in hydrogen pressure will lead to lower steady state concentrations of n-alkenes and secondary carbenium ions with a consequent decline in the limiting step rate (Calemma et al., 2000).

When, in the case of this study, the hydrogen partial pressure is lowered due to the introduction of H_2O, an increase in activity is expected on account of the above. Instead, the activity is lowered in spite of the lower hydrogen partial pressure. It thus follows that the lowered activity is entirely the result of the interaction of H_2O with the bi-functional catalyst. At the reaction temperature of 225°C water resides entirely in the vapor phase. In a three-phase trickle bed reactor, the assumption could be made that the catalyst is completely wetted by paraffins (Kumar and Froment, 2007). Nevertheless, in spite of the liquid paraffins and olefins that are adsorbed onto the zeolite surface and in the pores and which are hydrophobic in nature, water has a substantial detrimental effect on the activity.

An increase in the reaction temperature increases the activity in the presence of H_2O and CO more than with co-feeding of CO alone. At 225°C, 4.46% total conversion is reached; with increase in temperature to 235°C the total conversion increases to 42.6%. Thus it can be said that the effect of H_2O poisoning can be partially lifted at a higher reaction temperature.

As with CO poisoning, H_2O co-feeding leads to an increase of the unsaturated and the branched products, although the effect is more dramatic with H_2O than with CO. The median of the entire product distribution is also shifter towards a lower carbon number as may be observed in Figures 5.9 and 5.12 for the $Pd01_BHMFI$ and $Pd10_CHMFI$ catalysts, respectively. With H_2O, up to 25% of the products are unsaturated, the degree of saturation being lower in the branched products.

6.4 Compatibility of F-T Conditions and n-C_{16} Hydrocracking

The purpose of all of the above is to establish whether or not the bi-functional hydrocracking catalyst retains enough activity under operating conditions that are typical for the Fischer-Tropsch synthesis. In this study those conditions have been simulated by co-feeding CO and H_2O to the hydrocracking experiment at feed flow rates such that the H_2/CO molar ratio equals 2 and the H_2O to n-C_{16} molar ratio is approximately equal to 16. The latter number arises from the fact that for each $–CH_2–$ monomer of every Fischer-Tropsch product one H_2O molecule is co-produced.

In Table 6.2 hydrocracking reaction rates experimentally determined from this work with a $Pd10_CHMFI$ catalyst and the F-T reaction rate are compared. The rate of formation of hydrocarbons in F-T synthesis over a cobalt catalyst is based on 85% CO conversion and the hypothetical 100% selectivity towards n-C_{16}.

Table 6.2: Comparison of Hydrocracking Reaction Rates on $Pd10_CHMFI$ Catalyst with the Rate of Formation of Hydrocarbons in F-T synthesis over Cobalt Catalysts.

	Hydrocracking and Co-feed CO	Hydrocracking and Co-feed CO and H_2O	Fischer-Tropsch
Temperature (°C)	Conversion (%)		
230	46	17	85
235	62	43	
	Rate ($t_{n\text{-}C16}$ / $t_{catalyst}$ · h)		
230	0.50	0.18	0.48
235	0.67	0.47	

When F-T conditions are applied to 1wt.% Pd based hydrocracking catalyst, the reaction rate at 235°C is comparable to the rate of formation of hydrocarbons in F-T synthesis at 230°C. Alternatively, at 230°C F-T synthesis (normalized to C_{16}) is 2 – 3 times faster than C_{16} hydrocracking under identical conditions such that an F-T/hydrocracking catalyst blend of 1:2 and 1:3 (m/m) should make combined F-T/hydrocracking a practical possibility.

7 Conclusion

Due to the growing demand for transportation fuels and stringent legislation of fuel specifications, interest in the overall GTL environment has increased. The conversion of the heavy hydrocarbon wax to clean distillate fuels is a particular area of interest.

This study focused on the activity of the hydrocracking catalyst, Pd/SiO_2 in combination with H-MFI zeolite, under the operating conditions identical to that of the low temperature F-T synthesis. The product distribution obtained is strongly dominated by secondary cracking reactions and remains similar with increasing reaction temperature and conversion. The catalyst used for this study, H-MFI zeolite is a very strong acid catalyst. Secondary cracking of primary cracked products occur with increased acid strength of the catalyst.

This work has shown that CO present in the feed poisons the catalyst and thus reduces the catalyst activity. The presence of CO inhibits the metal function to rehydrogenate the unsaturated products. The presence of unsaturated and branched products prove this to be true. As with CO, the presence of water in the feed reduces the catalyst activity and the saturation of the cracked products is significantly reduced. Olefinicity increases in the presence of CO and more so in the presence of CO/H_2O. The impact of CO and CO/H_2O on the n-C_{16} conversion appears to be significant with catalyst having a higher metal loading. It is seen that the product of the catalyst with the higher metal loading is more saturated than that of the catalyst with the lower metal loading.

This study has shown that hydrocracking under F-T conditions aggravates the departure from ideal hydrocracking. From the product distribution obtained it was clear that only very little methane is formed. The absence of methane in the product spectrum indicates that hydrogenolysis does not occur. It is also been shown that the suppression of the catalyst activity in the presence of CO and CO/H_2O is completely reversible in the temperature range identical to that of the LTFT synthesis. From the data obtained in this study it can be clearly stated that the overall combined low temperature F-T synthesis and the hydrocracking of long chain paraffins seems possible.

It is recommended that further research be conducted utilizing various metal loadings to determine the relationship between conversion and catalyst metal loading and to verify that the activity becomes independent of the metal content in the catalyst at higher metal loadings. Furthermore, the deactivation of the catalyst by feeding CO and H_2O should be measured independently to determine if the suppression of the activity is more significant with CO or H_2O.

References

Alvarez, F., Ribeiro, F.R., Perot, G., Thomazeau, C. and Guisnet, M., 1996. *Hydroisomerisation and Hydrocracking of Alkanes: 7. Influence of the Balance Between Acid and Hydrogenating Functions on the Transformation of n-Decane on PtHY Catalysts*. Journal of Catalysis, volume 162, pp. 179–189

Atkins, P., de Paula, J., 2006. *Atkins' Physical Chemistry*. Oxford University Press, New York, 7th edition

Böhringer, W., Kotsiopoulus, A., de Boer, M., Knottenbelt, C. and Fletcher, J.C.Q., 2007. *Selective Fischer-Tropsch Wax Hydrocracking: Opportunity for Improvement of Overall Gas-to-Liquids Processing*. Studies in Surface Science and Catalysis, volume 163, pp. 345–365

Calemma, V., Peratello, S. and Perego, C., 2000. *Hydroisomerisation and Hydrocracking of Long Chain n-Alkanes on Pt/Amorphous SiO_2-Al_2O_3 catalyst*. Applied Catalysis A: General, volume 190, pp. 207-218

Chavarria, V., Ramirez, J., Gonzalez, H. and Baltanas, M.A., 2004. *Modeling of n-Hexadecane Hydroisomerisation and Hydrocracking Reactions on a Mo/HB-alumina Bi-functional Catalyst, using the Single Event Concept*. Catalysis Today, volume 98, pp. 235-242

Cengel, Y.A., Boles, M.A., 2001. *Thermodynamics: An Engineering Approach*. McGraw-Hill, 4th edition

Chen, N.Y., 1976. *Hydrophobic Properties of Zeolites*. The Journal of Physical Chemistry, volume 80, no. 1, pp. 60-63

Dalai, A.K. and Davis, B.H., 2008. *Fischer-Tropsch Synthesis: A Review of Water Effects on the Performances of Unsupported and Supported Co Catalysts*. Applied Catalysis, volume 20, pp. 239-281

De Klerk, A., 2007. *Environmentally Friendly Refining: Fischer-Tropsch versus Crude Oil*. The Royal Society of Chemistry, volume 9, pp. 560-565

Denayer, J., Ocakoglu, A., De Jonkheere, B., Martens, J., Thybaut, J., Marin, G. and Baron, G., 2003. *Adsorption Competition Effects in Hydroconversion of Alkane Mixtures on Zeolites*. International Journal of Chemical Reactor Engineering, volume 1. Article: A36

Dry, M., 2001. *High Quality Diesel via the Fischer-Tropsch Process - A Review*. Journal of Chemical Technology and Biotechnology, volume 77, pp. 43–50

Eilers, J., Posthuma, S.A. and Sie, S.T., 1990. *The Shell Middle Distillate Synthesis Process (SMDS)*. Catalysis Letters, volume 7, pp. 253-270

Fernandes, F.A.N. and Teles, U.M., 2007. *Modeling and Optimization of Fischer-Tropsch Products Hydrocracking*. Fuel Processing Technology, volume 88, no. 2, pp. 207-214

Fletcher, J.C.Q., Böhringer, W. and Kotsiopoulos, A., 2004. *Selective Fischer-Tropsch Wax Hydrocracking – Opportunity for Improvement of Overall Gas-To-Liquids Processing*. International R&D Forum on Oil, Gas and Petrochemicals, Malaysia, 5 – 6 April

Girgis, M.J. and Peter Tsao, Y., 1996. *Impact of Catalyst Metal-Acid Balance in n-Hexadecane Hydroisomerisation and Hydrocracking*. Ind. Eng. Chem. Res., volume 35, pp. 386-396

Kotsiopoulos, A 2005, '*The Hydrocracking of Fischer-Tropsch Wax Using n-Tetradecane as a Model Compound*', MSc Thesis, University of Cape Town. Retrieved January 20, 2009, from University of Cape Town Digital Theses.

Kukard, R.S., 2008, '*The Effect of Zeolite Type on the Hydrocracking of Long n-Paraffins*', MSc Thesis, University of Cape Town. Retrieved June 5, 2009, from University of Cape Town Digital Theses.

Kumar, H., 2004, '*Single Event Kinetic Modeling of the Hydrocracking of Paraffins*', MSc Thesis, University of Cape Town. Retrieved August 12, 2009, from University of Cape Town Digital Theses.

Kumar, H. and Froment, G.F., 2007. *A Generalized Mechanistic Kinetic Model for the Hydroisomerisation and Hydrocracking of Long Chain Paraffins*. Ind. Eng. Chem. Res., volume 46, pp. 4075-4090

Jiang, H., Yang, H., Hawkins, R. and Ring, Z., 2007. *Effect of Palladium on Sulphur Resistance in Pt-Pd Bimetallic Catalysts*. Catalysis Today, volume 125, pp. 282-290

Leckel, D., 2005. *Hydrocracking of Iron-Catalyzed Fischer-Tropsch Waxes*. Energy and Fuels, volume 19, pp. 1795-1803

Leckel, D., 2007. *Low-Pressure Hydrocracking of Coal-Derived Fischer-Tropsch Waxes to Diesel*. Energy and Fuels, volume 21, pp. 1425–1431

Leckel, D. and Liwanga-Ehumbu, M., 2006. *Diesel-Selective Hydrocracking of an Iron-Based Fischer-Tropsch Wax fraction (C_{15}-C_{45}) using a MoO_3-Modified Noble Metal Catalyst*. Energy Fuels, volume 20, no. 6, pp. 2330-2336

Li, X., Asami, K., Luo, M., Michiki, K., Tsubaki, N. and Fujimoto, K., 2003. *Direct Synthesis of Middle Iso-Paraffins from Synthesis Gas*. Catalysis Today, volume 84, pp. 59-65

Liu, Z., Li, X., Asami, K. and Fujimoto, K., 2005. *Formation of Isoparaffins through Pd/β Zeolite Application in Fischer-Tropsch Synthesis*. Energy and Fuels, volume 19, pp. 1790-1794

Martens, J. and Jacobs, P., 1997. *Reaction Mechanisms of Acid-Catalyzed Hydrocarbon Conversions in Zeolites*. Handbook of Heterogeneous Catalysis, volume 3, pp. 1137-1148

Martens, J.A., Jacobs, P.A. and Weitkamp, J., 1986. *Attempts to Rationalize the Distribution of Hydrocracked Products. Qualitative Description of the Primary Hydrocracking Modes of Long Chain Paraffins in Open Zeolites*. Applied Catalysis, volume 20, pp. 239-281

Möller, K., le Grange, P. and Accolla, C., 2009. *A Two-Phase Reactor Model for the Hydrocracking of Fischer-Tropsch-Derived Wax*. Ind. Eng. Chem. Res., volume 48, pp. 3791-3801

Nicholls, T (ed.), 2007. *GTL with a Difference*. Fundamentals of the Global Oil and Gas Industry, p. 101

Olson, D.H., Haag, W.O. and Borghard, W.S., 2000. *Use of Water as a Probe of Zeolitic Properties: Interaction of Water with HZSM-5*. Microporous and Mesoporous Materials, volume 35-36, pp. 435-446

Panagiotopoulou, P., Kondarides, D.I. and Verykios, X.E., 2008. *Selective Methanation of CO over Supported Nobel Metal Catalyst: Effects of the Nature of the Metallic Phase on Catalytic Performance*. Applied Catalysis A: General, volume 344, pp. 45-54

Park, K. and Ihm, S., 2000. *Comparison of Pt/Zeolite Catalysts for n-Hexadecane Hydroisomerisation*. Applied Catalysis A: General, volume 203, pp. 201–209

Ramachandran, C.E., Chempath, S., Broadbelt, L.J. and Snurr, R.Q., 2006. *Water Adsorption in Hydrophobic Nanopores: Monte Carlo Simulations of Water in Silicalite*. Microporous and Mesoporous Materials, volume 90, pp. 293-298

Rossetti, I., Gambaro, C. and Calemma, V., 2009. *Hydrocracking of Long Chain Linear Paraffins*. Chemical Engineering Journal, volume 154, pp. 295-301

Sandler, S.I, 1999. *Chemical and Engineering Thermodynamics*. John Wiley & sons, New York, 4th edition

Scherzer, J. and Gruia, A.J., 1996. *Hydrocracking Science and Technology*. Marcel Dekker Inc., New York, 1st edition

Shimoyama, Y., Haruki, M., Iwai, Y. and Arai, Y., 2002. *Measurement and Prediction of Liquid-liquid Equilibria for Water + Hexane + Hexadecane, Water + Toluene + Decane, and Water + Toluene + Ethylbenzene Ternary Systems at High Temperatures and Pressures*. Journal of Chemical Engineering Data, volume 47, no. 5, pp. 1232–1236

Sie, S., Senden, M. and van Wechem, H., 1991. *Conversion of Natural Gas to Transportation Fuels via the Shell Middle Distillate Synthesis Process (SMDS)*. Catalysis Today, volume 8, pp. 371–394

Thybaut, J.W., Laxmi Narasimhan, C.S., Denayer, J.F., Baron, G.V., Jacobs, P.A., Martens, J.A. and Marin, G.B., 2005. *Acid-Metal Balance of a Hydrocracking Catalyst: Ideal versus Non-Ideal Behavior*. Ind. End. Chem. Res., volume 44, pp. 5159-5169

Van Gruijthuijsen, L.M.P., Louwers, S.P.A., Van Santen, Z.R.A. and Niemantsverdriet, J.W., 1997. Catalysis Letters, volume 43, pp. 45-49

Van Vliet, O.P.R., Faaij, A.P.C. and Turkenburg, W.C., 2009. *Fischer-Tropsch Diesel Production in a Well-to-Wheel Perspective: A Carbon, Energy Flow and Cost Analysis*. Energy Conversion and Management, volume 50, pp. 855-876

Visconti, C.G., Tronconi, E., Lietti, L., Zennaro, R. and Forzatti, P., 2007. *Development of a Complete Kinetic Model for the Fischer-Tropsch Synthesis over Co/Al_2O_3 Catalysts*. Chemical Engineering Science, volume 62, pp. 5338-5343

Weitkamp, J. and Ernst, S., 1988. *Shape Selective Hydroconversion of Hydrocarbons: A Powerful Tool for Characterizing the Effective Pore Width of Zeolites and Related Materials.* Studies in Surface Sciences and Catalysis, volume 38, pp. 367–382

Weitkamp, J., Jacobs, P. and Martens, J., 1983. *Isomerisation and Hydrocracking of C9 through C16 n-Alkanes on Pt/HZSM-5 Zeolite. Applied Catalysis*, volume 8, pp. 123–141

Appendix A – Post Reactor Effluent Vaporization

A.1 Introduction

The system is set up for online gas chromatographic analysis. Therefore, the reactor effluent needs to be vaporized and downstream condensation of the sample prevented. Figure A.1 displays the original design of the post reactor effluent vaporization process. The reactor effluent is diluted, passes through a t-shaped filter followed by the back-pressure regulator and is subsequently vaporized at ambient pressure. The effluent from the trickle phase reactor is composed of a gas phase and a liquid phase. The liquid collects in the dead volume within the back-pressure regulator. Any slight temperature perturbation of the back pressure affects the vapor pressure in equilibrium with the liquid, making it very difficult if not impossible to guarantee steady-state flow of the effluent stream. This design was eventually abandoned.

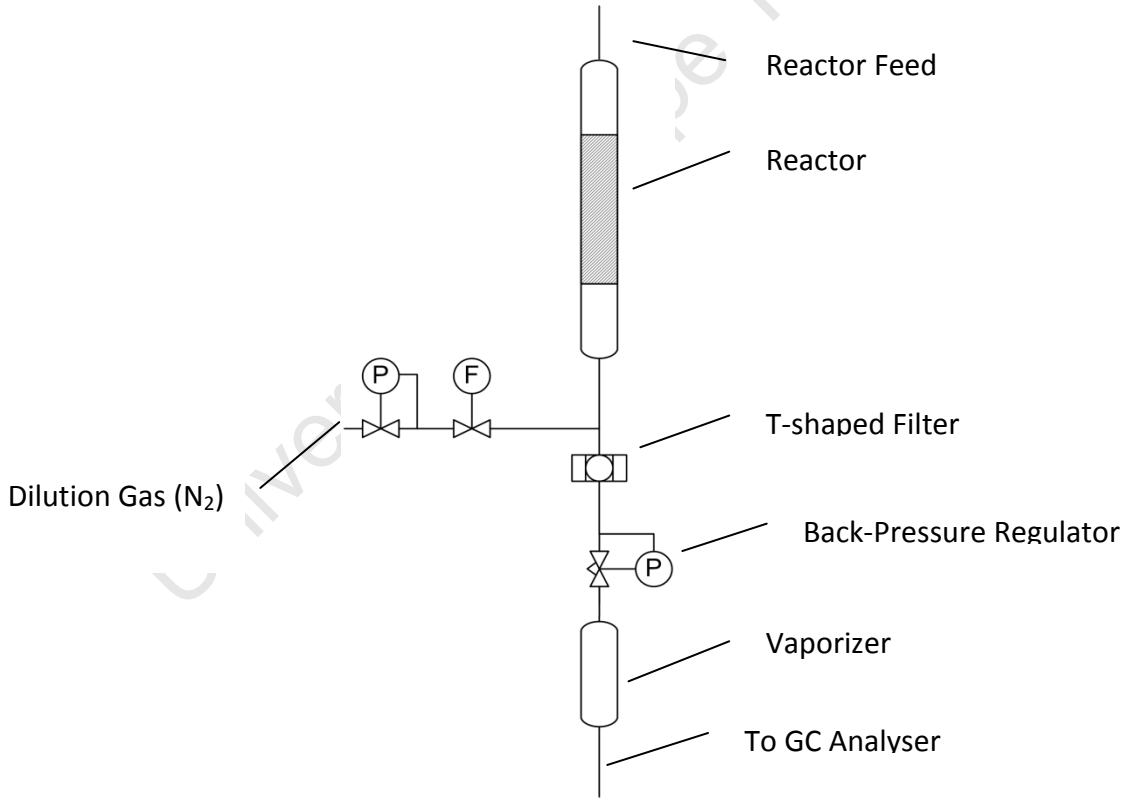

Figure A.1: Initial Design

A.2 Comparison of Improved System Designs

In the design, referred to as design A, shown in Figure A.2, the diluent gas flow maintains the pressure in the reactor because of the pressure drop generated by the restricting orifice in the reactor effluent stream. This restricting orifice is an adjustable needle valve. Partially liquid effluent passes through the needle valve to be vaporized at ambient pressure. Design A never delivered reproducible results. Scatter was observed in all experiments with this design. The reason for this probably resides in the needle valve. In order to guarantee a sufficiently large pressure drop the needle valve will only be opened slightly. Since the reactor effluent stream is composed of a liquid as well as a gas phase, the liquid is being pushed through the orifice by the gas and will be propelled onto the hot surface of the vaporizer that immediately follows it. It can be envisaged that only small uniform (monodisperse) droplets would constitute a steady liquid output into the vaporizer. If droplets coalesce, fluctuations in the liquid effluent stream are introduced, which ultimately leads to scatter in the chromatographic samples.

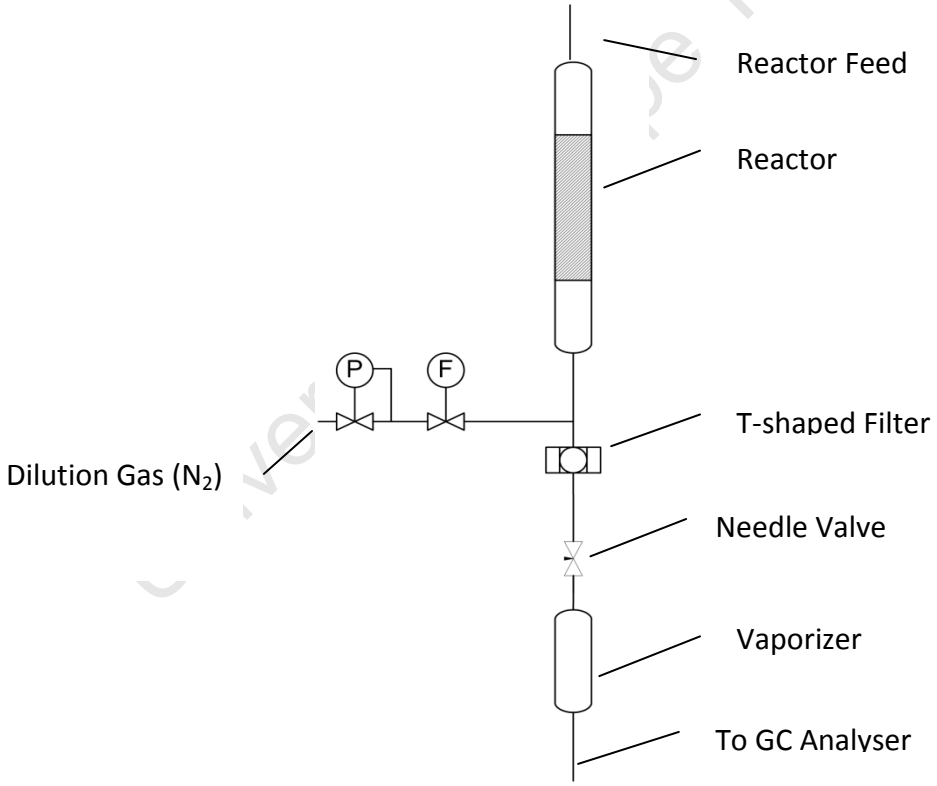

Figure A.2: Improved System Design A

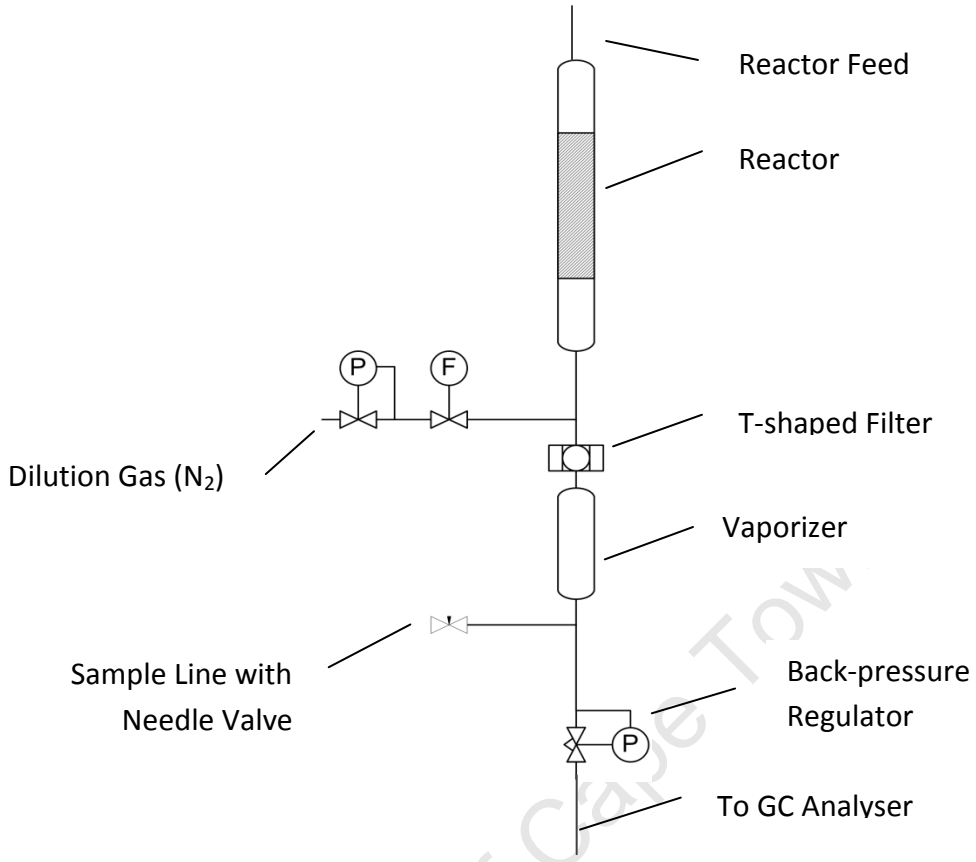

Figure A.3: Alternative Improved System Design B

Figure A.3 shows the alternative improved design, referred to as design B. The pressure in the reactor is set by a back-pressure regulator downstream of the vaporizer. Immediately below the vaporizer a sample stream branches off and a needle valve controls the flow through the sample line. Vaporization is achieved at the elevated pressure of the reactor, such that a higher temperature is required for vaporization than is the case for design A.

A.3 Obtaining a Steady State Flow of $C_{16}H_{34}$ to the FID; the Blank Run

A blank experiment was performed to evaluate whether or not steady state performance of the test unit could be obtained. A steady-flow process can be defined as a process during which a fluid flows through a control volume steadily. That is, the fluid properties can change from point to point within the control volume, but at any fixed point they remain the same during the entire process (steady means no change with time). No properties change at the boundaries of the control volume with time (Cengel and Boles, 2001). It follows that the mass flow rate of the fluid at an opening must remain constant. This then, in turn, means that the

composition of the reactor effluent stream remains constant and that the partial pressure and/or the molar fraction of C_{16} remain constant. To verify whether or not this condition is met, the reactor effluent stream is sampled over time and a plot of C_{16} sample mass plotted as a function of time.

The reactor feed comprised of 50 sccm H_2, 0.01 ml/min liquid $C_{16}H_{34}$ and the N_2 diluent flow was 500 sccm. Plots of $C_{16}H_{34}$ chromatographic peak height versus time are used to assess the steady state flow of feed through the system. Serious scatter was observed almost immediately. First attempts at finding a remedy focused on the automated injection of the sample onto the GC column. It was believed that condensation of $C_{16}H_{34}$ in the 1/16" tubing of the sample loop in the injector port or in the split vent or septum purge might have been responsible for the observed scatter. None of these hypotheses were ultimately confirmed and the search then turned to the test unit itself.

The t-shaped filter was not heated and provided a dead volume for the $C_{16}H_{34}$ to accumulate in. To avoid accumulation of liquid in the filter and, consequently, unsteady state flow of $C_{16}H_{34}$, the filter would need to be heated to vaporize the reactor effluent. This was attempted by wrapping it in a flexible glass fiber coated heating tape. Because the filter is rather bulky compared to the 1/4" tubing leading to and from it, it is very difficult to heat this connecting section between reactor and vaporizer while trying to avoid the creation of hotspots. The connecting section between reactor and vaporizer, including the filter, was heated to 300°C.

Figure A.4 shows the chromatographic scatter around the average when the filter is heated. Upon this dismal result the filter was removed from the test unit and replaced by a piece of 1/4" tubing. Without the filter a good result was obtained as displayed in Figure A.5.

Then, the $C_{16}H_{34}$ flow was increased by an order of magnitude to 0.1 ml/min. Condensation occurred as is evident from the increasing peak height of $C_{16}H_{34}$ in Figure A.6. Eventually, after every other option had been discarded, it was found that condensation in the sample loop of the sampling valve was responsible for the observed behavior since an increase in the temperature of the heated valve enclosure from 200°C to 250°C removed the problem. Reproducible peak height of consecutive injections of $C_{16}H_{34}$ containing effluent was observed (Figure A.7).

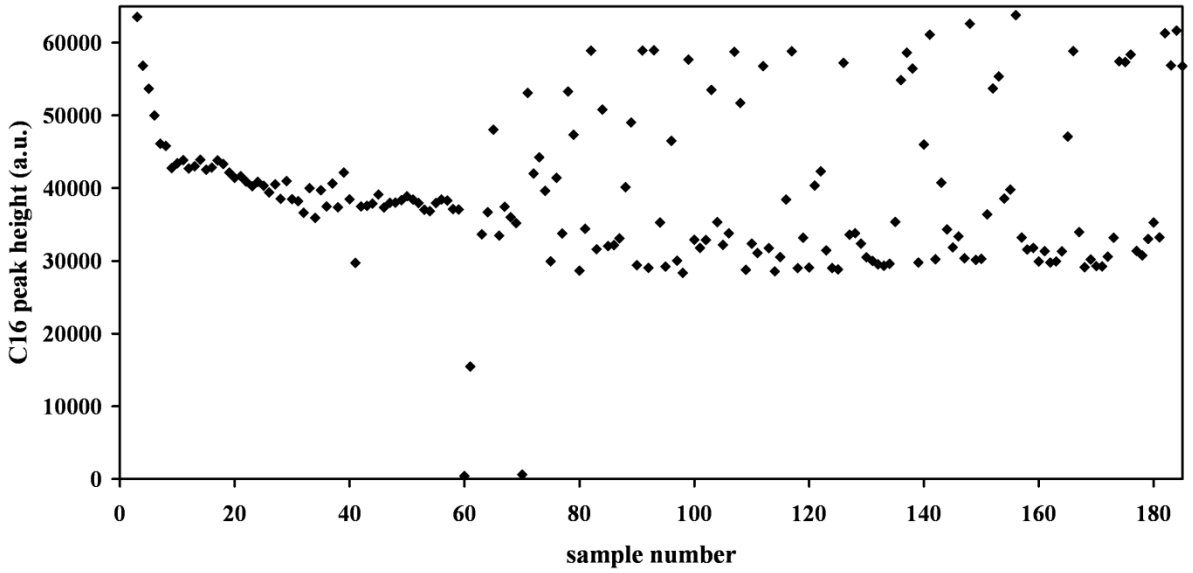

Figure A.4: Representation of Observed Chromatographic Scatter when Filter is Heated

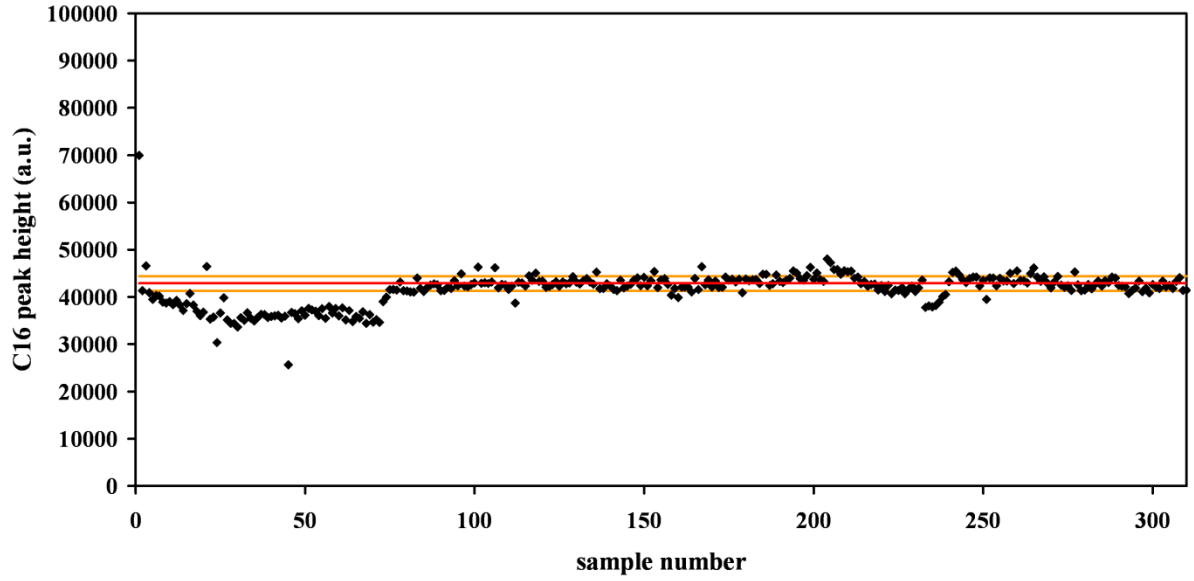

Figure A.5: $C_{16}H_{34}$ Chromatographic Reproducibility in the Absence of the Filter

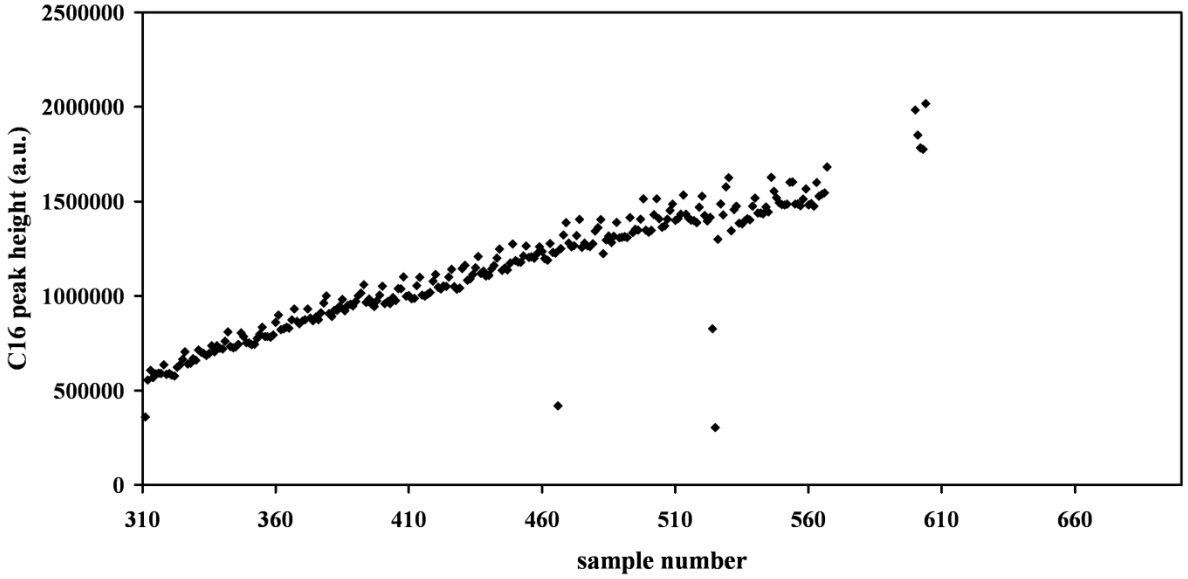

Figure A.6: Chromatographic Representation of Condensation in the Sample Loop

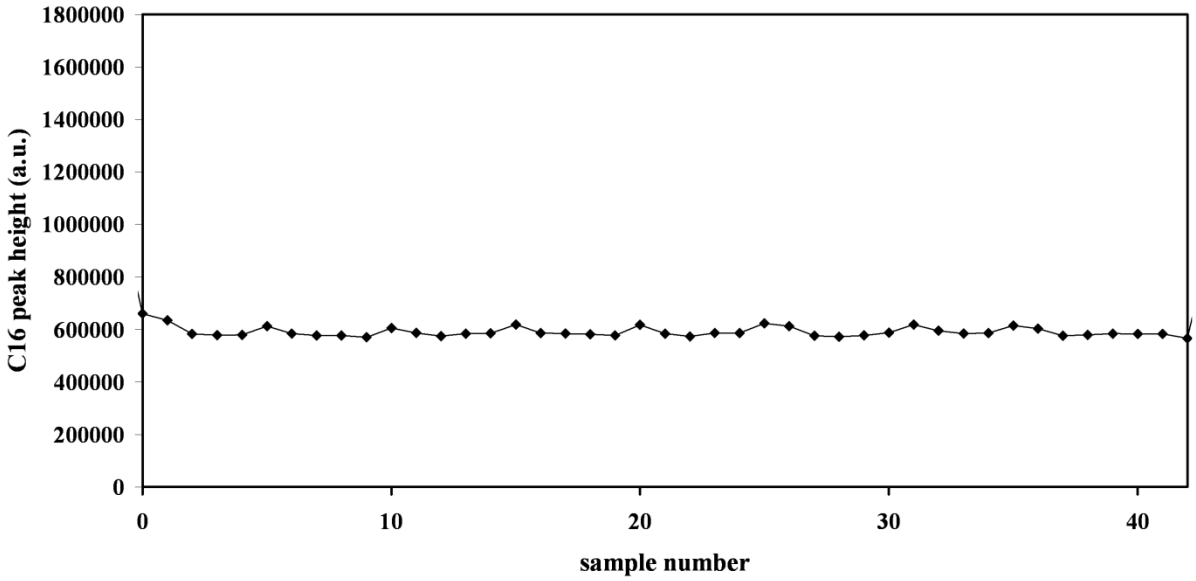

Figure A.7: Chromatographic Reproducibility at a Sample Loop Temperature of 250°C

Upon lowering the N_2 dilution flow from 500 sccm to 250 sccm scatter was reintroduced into the data (Figure A.8). Sample flow was lowered slightly by closing the needle valve to a greater extent, accounting for the apparent downward trend in the average peak height.

The entry point for the N_2 dilution flow comprised of a bored-through t-piece. The N_2 dilution flow enters horizontally from the rear and the reactor effluent tube extends to below this entry point. Liquid flows on the wall of the tubing. From the edge of the dip-tube to the wall of the t-piece the flow is discontinuous. In order for the liquid to bridge this discontinuity, it would have to form droplets that become large enough to break away from the dip-tube and fall down onto the wall. The forces that govern this process include adhesion of the liquid on the wall, surface tension of the liquid and sheer forces arising from a faster gas phase flowing over a slower liquid phase. It could be postulated that droplet formation gives rise to an unsteady state effluent flow.

To overcome droplet formation, the dip-tube was filled with glass wool that extends down so that it touches the t-piece wall. It was believed that capillary action would guide the liquid from one wall to the next thus eliminating spiked flow.

With a reactor temperature of 250°C, a vaporizer temperature of 300°C and the connecting section between vaporizer and dilution t-piece heated to 200°C, the liquid phase cools down to approximately 80°C before introduction of the dilution gas stream. The vaporizer is packed with SiC. With a dilution flow of 500 sccm, standard deviation (σ) around the mean (μ) is 3.7%. Scatter is much larger with 250 sccm N_2 dilution flow, and the data does not appear to be distributed normally around the mean. This implies an underlying physical phenomenon rather than random variation.

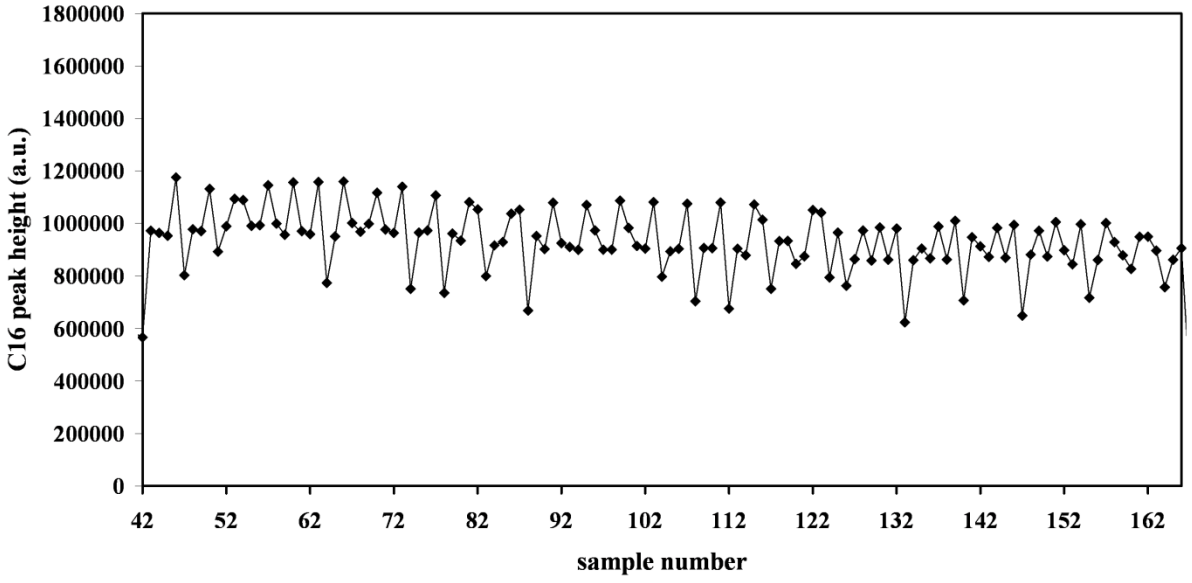

Figure A.8: Chromatographic Reproducibility with Reduced Dilution Flow of 250 sccm

To determine the cause of the scatter, N_2 dilution gas flow and N_2 feed gas flow were exchanged such that 250 sccm N_2 passed through the reactor and the dilution flow was 50 sccm. Downstream of the dilution point the composition and flow of the diluted effluent remains unchanged. Scatter was slightly reduced as is apparent in Figure A.9 (from sample number 500). At low feed gas flow and consequently high partial pressure of n-hexadecane in the reactor effluent, scatter is high whereas at higher feed gas flow and lower $C_{16}H_{34}$ partial pressure, scatter is reduced.

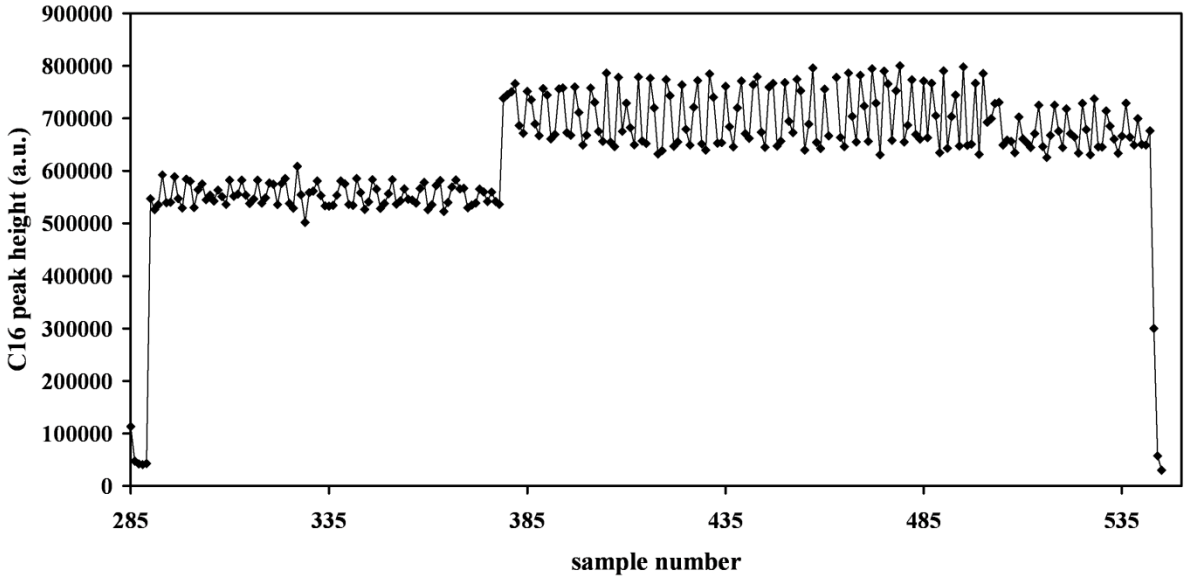

Figure A.9: Chromatographic Reproducibility with Dilution Gas Flow Rate and Feed Gas Flow Rate Exchanged

The design of the dilution entry point was then modified in order to remove the discontinuity in the contact surface with the liquid phase. The t-piece was angled at 45° with diluent gas entering from above and liquid running down smoothly. With the connecting section heated to 250°C and the vaporizer at 300°C, the angled arrangement did not result in steady state flow as is apparent from Figure A.10, sample 1 to 30. Another possible cause of scatter is a very steep temperature gradient. When liquid heats up faster than it can evaporate, it reaches a state of superheating which may lead to flash boiling. Boiling occurs in three characteristic stages, which are nucleate, transition and film boiling. These stages generally take place from low to high surface temperatures, respectively. Flash evaporation may also occur at the dilution point as a result of a sharp decrease in liquid partial pressure.

The heating of the connecting section was terminated and the top heater band of the vaporizer was also removed (sample 30 to 70). Then the space between reactor and vaporizer was wrapped in an insulation blanket (sample 70 to 90). Ultimately the vaporizer temperature was

lowered to 250°C. This led to steady state performance of the test unit blank experiment, with a standard deviation of 3.1% around the mean (Figure A.11).

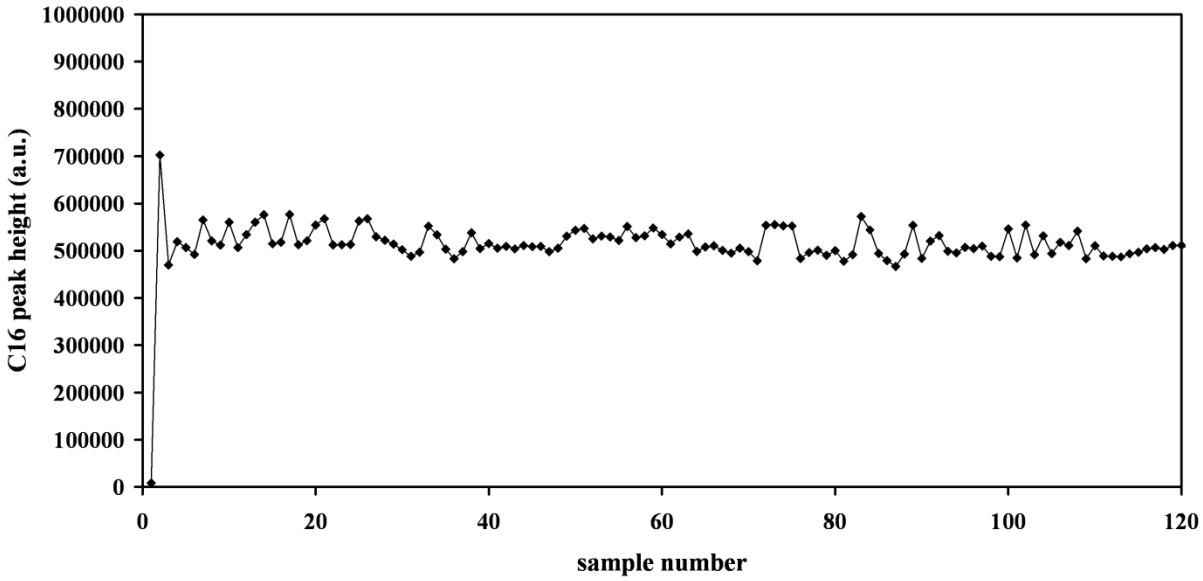

Figure A.10: Chromatographic Reproducibility with the T-Piece of the Dilution Entry Point at an Angled Position, Scatter Observed

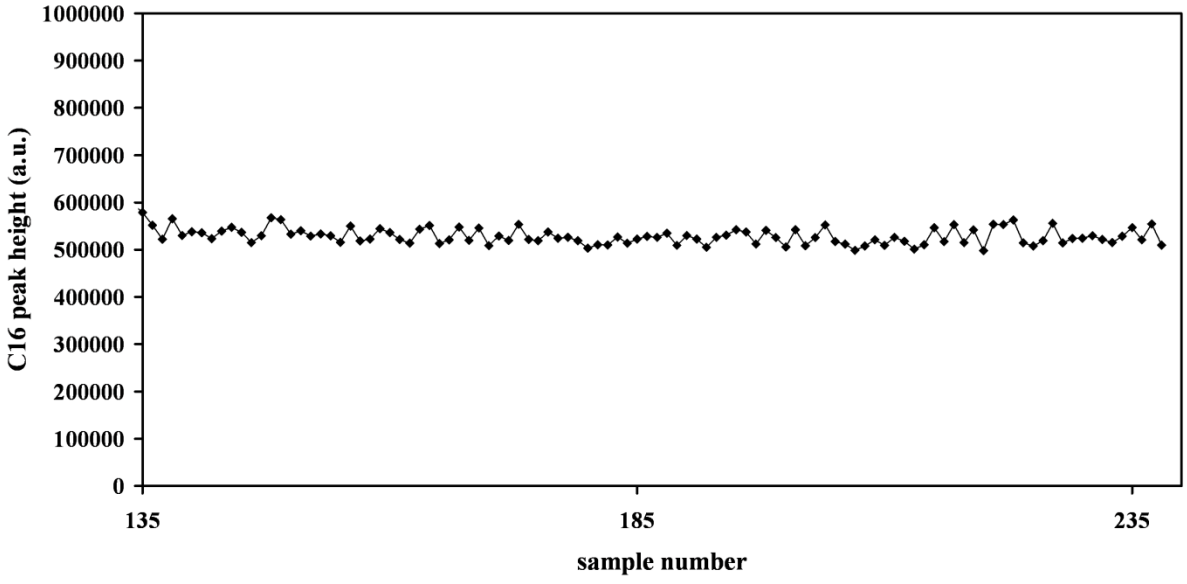

Figure A.11: Chromatographic Reproducibility with the Vaporizer Temperature Lowered to 250°C

Further blank tests were aimed at improving the heating profile, i.e. removing temperature gradients where possible. This necessitated heating the entire connecting section without creating hotspots and assuring that the heat is distributed evenly as well as lowering the temperature of the vaporizer as far as possible.

To heat the connecting section, tubing was encased in a metal conduit with a diameter of 25 mm. Heating wire was wound around the conduit followed by a layer of sticky aluminum foil and insulating glass fiber cloth. The entire section was insulated by an insulating jacket to further improve heat distribution. The vaporizer temperature was 250°C. With 50 sccm of reactor gas feed, 500 sccm of dilution gas feed and 0.1 ml/min liquid n-hexadecane feed, the partial pressure of n-hexadecane ($3.0 \cdot x\ 10^4$ Pa) is well below the vapor pressure at 250°C ($6.0 \cdot x\ 10^4$ Pa). Steady state performance was thus achieved (Figure A.12) but the standard deviation (3.2%) could not be further improved.

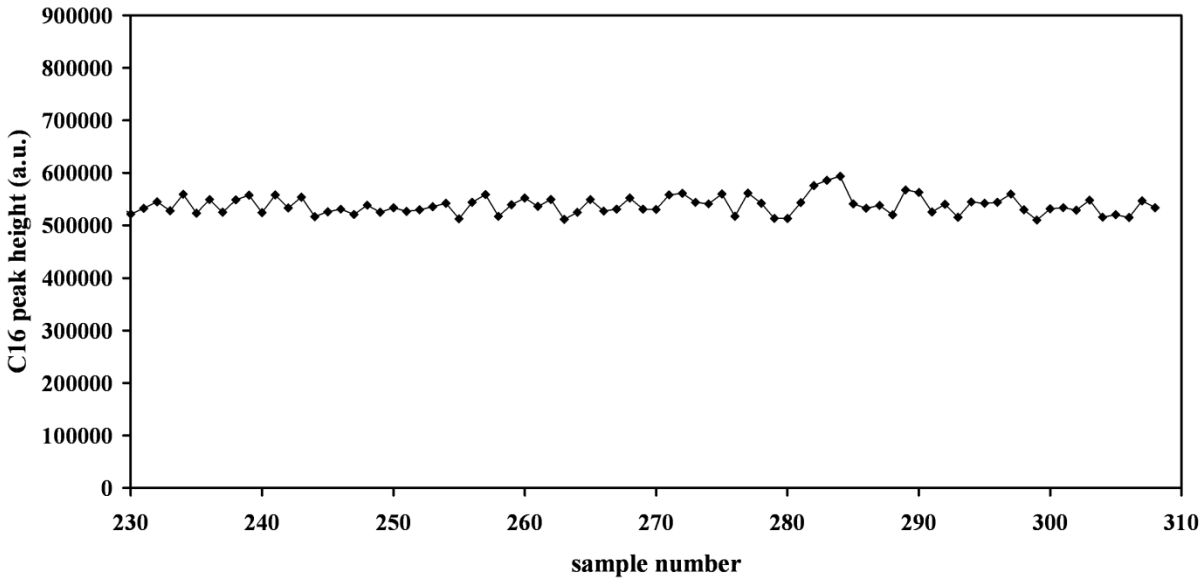

Figure A.12: Chromatographic Reproducibility showing No Significant Improvement with the Redesigned Heating Arrangement

At half the dilution flow (250 sccm), the partial pressure of n-hexadecane ($5.5 \cdot x\ 10^4$ Pa) is still just below the vapor pressure at 250°C ($6.0 \cdot x\ 10^4$ Pa). Nevertheless, scatter appeared in the sampling data (Figure A.13). Neither an increase in vaporizer temperature nor an increase or decrease in the temperature of the connecting section made any meaningful difference. By increasing the split ratio at the GC injector port from 50 to 100, steady state performance with a standard deviation of 3.2% was once again obtained (Figure A.14). These conditions

represent the worst case scenario for hydrocracking experiments, i.e. no conversion at the highest n-hexadecane space velocity with the minimal amount of heating and the minimal amount of dilution. Increasing the split ratio at the injector port, leads to a relatively small increase in gas consumption.

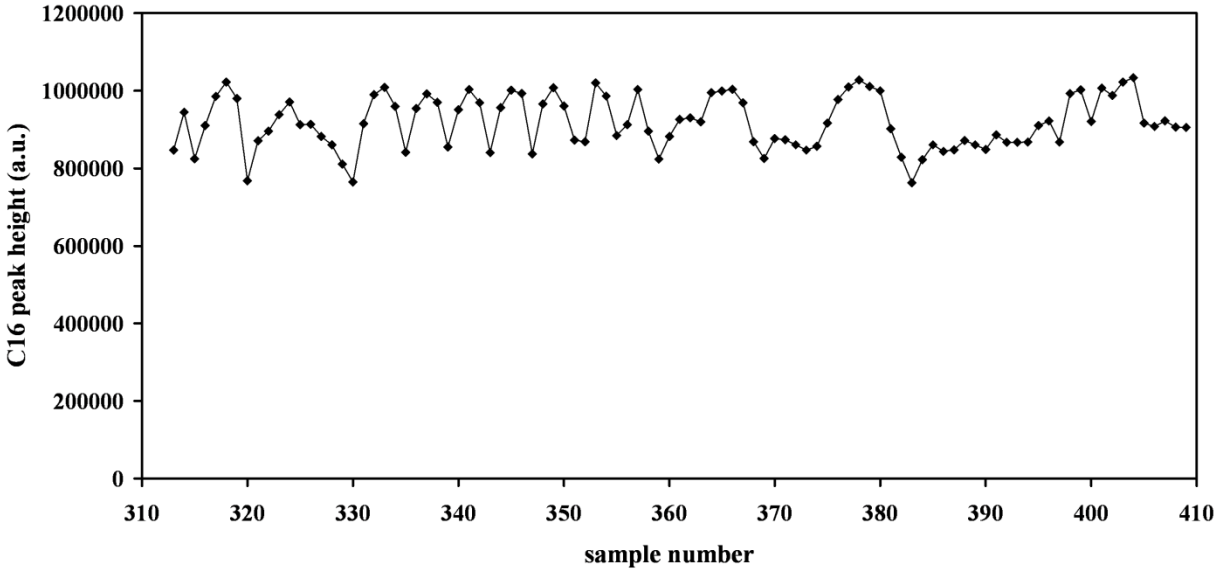

Figure A.13: Chromatographic Representation at 'High' n-C_{16} Feed Flow Rate

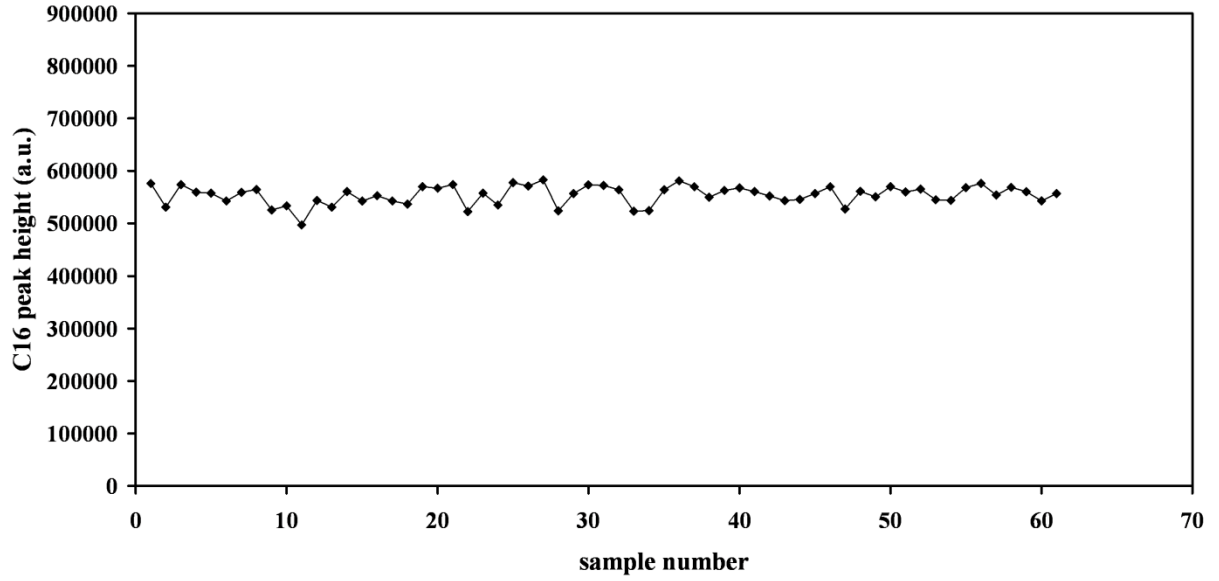

Figure A.14: Chromatographic Reproducibility with Increased Split Flow in the GC Injector

A.4 Recommendations for Further Reducing Temperature Gradients

The vaporizer tube is surrounded by a big brass block which conducts heat very efficiently. When only heated by the bottom heater band that covers half the brass block and without the top heater band in place so as to remove excess insulation, the top of the block still measures almost the same temperature as the set temperature at the bottom of the block. Only the edge of the block is slightly cooler than the center. A brass block, therefore, does not lend itself to creating a temperature gradient in the vaporizer tube ranging from slightly below to slightly above the boiling point of the highest boiling compound in the reactor effluent, preferably over the entire length of the vaporizer tube.

The brass heating blocks were discarded to improve the vaporizer heating. Instead a metal conduit of 1" diameter was installed around the vaporizer tube and the connecting tubes extending all the way to the back pressure regulator at the bottom about 10 beyond the sample tee. Resistive heating wire is wound in the spiral groove around the metal conduit. A metal conduit with an increasingly densely coiled heating wire is able to impose a reasonably flat temperature gradient onto the vaporizer tube. Proper insulation of this heating system alleviates any remaining hotspots, since the metal conduit acts as an oven in which heat is distributed by convection as well as, to a lesser extent, conduction through the walls of the tubing and through contact between the tubing and the metal conduit. Several approaches to winding the heating wire were required to obtain a smooth temperature gradient along the length vaporizer as shown in Figure A.15.

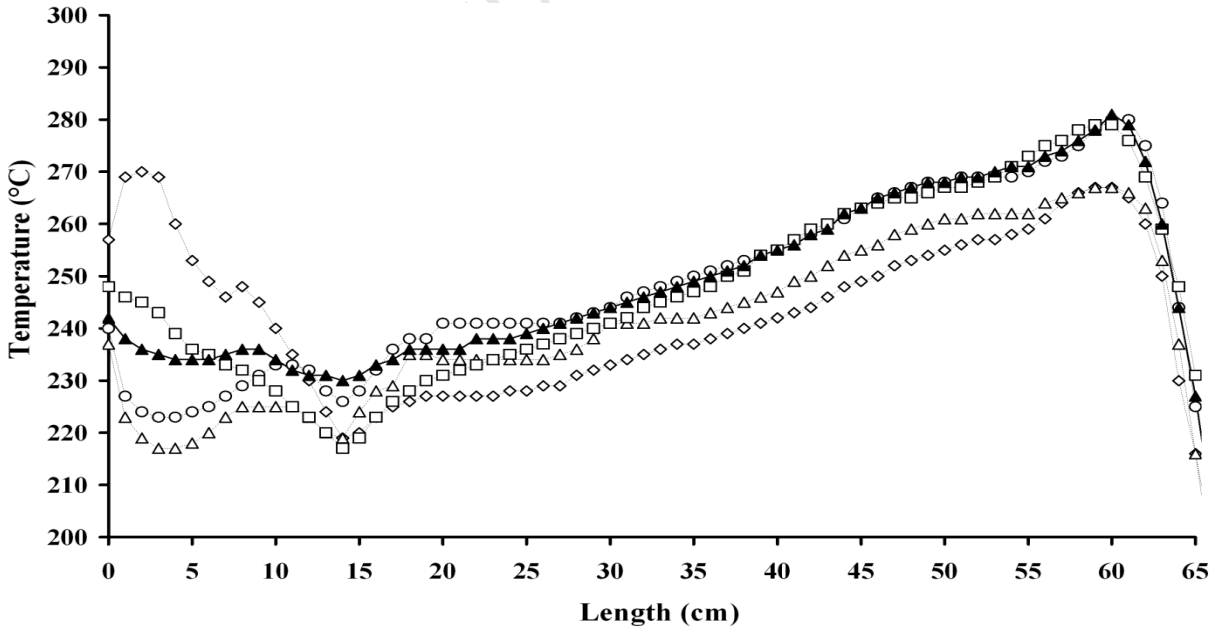

Figure A.15: Vaporizer Temperature Profile

The temperature increases or decreases at no more than 2°C/cm along any part of the vaporizer. In the example shown in Figure A.15 the temperature gradually decreases from the reactor temperature of 250°C to the lowest temperature at the point where the nitrogen dilution flow is introduced from where it steadily increases to the hottest point at which the sample line branches off. The temperature of the entire heating zone is controlled by a thermocouple inside the tube at the sampling point branch-off. The temperature couple tip is only in contact with the gaseous and diluted reactor effluent.

A.5 Application of the Improved Design to Two More Test Units

Another two test units with two reactor tubes each were rebuilt using the above design. The following documents the commissioning of these test units and the conclusions drawn from this process. The two test units were run in parallel.

The initial blank tests were poor. Under the following conditions; reactor temperature 225°C, vaporizer temperature (controlled at the bottom) 270°C, N_2 dilution 250 sccm, C_{16} 0.03 ml/min liquid, H_2 50 sccm, standard deviation of the C_{16} peak height was 6.9 and 10.9 in the left and right test units, respectively. All settings were identical, but the temperature profile of the vaporizers was dissimilar. Figure A.16 shows the blank test result with the temperature profile of the vaporizer for both left and right test units.

Two observations need to be made:

1) Although the temperature profile is 'smooth', the C_{16} output is considerably scattered, and

2) The scatter is larger for the higher vaporizer temperature in the right test unit. More precisely, the temperature at the dilution point is higher in the right test unit than in the left test unit.

When subsequently in the right unit, the N_2 dilution gas was rerouted to the top of the reactor instead of at the bottom between reactor and vaporizer tubes, the scatter was slightly reduced from 10.9% to 7.7%. This suggests that the C_{16} liquid flowing out of the reactor and into the vaporizer is evaporated too quickly and unsteadily. Flash evaporation or boiling occurs resulting in scatter in the C_{16} output signal: the C_{16} peak heights in the chromatograms. In the previous sections it was demonstrated that a sharp temperature gradient could lead to boiling and consequently scatter. In this instance, flash evaporation occurs when the reactor effluent is diluted with nitrogen. Table A.1 lists the partial pressure of C_{16} (P_{C16}) in the reactor and at the dilution point and the vapor pressure of C_{16} (P*) at the temperatures that prevail in the reactor and at the dilution point for the left and right test unit during the blank experiment.

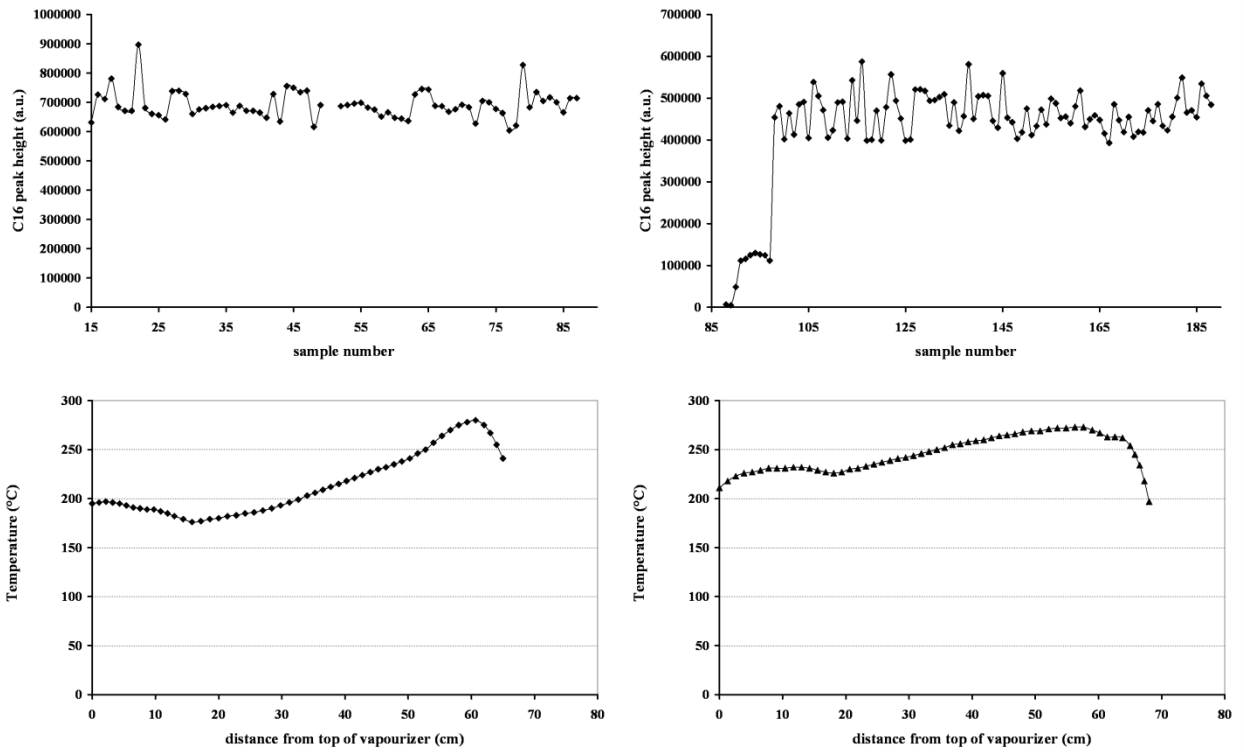

Figure A.16 (a), (b), (c) and (d): Chromatographic Comparison of the Output from Identical Test Units and their Vaporizer Temperature Profiles.

Table A.1: Partial and Vapor Pressure of C_{16}

		Left test unit			Right test unit		
	Total Pressure	Temp	Partial Pressure, P_{C16}	Vapor Pressure, P*	Temp	Partial Pressure, P_{C16}	Vapor Pressure, P*
	bar	°C	bar	bar	°C	bar	bar
Reactor	21	225	1.00	0,25	225	1.00	0,25
Dilution entry	21	176	0,17	0,05	226	0,17	0,27
Vaporizer bottom	21	270	0,17	0,79	270	0,17	0,79
Sample line	1	200	0,0082	0,11	200	0,0082	0,11

With the flow rates as given above, C_{16} 0,03 ml/min liquid, H_2 50 sccm, N_2 250 sccm, the molar fraction of C_{16}, H_2 and N_2 are calculated. The ratio of H_2/C_{16} is 20 and the dilution ratio $N_2/(H_2+C_{16})$ is 4,9 in this case. The partial pressure of C_{16} is then simply the molar fraction times the total pressure, assuming C_{16} is vaporous. When the partial pressure exceeds the vapor pressure of C_{16} at a particular temperature condensation occurs until the partial pressure matches the vapor pressure. In the left test unit the dilution of the reactor effluent stream takes place at 176°C. At this temperature the partial pressure of the diluted effluent exceeds the vapor pressure of hexadecane. Most of the hexadecane remains liquid, but a part is evaporated. In the right test unit on the other hand, the dilution takes place at 226°C. Since at this temperature the vapor pressure of hexadecane exceeds the partial pressure of hexadecane in the diluted effluent stream, hexadecane is evaporated to entirely at the entry point of the dilution gas. Evaporation occurs suddenly in the right test unit. In the left test unit, evaporation occurs gradually as the remaining liquid hexadecane trickles down on an increasingly warm surface. This is the reason why the C_{16} output in the right test unit, where evaporation is instantaneous, displays more scatter.

A graphical illustration is helpful in determining how hexadecane is partitioned over liquid and vapor phases in the reactor and in the vaporizer and how this partition is affected upon diluting the reactor effluent stream. Figure A.17 displays a phase diagram of the H_2+C_{16} feed stream at reactor pressure (21 bar). Gibbs' phase rule allows determining the number of intensive variables that can be changed independently without disturbing the number of phases in equilibrium:

$$F = C - P + 2$$

There are 2 components in the reactor, hydrogen and hexadecane. With the pressure fixed at 21 bar, Gibb's rule reduces to F':

$$F' = 3 - P$$

This means that when two phases exist in equilibrium, one degree of freedom can be independently chosen. For instance, when both a liquid and a vapor phase co-exist, the temperature determines the composition of both the liquid and the vapor phase. With only one phase in the reactor, the vapor phase, temperature and composition can be varied independently of one another.

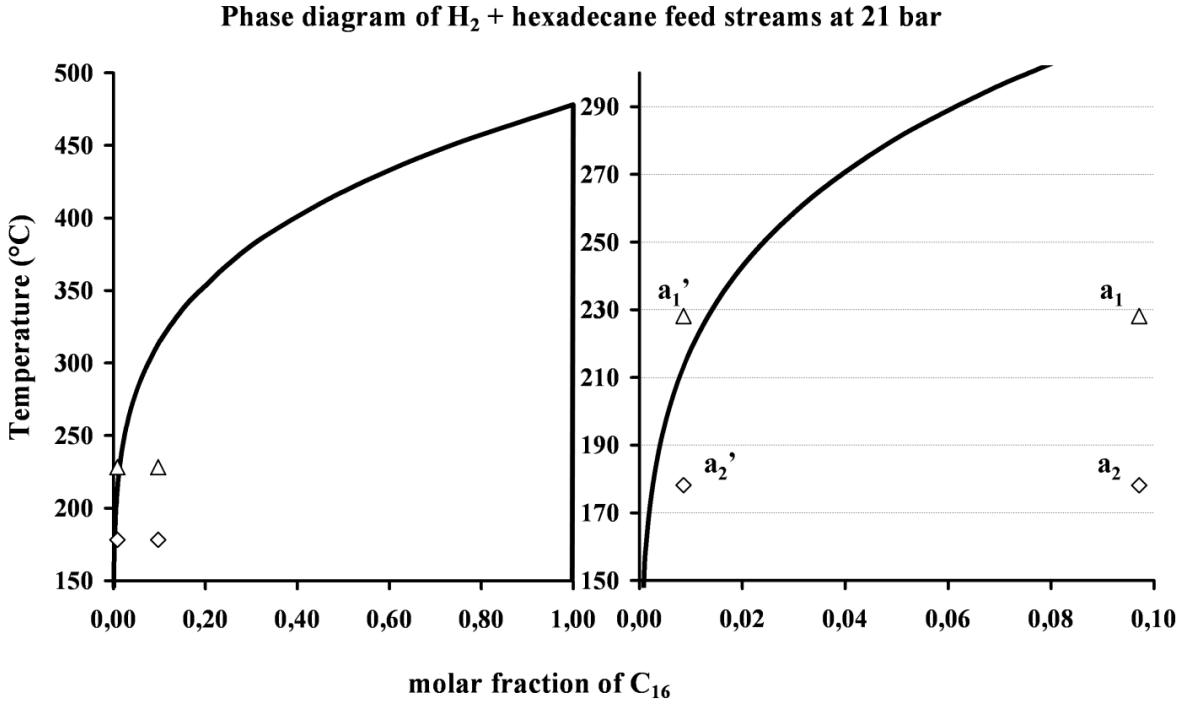

Figure A.17: Illustration of How Dilution at Too High Temperature Leads to Complete Vaporization

At the temperatures and pressures that prevail in the reactor, hydrogen is gaseous and for simplicity's sake we will ignore the negligible dilution of hydrogen in hexadecane. The liquid phase therefore consists of pure hexadecane. The composition of the liquid phase is represented by a vertical line at molar fraction 1 in the phase diagram. The curved line traces the composition of the vapor that is in equilibrium with the liquid at that temperature. Above this line, F' = 2, lies the vapor phase region, below this line, F' = 1, two phases, a liquid phase and a vapor phase, are in equilibrium. The vapor pressure of hexadecane can be read from the phase diagram by multiplying the mole fraction of hexadecane that corresponds to the temperature on the vapor-phase composition line with the total pressure. Figure A.17 shows the entire phase diagram on the left hand side, and a magnification of the relevant area of the phase diagram for our reactor system on the right hand side.

In the reactor, at 225°C, the partial pressure of C_{16} exceeds the vapor pressure. The mixture consists of a liquid phase and a vapor phase. This state is represented by the triangular point labeled: a_1 in the phase diagram. By means of the lever rule (Atkins, 2006) one can calculate the relative amounts of liquid phase and vapor phase. At a1, 13% of all C_{16} resides in the vapor phase which makes up 92% of the reactor effluent. Upon dilution of the reactor effluent with

nitrogen, composition a_1' is obtained. This composition lies in the single phase region and all hexadecane is consequently evaporated. This situation is representative of what happens in the right test unit. In the left test unit on the other hand, the reactor effluent with composition a_1 is first cooled from 225°C to 176°C as it runs down the walls of the tubing. The effluent has the composition a_2 at this point before it is diluted to a mixture of a liquid and a vapor phase with overall composition a_2'. At a_2, only 2% of the total amount of C_{16} is situated in the vapor phase which constitutes 91% of the entire effluent. By diluting this effluent stream, a further 28% of the C_{16} content is evaporated into the vapor phase. Less than 1% of the effluent is liquid but it still comprises 70% of all C_{16} at this point in the vaporizer. So, although a substantial amount of C_{16} has been evaporated by diluting the reactor effluent stream, the greater part is still in the liquid phase. This represents a much smaller shock to the system than the total evaporation that occurs in the right test unit when the dilution point is 50°C hotter at 226°C. Therefore, the scatter in the left test unit is less pronounced.

Table A.2: An overview of the C_{16} partition over the different phases

T	H_2/C_{16}	N_2/eff	x_r	x_l	x_v	n_v/n_l	n_v	n_l	$n_v x_v$	$n_l x_l$
226	10	0	0,097	1	0,013	10,8	91,5	8,5	12,6	87,4
176	10	0	0,097	1	0,013	9,6	90,5	9,5	2,4	97,6
176	10	9,6	0,0086	1	0,0026	165,7	99,4	0,6	30,0	70,0

N_2/eff; dilution ratio of the reactor effluent with nitrogen

x_r; molar fraction of hexadecane

x_l; molar fraction of hexadecane in the liquid phase

x_v; molar fraction of hexadecane in the vapor phase

n_v/n_l; ratio of amount of vapor phase over amount of liquid phase, from the lever rule

n_v; amount of vapor phase as a percentage of the total

n_l; amount of liquid phase as a percentage of the total

$n_v x_v$; amount of C_{16} in the vapor phase as a percentage of the total amount of C_{16}

$n_l x_l$; amount of C_{16} in the liquid phase as a percentage of the total amount of C_{16}

In the right test unit, the reactor effluent is diluted at 226°C and fully evaporated. The partition of C_{16} over the liquid and vapor phases is tabulated in the top line of Table A.2. In the left test unit the reactor effluent cools to 176°C before it is diluted. The corresponding partitions of C_{16}, before and after dilution are given in Table A.2.

From the above discussion it is concluded that slow controlled evaporation of C_{16} can reduce scatter in the C_{16} output. Evaporation of C_{16} occurs when the temperature is raised or when the vapor phase in equilibrium with liquid C_{16} is diluted. In the former case, the vapor pressure of C_{16} is increased thereby allowing more C_{16} to evaporate into the vapor phase, whereas in the latter case the existing partial pressure of C_{16} in the vapor phase is divided by the dilution ratio thereby allowing C_{16} from the liquid phase to evaporate to the point that partial pressure and vapor pressure of C_{16} are once more equal and the vapor phase is saturated. When the partial pressure and the vapor pressure at a particular temperature are equal; boiling occurs. Boiling as such is not a problem, in the reactor liquid and vapor phase are in equilibrium and C_{16} boils. But it can be envisaged that when a step change is introduced into the system such that the partial pressure becomes suddenly much lower than the vapor pressure this may result in fluctuations in the C_{16} partial pressure ultimately resulting in scatter in the C_{16} output. Exactly how this happens is a matter for speculation but when, locally, conditions are met for boiling to occur while overall the partial pressure is still well below the vapor pressure, the rate of evaporation may fluctuate dramatically.

Ideally, as liquid C_{16} flows down the vaporizer over an increasingly hot surface, the vapor pressure is increased at about the rate at which evaporation can increase the partial pressure of C_{16} to match the vapor pressure. This requires that the flow rate of C_{16} is low and the temperature gradient of the vaporizer not steep. According to this logic it would make sense to maximize the surface area over which C_{16} flows.

In order to achieve this, the tubing section connecting the vaporizer tube to the Swagelok VCR coupling at the bottom of the reactor was filled with SiC. The vaporizer tube had been full with SiC previously but the tubing between vaporizer and reactor including the point where the dilution gas is introduced through the Swagelok t-piece was empty. SiC dramatically increases the surface area at the dilution point and consequently lowers the superficial flow rate of C_{16}. Additionally, the temperature gradient of the right test unit was adjusted to match the profile of the left test unit.

The results of this modification – increasing the surface area at the dilution point – are presented in Figure A.18 for all reactor tubes of the left and right test unit. Standard deviations of the average C_{16} peak height are; 1.1% and 1.2% for the left test unit reactor tubes, and 1.2% and 0.8% for the right test unit reactor tubes. Such low standard deviations at last make it possible to obtain reproducible and reliable catalytic experimental data from these test units.

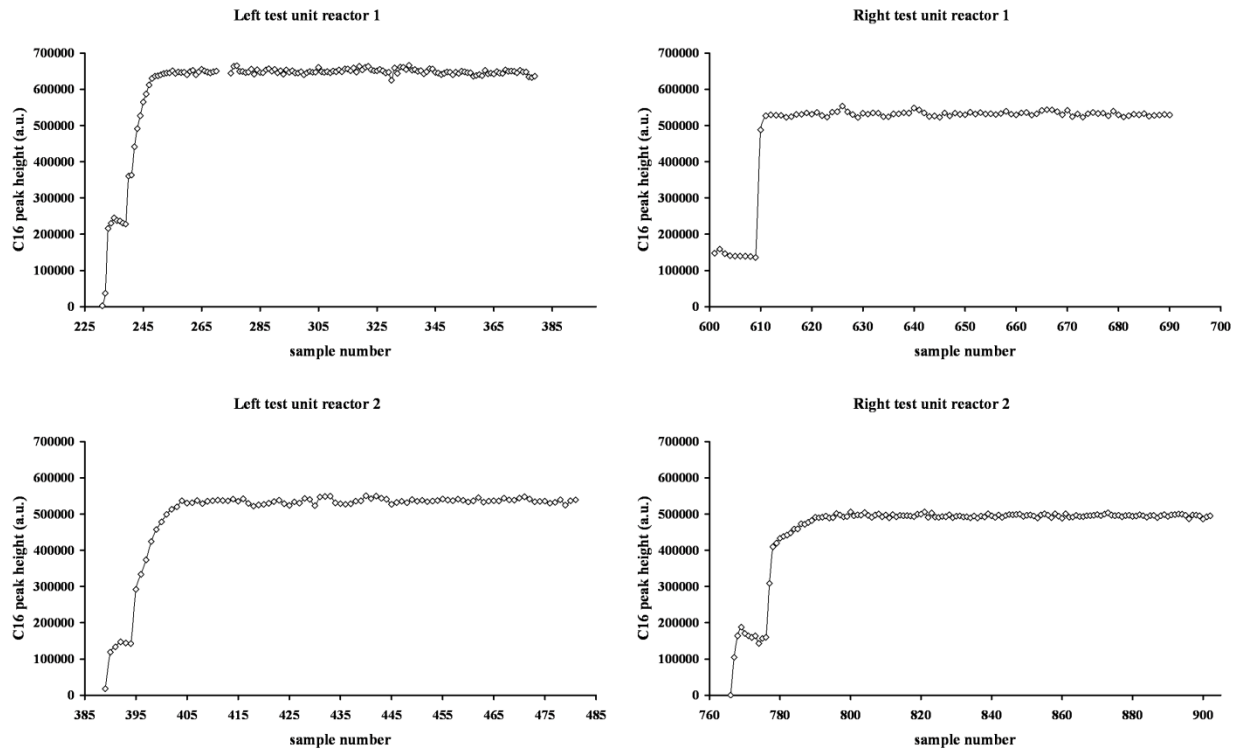

Figure A.18 (a), (b), (c) and (d): Final Results from All Reactor Tubes

Further evidence for the need for slow-flowing C_{16} feed and for a temperature gradient that isn't steep is presented in Figure A.19. During this blank run, the dilution gas was mistakenly passed through the reactor inlet together with the hydrogen/hexadecane mixture, rather than through the dilution inlet at the bottom of the reactor and just above the vaporizer. The top of the reactor has a very steep temperature gradient, and the flow rate of the vapor phase is increased by a factor equal to the dilution ratio. Both these conditions favor uncontrolled evaporation of C_{16} resulting in scatter as is clearly observed in Figure A.19.

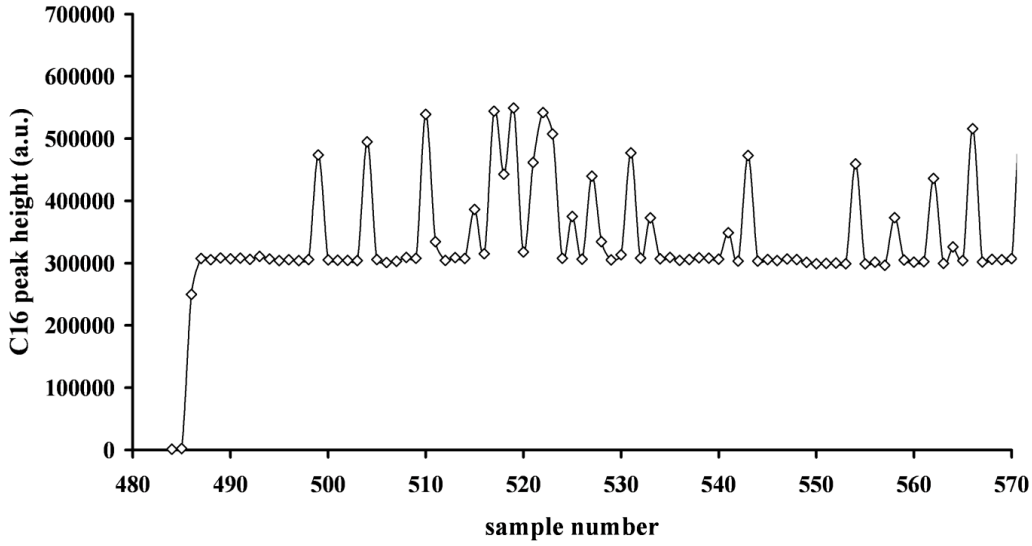

Figure A.19: Chromatographic Reproducibility with High Flow Rate of Gas at the Reactor Entry and a Steep Temperature Gradient: Scatter Observed

A.6 Co-feeding water and hexadecane

Water and hexadecane are immiscible liquids. They only mix well in the vapor phase. Figure A.20 displays what happens when, during a blank run with C_{16}, water is introduced at a flow rate of 0.02 ml/min. The C_{16} output becomes scattered with a standard deviation of 10.5%. Lowering the flow rate to 0.01 ml/min reduces the standard deviation to 5.9%, demonstrating a direct causal relation between water and scatter in the C_{16} output. Several attempts at remedying this problem were undertaken. Water was given a separate entry point at the top of the reactor. This did not resolve the issue. The top of the reactor was filled with a hydrophilic filler material, SiO_2, instead of the hydrophobic SiC. This did not resolve the problem either. Introducing water into the reactor feed stream at 0.02 ml/min lowers the C_{16} partial pressure by a factor 1.5. This is not a dramatic change; it certainly is not enough to vaporize all C_{16} in the reactor. Even at the dilution point, this extra dilution by water is not enough to force all of the C_{16} in the vapor phase upon diluting the reactor effluent with N_2, which can cause scatter as was explained above. The root of the problem must therefore simply be that C_{16} and H_2O are immiscible in the liquid phase. It stands to reason then, that removing one component from the liquid phase may solve the problem.

This was achieved by introducing water into the reactor through a dip tube which extended to the point where the temperature is high enough to vaporize the water molar fraction. On the other hand, hexadecane is allowed to flow over the SiC filled top part of the reactor. This

section of the reactor has a rather steep temperature gradient, from approximately 60°C to 225°C in 6 cm. When the hexadecane and hydrogen reach the dip tube opening, water is added to the vapor phase and not to the liquid phase. Mixing hexadecane and water in the liquid phase is not possible, but in the vapor phase they mix easily. At 573K and 20 MPa, a water and hexadecane are partially immiscible.

The water rich phase contains no appreciable amount of hexadecane, but the hexadecane rich phase contains up to 45% water (Shimoyama et al., 2002). The standard deviation of the C_{16} peak height was 1.4% before introduction of water and 1.7% when water was flowing through the reactor. Figure A.20 displays the excellent steady state blank run results.

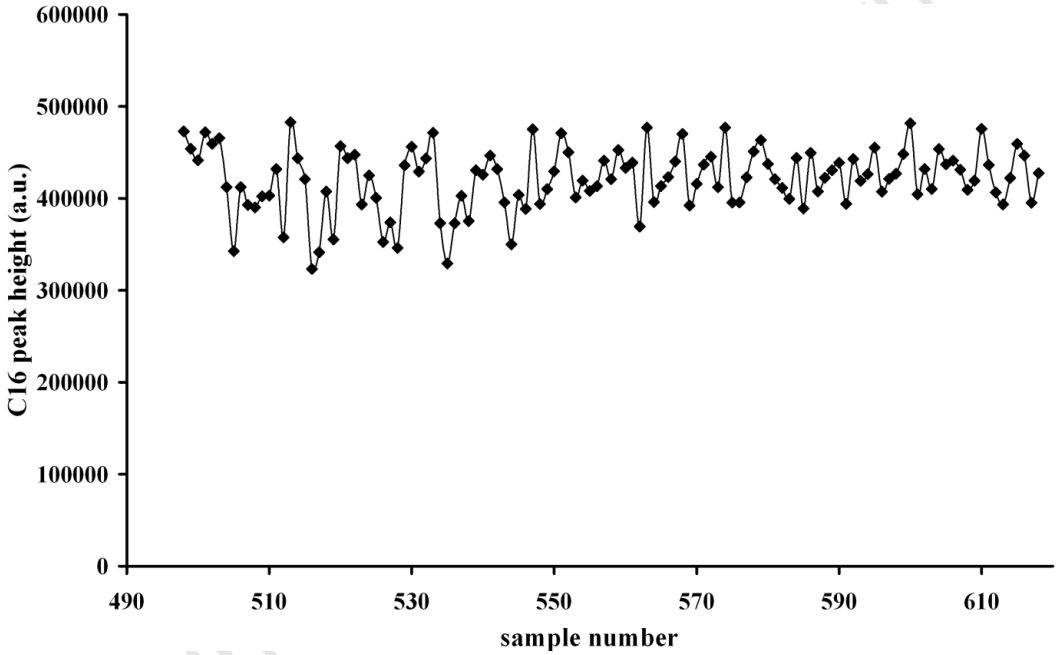

Figure A.20: Chromatographic Representation of Observed Scatter due to co-feeding of H_2O and n-C_{16}

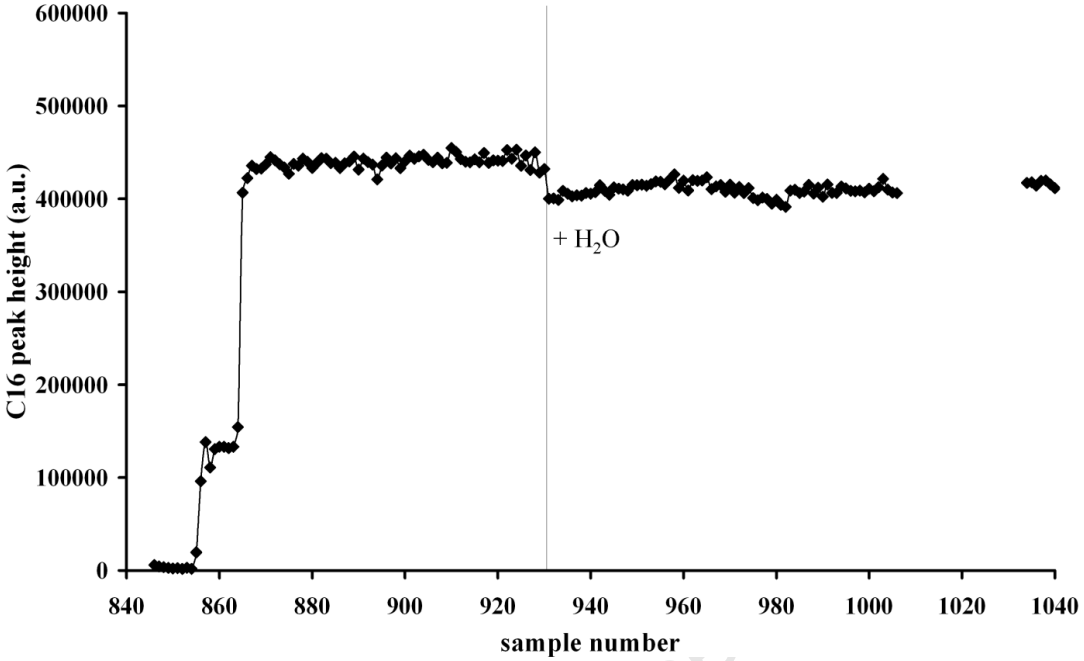

Figure A.21: Chromatographic Reproducibility with Introducing Water through a Dip-Tube

The following figure, Figure A.22 displays an overview of the sampling with time-on-stream (TOS) for Experiment B with catalyst $Pd01_BHMFI$. Total peak height as well as C_{16} peak height is plotted against time. In the following paragraph the experimental progress will be explained. A solid vertical line indicates a change of an experimental gas and/or liquid feed setting or a change in reactor temperature. The grey textured blocks indicate a transitional phase of a different nature, this will be highlighted here. In the first grey zone at the very beginning of the run, C_{16} condenses in the reactor to fill the small capacity for liquid C_{16} absorbed on the SiC inert filler. After about 12 hours C_{16} steady state is reached and the C_{16} peak height levels off. The second grey zone at 55 hours TOS indicates at temperature change in the vaporizer. The vaporizer temperature was lowered from 270°C to 235°C to avoid flash evaporation at the dilution point as was previously explained. This measure lowered the scatter in the results.

At 76 hours TOS, indicated by a solid vertical line and arrow marker, CO was introduced in place of N_2 in the gas feed stream to initiate poisoning of the noble metal co-catalyst. Deactivation is apparently from the steadily climbing C_{16} peak height, which translates into a lower conversion. During the 3rd grey zone the vaporizer temperature was first raised to 253°C at 123 hours TOS and subsequently lowered to 235°C again at 146 hours TOS in an attempt to reduce scatter in the C_{16} peak height trace.

At 170 hours TOS, again indicated by a solid vertical line and arrow marker, H_2O was introduced at 0.02 ml/min through the dip tube into the reactor. This resulted in a slightly lower total peak height since the partial pressure of C_{16} is lowered. Furthermore the C_{16} peak height seems to increase suggesting a further deactivation of the catalyst. These observations are confirmed from a plot of conversion against TOS in Figure 5.7.

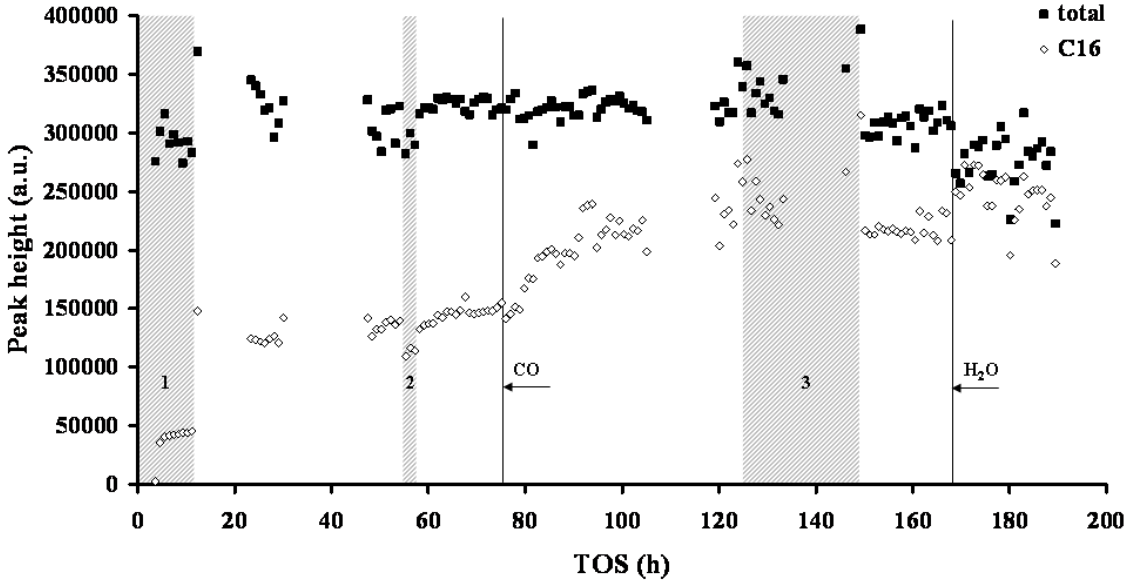

Figure A.22: Total Peak Height and n-C_{16} Peak Height versus Time-On-Stream show the Quality of the Data (Experiment B: $Pd01_BHMFI$)

A.7 Conclusion

In order to evaporate n-hexadecane in a controlled manner leading to minimal scatter in the data, the following conditions need to be satisfied.

The partial pressure of hexadecane must increase incrementally along the length of the vaporizer. Any step change in the partial pressure may result in scatter. Step changes are either a drastic increase in temperature and associated C_{16} vapor pressure or a drastic lowering of the partial pressure due to dilution of the C_{16} containing effluent. When a step change is introduced, the effect can be moderated by increasing the surface area on which C_{16} is evaporated.

Water and n-hexadecane are immiscible at the conditions prevailing in the reactor. Water has a large effect on the stability of the C_{16} output. When water and hexadecane are both

introduced in the liquid state to the reactor, large scatter of the C_{16} output is the result. This problem is resolved only when one of these components is fed to the reactor as a vapor. Since hexadecane needs to be evaporated preferably in a controlled way, water must be pre-heated and introduced as a vapor. Because the top of the reactor must remain cold so as not to aggravate the already steep temperature gradient in the SiC filler on which C_{16} is evaporated, water is introduced through a dip tube that drops down to the point at which all water is vaporous. Water runs through the dip tube and is evaporated on the progressively hot wall of the tube that extends about 15 cm into the reactor but ends well above the catalyst bed (approximately 20 cm).